Optimization of Air-Scouring Energy
in Full-Scale Submerged Membrane Bioreactor (MBR) System

by

Changyoon Jun

A dissertation submitted in partial fulfillment
of the requirements for the degree of
Doctor of Philosophy
(Environmental Engineering)
in the University of Michigan
2025

Doctoral Committee:

Professor Glen T. Daigger, Co-chair
Assistant Professor Joshua Jack, Co-chair
Senior Vice President Diana Mourato-Benedek, Anaergia Inc
Professor Jeffrey Scruggs
Assistant Professor Kean Ming Tan

Changyoon Jun

cyjun@umich.edu

ORCID iD: 0009-0007-5593-6032

© Changyoon Jun 2025

Dedication

To my beloved family, for their unwavering faith and encouragement. This dissertation is dedicated especially to my three precious princesses: my wife, Yongseon, and my twin daughters, Grace and Ellie.

Acknowledgements

First, as a Christian, I am deeply grateful to God, who has always provided what I need and guided my path.

I wish to express my deepest gratitude to my advisor, Glen, and his wife, Patty. To my advisor, Glen, a true mentor who guided me through my academic journey, and to his wife, Patty, who showed me what it means to live with warmth and integrity. I am deeply grateful for the lessons you shared, both in scholarship and in life. You have taught me not just how to think, but how to live, and it is a gift I will always treasure.

I would like to extend my sincere gratitude to my committee members for their guidance and invaluable feedback. I am especially grateful to Dr. Diana Mourato-Benedek, who played a pivotal role in the inception of this research. Her initial steps in launching this project with Glen were fundamental to its success. My thanks go to Dr. Joshua Jack for his insightful guidance and for serving as a valuable advisor from a related field within the department. His perspective enriched this work. I also thank Dr. Kean Ming Tan for his invaluable support and mentorship throughout my pursuit of the Statistics dual degree.

This research was made possible through the generous financial and technical support from Fibracast Ltd. I am deeply grateful to Steve, Bernard, Kimia, and Deo for their unwavering encouragement and support over the past four years. Their partnership was instrumental in allowing this work to flourish.

My time in the lab was made brighter by my friends and colleagues. I extend my thanks to Dr. Ko, a senior member of our group, for his wise counsel and for always sharing in both the struggles and successes. I am grateful to Dr. Yang with whom my family and I have shared a deep and cherished friendship (*jeong*) over the past five years. To Dr. Cao, who has been by my side since we both joined the group as Master's students and throughout the Ph.D. program, thank you for being a constant source of support and camaraderie for six years. I also thank Jiawei Liu, a kind and brilliant junior colleague. The cheerful moments we shared were a great source of strength.

On a personal note, a special thanks to my dear old friend, Kyung uk Kim, for your steadfast encouragement and for always having my back.

To my former colleagues from my time in the industry, the professional foundation I built with you was invaluable to this academic pursuit. To all the friends and colleagues I have met along this path, thank you.

Finally, to my family. To my father and mother, sister, and brother, thank you for your endless love and for living your lives well, which has always been my greatest motivation. To my family-in-law, thank you for welcoming me as your own. I am especially grateful to my sister-in-law, Dr. Bae, whose advice and gentle nudging were instrumental in my decision to embark on this journey. To my mother and father-in-law, thank you for your boundless love and support.

Table of Contents

Dedication ii

Acknowledgements iii

List of Tables viii

List of Figures ix

List of Appendices xii

Abstract xiv

Chapter 1 Introduction 1

1.1 Importance of the MBR Process in Water Management 1

1.2 Function and Importance of Minimizing Air Scour in MBRs 3

1.3 Hypothesis and Work Frames 4

1.3.1 Fouling Progression and Threshold Mechanisms in MBRs 4

1.3.2 Development and Validation of an Empirical Model with Full-Scale Application and Extension 7

Chapter 2 Data-Driven Threshold Modeling for Air Scour Optimization in Full-Scale MBRs 11

Chapter 3 Development of a Dual-Metric Operating Model for MBRs 14

3.1 Introduction 14

3.2 Theoretical Framework and Metric Definition 16

3.2.1 The Hydrodynamic Index with Thresholds 16

3.2.2 Fouling State Diagnostics (Analysis of Resistance Components) 16

3.3 Methods 18

3.3.1 Full-Scale MBR System Evaluated 18

3.3.2 Data Acquisition and Processing 19

3.3.3 Calculation of Metrics and Application 21
3.3.4 Evaluation of Fouling Rate 23
3.3.5 Statistical Evaluation of Operating Categories 24
3.4 Results 24
3.4.1 Summary of Plant Operation 24
3.4.2 Relationship Between Hydrodynamic Index (K) and Total Resistance (R_T) 28
3.4.3 Analysis of Resistance Responses 30
3.4.4 Development of Fouling Resistance Components: Trajectory Analysis 33
3.4.5 Categorization of Operating Conditions using Dual-Metric Control Matrix 37
3.4.6 Development of Action Matrix 39
3.5 Discussion 41
3.6 Conclusions 47
Chapter 4 Integrated Framework for MBR Operation and Generalization 50
4.1 Introduction 50
4.2 Method 51
4.2.1 Data Sources and Processing 51
4.2.2 Fouling State Diagnosis and Correlation Analysis 53
4.2.3 Evaluation of System Responses and Generalization 54
4.2.4 Visualization of Actual Capacity 54
4.3 Results 55
4.3.1 Comparison of Historical Operational Conditions 55
4.3.2 Comparison of Different Pathways to Limiting Conditions: Plants A and C 58
4.3.3 Investigating Fouling Dynamics in Plant A 60
4.3.4 Insights into Controlling Intact Fouling 63
4.3.5 Fouling Dynamics in Plant B: An Indirect Assessment 65

4.3.6 Generalization of Control Matrix 66
4.4 Discussion 69
4.4.1 The Unifying Concept of Actual Capacity 69
4.4.2 Visualizing the Actual Capacity with Operational Data 72
4.4.3 A Holistic Framework for MBR Management 73
4.5 Conclusion 75
Chapter 5 Discussion and Conclusion 77
5.1 Interpreting Fouling Dynamics through a Dual-Metric Framework 77
5.2 Contributions and Originality 80
5.3 Practical Implications 81
5.4 Limitations of the Study 82
5.5 Future Research Directions 83
5.5.1 From Reactive to Proactive Control via Predictive Modeling 83
5.5.2 From Predictive Control to Autonomous Optimization via Reinforcement Learning 84
5.5.3 From Single-Plant Autonomy to Fleet-Wide Intelligence via Hierarchical Models 84
5.6 Conclusion 85
Appendices 86
Bibliography 108

List of Tables

Table 3.1: Summary of Operational Conditions 18

Table 3.2: Segmented Historical Dataset 19

Table 4.1: Comparison of Physical Configurations and Cleaning Protocols for Plants A, B, and C 52

Table 4.2: Detailed Configuration of MBR Plants 52

Table 4.3: Key operational statistics for each train in Plant A, B, and C. Values are presented as mean ± standard deviation. 57

Appendix Table A.1: Taxonomy of Threshold Flux Concepts in MBR Operation 88

Appendix Table A.2: Dominant Back-Transport Mechanisms and the "Fouling Window" 94

Appendix Table A.3: MBR Characteristics from a Complex Systems Perspective 97

List of Figures

Figure 3.1: Daily average variations of key operational variables for Plant C. Panel: (a) Transmembrane Pressure (TMP) with five segregated periods (P1-P5) indicated, (b) permeate flux, (c) Specific Air Demand per Membrane area (SAD_m) and mean MLSS concentration in the MBR tank ($MLSS_{tank}$), and (d) the hydrodynamic index (K). The horizontal red dashed line in the panel (d) indicates the limiting value of K (K_{Lim})..... 26

Figure 3.2: Daily averaged variation of resistance components. Panel: (a) total resistance (R_T), (b) back-pulsing resistance (R_{BP}), and (c) cake resistance (R_{cake}). Vertical lines denote recovery clean events, color-coded by train. (Blue: Train 1; Orange: Train 3; Green: Train 4). 27

Figure 3.3: Daily Average Correlation between the Hydrodynamic Index (K Value) and Total Resistance (R_T) for Trains 1, 3, and 4 (panel (a), (b), and (c) respectively): Data points are color-coded to indicate the date of operation, showing the temporal progression of the system's state. The solid red vertical line represents the limiting K value (K_{Lim}), and the dashed black vertical line represents the target K value (K_{Target}). 29

Figure 3.4: Correlation of resistance components with total resistance (R_T) for Trains 1, 3, and 4, colored by the corresponding K value. The top row (panels (a), (b), (c)) shows Back-pulsing resistance (R_{BP}) vs. R_T, while the bottom row (panels (d), (e), (f)) shows Cake resistance (R_{cake}) vs. R_T. Horizontal dash-dot lines represent empirically determined thresholds for each resistance component. The solid red line is a 1:1 reference line. Pink highlighted circles indicate high solid loading conditions (MLSS > 10g/L). 31

Figure 3.5: Periodic trajectory analysis (Period 3-5: July 2024 onward) of R_{BP} versus R_{cake} for Trains 1, 3, and 4, illustrating Pathway A. Data points are colored by the K value (m·s/kg). Dash-dot lines represent the resistance thresholds. Diagonal lines are iso-resistance reference lines. Each panel (a-l) represents a distinct operational period. Asterisks denote the first day of each period, squares indicate the last day, and red diamonds mark recovery clean events..... 34

Figure 3.6: Periodic trajectory analysis (Period 1-2: Feb. – July 2024) of R_{BP} versus R_{cake} for Trains 1, 3, and 4, illustrating Pathway B. Data points are colored by the K value (m·s/kg). Dash-dot lines represent the resistance thresholds, and diagonal lines are iso-resistance reference lines. Each panel (a-f) represents a distinct operational period. Asterisks denote the first day of each period, squares indicate the last day, and red diamonds mark recovery clean events. 36

Figure 3.7: Control matrix based on the K Value and Resistance Thresholds: The main plot (panel (a)) shows Total Resistance (R_T) vs. K value. The supplemental plots show the same data space but are separated into Back-Pulsing Resistance (R_{BP}, panel (b)) and Cake Resistance

(R_{cake}, panel (c)). Data points are color-coded by the fouling rate (dTMP/dt), and the median fouling rate for each of the nine operational regions is annotated. 38

Figure 3.8: A conceptual 2x2 management framework derived from the control matrix. The x-axis represents the hydrodynamic state relative to the K_{Target} threshold (e.g., 2.0×10^{-8} m·s/kg), and the y-axis represents the fouling state relative to the first total resistance (R_T) threshold (e.g., 1.4 kPa/LMH). Each quadrant suggests targeted operational actions to maintain or restore system stability..... 40

Figure 3.9: Correlation plots of cake resistance (R_{cake}) versus back-pulsing resistance (R_{BP}) for Trains 1, 3, and 4 (panel (a), (b), and (c)). Data points are color-coded by the corresponding Transmembrane Pressure (TMP). The plot illustrates the critical fouling transition phenomenon (consolidation) where, under high TMP (red points), Rcake may decrease as R_{BP} increases 43

Figure 4.1: Daily averaged total resistance (R_T) and permeate flux for Plant A (panel (a)), Plant B (panel (b)), and Plant C (panel (c)). Black solid and dashed lines represent individual trains. The light blue line indicates the plant-wide average flux. Red vertical markers denote maintenance cleaning events..... 56

Figure 4.2: Fouling characteristics for Plant A (left column) and Plant C (right column) as a function of Transmembrane Pressure (TMP). The top row (panels (a) and (b)) shows fouling rate (FR) vs. TMP, color-coded by total resistance (R_T). The middle row (panels (c) and (d)) shows back-pulse resistance (R_{BP}) vs. TMP, and the bottom row (panels (e) and (f)) shows cake resistance (R_{cake}) vs. TMP. Data points in the middle and bottom rows are color-coded by permeate flux. 59

Figure 4.3: Fouling trajectory analysis plotting back-pulse resistance (R_{BP}, x-axis) against cake resistance (R_{cake}, y-axis) for Train 1 (panel (a)) and Train 2 (panel (b)) of Plant A. Data points are color-coded by date to illustrate temporal evolution. The background contour lines indicate fouling rate (FR), with darker gray lines representing higher FR values. Red circles highlight the data point immediately following a recovery clean (RC). The diagonal lines represent iso-resistance thresholds ($R_{BP}+R_{cake}$ = 1.4 and 2.1 kPa/LMH) derived from Plant C (Chapter 3) for benchmarking..... 62

Figure 4.4: Box plot comparison of cleaning strategies implemented in Plant A (A T1, A T2) and Plant C (C T1, C T3, C T4). The panels show distributions for (panel (a)) the interval between Back-Pulsing (BP) events, (panel (b)) the intensity of BP events measured as flux, and (panel (c)) the interval between Maintenance Cleaning (MC) events. The central mark in each box indicates the median, the box edges represent the 25th and 75th percentiles, the whiskers extend to the most extreme data points not considered outliers, and outliers are plotted individually as dot marks. 64

Figure 4.5: Box plot distribution of the daily fouling rate (FR) in Plant B as a function of the number of days since the last maintenance cleaning (MC) event. The central mark in each box indicates the median, the box edges represent the 25th and 75th percentiles, the whiskers extend to the most extreme data points not considered outliers, and outliers are plotted individually as dot marks. 66

Figure 4.6: Generalized control map plotting daily averaged K value versus total resistance (R_T) for Plant A (panels (a), (b)), Plant B (panel (c)), and Plant C (panels (d), (e), and (f)). Data points are color-coded by the magnitude of the normalized fouling rate (FR). Vertical lines indicate the target K value (K_{Target}, black dash-dot) and the limiting K value (K_{Lim}, red dashed). Horizontal lines indicate the empirically determined iso-resistance thresholds: the first (black dash-dot) and the second (red dashed). 68

Figure 4.7: Conceptual illustration of a system's declining 'Actual Sustainable Capacity' (red line) in response to fouling progression, shown against a typical diurnal 'Operational Flux' pattern (black line) and the fixed maximum design capacity (blue dashed line). The shaded orange areas represent periods where the operational demand exceeds the system's sustainable capacity, leading to accelerated fouling. 71

Figure 4.8: Fouling rate (FR) versus permeate flux, with total resistance (R_T) shown as color contours for Plants A, B, and C (panel (a), (b), and (c), respectively). The contours, smoothed using a LOWESS function to reveal the underlying trends, visualize the system's dynamic Actual Capacity by showing how the sustainable operational window shrinks as resistance increases. 72

Figure 4.9: A holistic MBR management framework. Fouling acts as the central variable connecting system capacity (CAPEX) to operational control actions and long-term overhaul needs (OPEX). An intelligent control strategy based on real-time monitoring optimizes this entire lifecycle. 74

Appendix Figure B.1: Example output of the automated cycle classification algorithm. The algorithm successfully identifies and segments the time series into Permeation cycles (blue dots) and Back-pulsing events (red dots). 105

List of Appendices

Appendix A: Theoretical Foundations of Threshold Phenomena in MBR Systems: A Spectral Perspective 86

A.1 Background and Purpose 86

A.2 The Deterministic Paradigm: Concepts and Assumptions 87

A.2.1 The Critical Flux Concept and Taxonomy 87

A.3 Mechanistic Foundations: Mass Balance and Force Balance Perspectives 88

A.3.1 The Integrated Framework 88

A.3.2 Defining Criticality 91

A.3.3 Factors Influencing the Mechanistic Balances 92

A.3.4 The Interplay of Mechanisms and Operational Challenges 94

A.3.5 The Amplifying Dimensions of Operational Complexity 95

A.4 MBR as a Complex Adaptive System 96

A.5 The Spectral Interpretation of Threshold Phenomena 98

A.6 The Paradigm Shift: From Prediction to Adaptive Management 99

A.7 Conclusion 101

Appendix B: Data Processing Methodology 102

B.1 Overview of the Data Processing Pipeline 102

B.2 Detailed Data Processing Steps 103

B.2.1 Resampling and Normalization 103

B.2.2 Automated Operational Cycle Classification 103

B.2.3 Data Cleaning and Feature Engineering 105

B.2.4 Resistance Calculation Protocol 106
B.2.5 Data Aggregation and Alignment 107

Abstract

Membrane Bioreactor (MBR) technology is essential for sustainable water management and advanced water reuse; however, its widespread adoption is constrained by high operational costs, primarily driven by the energy consumption of air scouring used to control membrane fouling. To ensure reliability, operators often maintain conservative, energy-intensive aeration regimes because they lack robust, real-time indicators to predict the onset of critical fouling transitions in complex, full-scale environments. This dissertation addresses this gap by developing and validating a data-driven, dual-metric framework to optimize air scour energy while maintaining system stability.

This research is grounded in the hypothesis that fouling transitions are governed by the dynamic balance between convective deposition and shear-induced removal. The study involved the analysis of long-term, high-frequency operational data from three distinct full-scale MBR facilities.

The initial phase introduced a physically interpretable hydrodynamic index, the "K value." This index integrates key operational variables, including permeate flux, air flow, Mixed Liquor Suspended Solids (MLSS) concentration, and total resistance, to quantify the system's proximity to fouling thresholds. Validation across multiple facilities demonstrated that a critical threshold (K_{Lim}) reliably signaled the onset of rapid, unstable fouling (the "Limiting Condition"). Utilizing this model suggested significant potential for energy savings, suggested a potential for 30-40% energy savings, by determining the minimum required aeration.

Recognizing that hydrodynamic optimization alone is insufficient, as persistent fouling may be unresponsive to increased aeration, the study evolved into a dual-metric framework. This approach integrates the K value (hydrodynamic stress) with in-situ resistance component analysis derived from back-pulse data. This enables the operational

differentiation between dynamic cake accumulation (R_{cake}) and persistent intact fouling (R_{BP}), facilitating targeted interventions rather than generalized increases in aeration.

The framework was generalized across the three plants, leading to the introduction of "Actual Capacity." This unifying concept redefines MBR performance limits as dynamic and state-dependent, reflecting the interplay between hydrodynamic stress and the evolving fouling state. A diagnostic control matrix was developed to operationalize this concept for real-time decision support.

This dissertation facilitates a paradigm shift from reactive maintenance to proactive system health management. The dual-metric framework provides operators with practical tools to significantly reduce operational expenditures (OPEX), enhance system reliability, and preserve Actual Capacity (CAPEX), thereby advancing the sustainability and economic viability of MBR technology.

Chapter 1 Introduction

1.1 Importance of the MBR Process in Water Management

Water scarcity is no longer a distant threat but a growing reality, driven by population growth, urbanization, industrial expansion, and shifting consumption patterns. Recent industrial advances, including the rapid rise of the Artificial Intelligence (AI) industry, have accelerated water demand, while climate change continues to intensify global aridification and diminish available resources(FOOD & WATER WATCH 2025; He et al. 2021; UN Water 2024). Traditional approaches that focus solely on developing new freshwater supplies are increasingly proving unsustainable (UN Water 2024).

In response, membrane bioreactor (MBR) technology offers a more resilient and effective solution. MBR systems combine activated sludge biological treatment with membrane filtration processes such as microfiltration (MF) and ultrafiltration (UF) to consistently produce high-quality treated water and improved control of pathogens compared to alternate biological treatment technologies (Francy et al. 2012). By effectively removing nutrients such as nitrogen and phosphorus, MBR effluent improves the quality of receiving water bodies, prevents eutrophication, and helps protect aquatic ecosystems. This treatment quality also promotes the development of circular water systems by enabling the local reuse of treated water and sustaining downstream resources (Daigger et al. 2019). MBRs can operate at high mixed liquor suspended solids (MLSS) concentrations, which significantly reduces the footprint compared to conventional processes, increases treatment capability, and expands opportunities for water reuse in urban and industrial environments. Therefore, as droughts become more severe and water

needs grow more complex, MBR technology is increasingly seen as a cornerstone of sustainable water management and integrated reuse strategies.

A persistent challenge in MBR operation is membrane fouling, the deposition of particles that gradually declines filtration capacity. The evolution of MBR technology has largely been driven by efforts to control this fouling efficiently. Early MBR systems, introduced in the late 1960s, utilized side-stream configurations (e.g., tubular membranes external to the bioreactor) and relied on high cross-flow velocities for cleaning. These methods were highly energy-intensive due to the required pumping, restricting MBRs primarily to small-scale industrial applications. The pivotal advancement was the development of submerged MBRs, pioneered by Yamamoto in 1989 (Yamamoto et al. 1988). In these systems, the membranes (configured as hollow fibers or flat sheets) are submerged in the bioreactor and utilize air scour (the injection of air bubbles) rather than high-velocity pumping for fouling control.

This innovation dramatically reduced energy consumption compared to side-stream systems, enabling application to large-scale municipal facilities and fueling rapid commercialization. Consequently, submerged MBRs are now the dominant configuration. While air scour solved one energy problem, it introduced another. In submerged systems, air scour is essential for generating hydrodynamic shear at the membrane surface to remove foulants and maintain performance. However, it is also the dominant contributor to energy consumption, accounting for 30–60% of the total energy demand (Barillon et al. 2013; Monclús et al. 2015). Therefore, optimizing air scour intensity is critical for the overall sustainability and economic viability of MBR technology. Note that, given their prevalence, the term "MBR" will henceforth be used to refer specifically to the submerged configuration unless otherwise specified.

1.2 Function and Importance of Minimizing Air Scour in MBRs

While air scour is essential for the continued operation of the membranes in an MBR process, minimizing air scour is crucial for improving the energy efficiency and sustainability of MBRs. Excessive aeration not only leads to increased operational costs but also to other performance issues. For example, over-aeration can destabilize biomass, promote the generation of smaller particles (Guo et al. 2008; Meng et al. 2009; Yang et al. 2009), create uneven shear profiles due to changes in bubble behavior and hydrodynamic conditions (Li and Wang 2006; Wang et al. 2021), and condense the fouling layer (Ding et al. 2016; Du et al. 2017b; Erkan et al. 2020), ultimately worsening filtration performance. Over-aeration can also damage the membrane itself by either breaking the hollow fibers or sheets or peeling off the thin polymeric layer that creates the ultrafiltration property of the membrane. Furthermore, it can hamper the denitrification process by disrupting the low ORP (anoxic) conditions in the preceding zone of the bioreactor. Balancing sufficient fouling control with minimized aeration remains one of the key optimization challenges in MBR operation.

Achieving this balance, however, remains elusive in practice due to limitations in current air scour control strategies. In real-world full-scale MBR applications, air flow rates are often static, pre-set, or determined by empirical heuristics, rather than dynamically adjusted in response to actual membrane fouling state or filtration demand (Drews 2010; Vera et al. 2015). This non-adaptive approach invariably results in suboptimal operation and unnecessary energy consumption, highlighting the need for more adaptive air scour strategies. This limitation stems from an unresolved gap between fundamental fouling research and operational practice (Drews 2010). On one hand, there has been significant progress in understanding how fouling mechanisms operate at a fundamental level (Belfort et al. 1994; Bhattacharjee et al. 1999; Hermia 1985; Romero and Davis 1988, 1990; Song and Elimelech 1995). On the other hand,

extensive empirical observations have identified operational thresholds that indicate when fouling accelerates, beginning with the foundational 'critical flux' concept (Bacchin et al. 1995; Field et al. 1995) and later expanding to a broader taxonomy of pragmatic limits like sustainable and threshold flux (Bacchin et al. 2006; Field and Pearce 2011), a topic reviewed in detail in Appendix A. However, a robust predictive framework linking these mechanistic insights to the onset of threshold transitions remains elusive (Jun et al. 2024; Monclús et al. 2015). In particular, how the hydrodynamic balance, the interplay between convective foulant deposition and shear-induced back transport, governs these transitions is not yet fully understood (Drews 2010; Meng et al. 2017). Consequently, operators lack the reliable indicators needed for optimized control and often default to conservative, energy-intensive aeration regimes to ensure reliability and mitigate fouling risk. This practice incurs a significant energy penalty and undermines the overall sustainability of MBR technology.

1.3 Hypothesis and Work Frames

1.3.1 Fouling Progression and Threshold Mechanisms in MBRs

This study hypothesizes that the fouling transition point in MBR systems is primarily governed by the dynamic balance between the convective transport of particles toward the membrane surface (driven by permeate flow) and their removal by hydrodynamic shear forces generated through air scour. This balance determines whether particles accumulate or are back-transported from the membrane interface (Belfort et al. 1994; Davis 1992; Jørgensen et al. 2012). The extent of deposition is further influenced by interfacial adhesion forces arising from foulant–membrane and foulant–foulant interactions (Meng et al. 2009), which affect the likelihood of particle attachment once contact occurs (Li and Wang 2006; Mannina and Di Bella 2012). Therefore, we hypothesize that hydrodynamic forces primarily govern the transport of particles

to and from the surface, while interfacial interactions determine the attachment efficiency and the resulting extent of actual deposition. Understanding and quantifying this relationship is critical to optimizing air scour intensity, which remains the dominant and most energy-intensive control parameter in MBR operation.

To analyze this system, the key forces influencing fouling behavior are classified into three categories: (1) deposition forces associated with permeate drag (Belfort et al. 1994), (2) removal forces including hydrodynamic lift and shear-induced dispersion (Cui et al. 2003; Yeo and Fane 2005), and (3) interfacial forces modulating adhesion (Hoek and Elimelech 2003; Kang et al. 2004; Meng et al. 2007). A theoretical foundation for these interactions and the mechanisms underlying resulting threshold phenomena (e.g., critical flux) is provided in Appendix A, while the present section focuses on their practical implications for full-scale operations.

The net rate of foulant accumulation on the membrane surface can be described by a mass balance (Jørgensen et al. 2012; Wang and Li 2012):

$$\frac{dM}{dt} = J_{convective} - J_{back} = J \cdot C - D_{eff}\frac{dC}{dx} \qquad \text{Equation (1.1)}$$

where $J \cdot C$ represents the convective solids flux, and $D_{eff} \cdot (dC/dx)$ denotes the back-transport flux, driven by the local concentration gradient and an effective diffusivity D_{eff}.

In MBR systems, the effective diffusivity D_{eff} represents the cumulative contribution of several particle transport mechanisms that facilitate back-transport from the membrane surface (Belfort et al. 1994; Davis 1992; Romero and Davis 1988; Schwarz et al. 2006). These include Brownian diffusion for submicron colloids, shear-induced diffusion for micrometer-scale suspended solids, and inertial lift for larger particles (typically greater than 10–20 μm). Although inertial lift is a deterministic force arising from fluid inertia and velocity gradients near

boundaries, it promotes particle migration away from surfaces in a manner functionally similar to diffusion. For modeling purposes, inertial lift is therefore incorporated into D_{eff} (Belfort et al. 1994). Additional factors such as turbulence-enhanced dispersion or site-specific hydrodynamic phenomena may also contribute (Cui et al. 2003; Drews 2010; Psoch and Schiewer 2005; Wintgens 2003).

The overall mass balance of foulant transport is expressed in Equation 1.1, where the convective flux term $J_{convective}$ corresponds to permeate drag driving particles toward the membrane, and the back-transport flux J_{back} reflects the combined effects of hydrodynamic shear and interfacial adhesion resisting deposition. Within J_{back}, hydrodynamic shear enhances particle removal by increasing D_{eff} and stabilizing the concentration gradient dC/dx near the membrane surface. However, even under strong shear conditions, the effectiveness of back-transport is modulated by interfacial adhesion arising from particle-specific properties such as size, structure, and surface interactions, which influence the net deposition rate (Chen et al. 2017; He et al. 2016). For example, colloidal particles are less affected by shear intensity due to their small size and higher surface charge, which leads to stronger repulsive interactions (Davis 1992; Mcdonogh et al. 1989; Meng et al. 2009). As a result, they are generally more resistant to deposition and exhibit less sensitivity to threshold transitions governed by hydrodynamic shear (Bacchin et al. 1995; He et al. 2016; Wang and Li 2012).

The net rate of foulant accumulation is governed by the dynamic balance between $J_{convective}$ and J_{back}. When back-transport sufficiently offsets convective deposition, accumulation remains slow or negligible. Conversely, when this balance breaks down, due to inadequate shear or unfavorable particle characteristics, accumulation accelerates sharply, marking a transition

from stable to unstable fouling behavior. Such threshold transitions have been widely observed in MBR systems and are described by phenomenological concepts such as the critical flux.

The fouling thresholds manifest as abrupt changes in the rate of foulant accumulation (dM/dt). In laboratory-scale studies, they may appear as subtle increases in membrane resistance (e.g., weak critical flux) (Field et al. 1995), while in full-scale MBR operations, they typically correspond to more pronounced transitions, such as the onset of irreversible fouling (critical flux for irreversibility) (Bacchin et al. 2006) or a clear inflection point in the fouling rate (threshold flux) (Field and Pearce 2011). Although these terms are often categorized separately, they essentially describe the same underlying phenomenon, the breakdown of the balance between convective deposition and shear-induced back-transport, interpreted differently depending on the specific operational context or control objective. In submerged MBR systems, air scour is the primary mechanism for generating the necessary shear to maintain this balance and delay the onset of critical fouling. Ultimately, understanding and characterizing fouling threshold transitions is central to the objective of optimizing air scour strategies. Building on this conceptual foundation, the present study proposes a data-driven, force-balanced approach for detecting threshold behavior and optimizing air scour intensity in full-scale MBR systems.

1.3.2 Development and Validation of an Empirical Model with Full-Scale Application and Extension

In the following chapter (Chapter 2), an empirical model is developed aimed at identifying fouling thresholds using historical operational data from full-scale MBR systems. The model is conceptually grounded in the mass balance framework introduced in Equation 1.1, operationalizing the underlying mass balance. Major operational variables, including aeration rate, permeate flux, and MLSS concentration, are incorporated to identify the critical conditions

under which this balance (convection vs. shear) fails, leading to rapid mass deposition. To balance mechanistic relevance with practical applicability, complex secondary factors, such as interfacial interactions, are simplified into a constant term. By assessing the operational proximity to the fouling threshold, the model provides actionable, quantitative guidance on how aeration intensity can be adjusted to maximize energy savings without compromising system stability.

The model was validated using over a year of operational data from two full-scale MBR facilities treating primarily municipal wastewater. In this analysis, operational thresholds were defined by the onset of rapid increases in the fouling rate (dTMP/dt). A critical insight emerged regarding the dynamic role of total resistance (R_T = TMP/Flux/viscosity). We found that R_T modulates the hydrodynamic conditions near the membrane surface. As fouling increases R_T, higher TMP is required to maintain a constant applied flux. This elevated pressure increases the local convective drag, making the system more susceptible to fouling transitions even under the same apparent flux. Incorporating this dynamic feedback mechanism enables more accurate inference of actual hydrodynamic stress and fouling transition patterns. The results demonstrate that this empirical model, which operationalizes the theoretical mass-balance framework using real-world data, can reasonably detect threshold behavior.

In Chapter 3, this investigation is extended to a third full-scale MBR operating at consistently higher flux levels than the previous two. Under these conditions, fouling stress intensifies, offering deeper insight into how high-load conditions impact fouling progression and influence threshold transitions. These findings emphasize that a more comprehensive understanding of fouling dynamics is essential not only for aeration optimization but also for robust system optimization.

The challenges observed under these high-stress conditions underscore the limitations of conventional control strategies. As established in the literature, while external shear can effectively manage reversible fouling and maintain bulk solid flow (Delgado et al. 2008; Drews 2010; Du et al. 2017b), it becomes insufficient against inner-layer deposits as heterogeneous or more cohesive, compact fouling layers develop, often classified as irreversible fouling (Aslam et al. 2017; Desmond et al. 2022; Kang et al. 2004). As fouling progresses, the convective load increases due to rising TMP under a constant flux condition (i.e., increasing local permeation drag), while the effectiveness of shear mitigation decreases (Hwang et al. 2008; Schwarz et al. 2006). This decline results from increased local solids concentration and viscosity (Le-Clech et al. 2006; Meng et al. 2007; Trussell et al. 2007), as well as shear saturation effects that limit the additional benefit of further aeration, lowering the threshold at which rapid fouling transitions occur (Jeison and Van Lier 2006; Pritchard et al. 1995; Trussell et al. 2007). Under such conditions, simply increasing air scour intensity is ineffective and may even aggravate fouling by promoting floc breakup, which releases fine particles that penetrate the voids of the fouling layer, leading to its consolidation and densification (Ding et al. 2016; Meng et al. 2009; Tarleton 1994).

These observations highlight the need to better characterize the system's response to fouling progression, particularly to identify the onset of irreversible fouling. One promising approach involves the use of back-pulsing resistance measurements, which indicate the integrity and reversibility of fouling layers (Diez et al. 2014). Such measurements, when applied to long-term full-scale datasets, can be systematically linked to actionable operational responses grounded in fouling mechanisms and threshold theory (Appendix A).

In Chapter 4, the study synthesizes these findings across all three full-scale systems to evaluate and generalize the dual-metric framework. This includes the empirical validation and

introduction of the unifying concept of "Actual Capacity" (which redefines MBR performance limits as dynamic and state-dependent) and the proposal of a control matrix designed to support proactive, feedback-based operation aimed at optimizing OPEX and preserving CAPEX.

Finally, Chapter 5 provides a comprehensive synthesis, formally linking the empirical findings back to threshold flux theory and summarizing the key contributions and practical implications of this research for sustainable MBR operation (e.g., energy savings, reliability, and asset longevity). It concludes by outlining a roadmap for future research, emphasizing the progression toward predictive modeling and autonomous, AI-driven optimization (e.g., via Reinforcement Learning).

Chapter 2 Data-Driven Threshold Modeling for Air Scour Optimization in Full-Scale MBRs

As introduced in Chapter 1, optimizing air scour intensity in full-scale MBR systems remains a persistent challenge due to the lack of reliable indicators for the fouling rate threshold. In the absence of the ability to detect the transition, operators have to maintain conservative aeration levels to avoid performance loss, often resulting in excessive energy consumption. This chapter addresses the need for a threshold-based framework that can infer the operational proximity to transition points, indicating how close the current operating state of the MBR system is to the onset of rapid fouling and enabling more efficient, data-informed control of air scour.

To this end, we derived a physically interpretable threshold indicator based on fundamental system variables. The limiting condition for threshold onset, denoted as K_{Lim}, is expressed as:

$$K_{Lim} \leq \alpha_s \cdot Q_A \cdot \frac{1}{Q_P \cdot \mu_{app} \cdot MLSS \cdot R_T} \qquad \text{Equation (2.1)}$$

where Q_A (m^3/hr) is the air flow rate, Q_P (m^3/hr) is the permeate flow rate, μ_{app} is the apparent viscosity of the mixed liquor (Pa·s), MLSS (g/l) is the arithmetic mean mixed liquor suspended solids concentration in the membrane bundle, R_T is the total resistance (m^{-1}), incorporating the temperature-corrected water (permeate) viscosity at 20°C, and α_s is the membrane packing density (m^2/m^3). This formulation provides a means to assess how close an operating condition is to the fouling rate threshold using continuously monitored variables via sensor measurements,

coupled with parameters that change relatively slowly such as MLSS. It enables adaptive adjustment of aeration by interpreting system vulnerability under current loading and hydraulic conditions.

The model was evaluated using long-term data from two full-scale MBR facilities (Plant A and B) with distinct influent characteristics and operational strategies but utilizing corrugated flat sheet membranes from the same membrane manufacturer. Despite these differences, both systems exhibited statistically similar values for K_{Lim} at their respective transition points. This consistency supports the generalizability of the threshold framework and demonstrates its potential to inform air scour control across diverse operating conditions.

Building on this result, a simplified air scour control logic is proposed based on the estimation of a critical air-to-permeate flow ratio. By rearranging the threshold expression, the critical scour demand can be expressed as:

$$\frac{Q_{A,Crit}}{Q_P} = \frac{K_{Lim}}{\alpha_s} \cdot MLSS \cdot \mu_{app} \cdot R_T \qquad \text{Equation (2.2)}$$

where $Q_{A,Crit}$ is the minimum air scouring flow rate at which a limiting condition occurs and K_{Lim} is the threshold-inducing value of the system, statistically determined from full-scale data collected under limiting operating conditions. The remaining terms on the right-hand side are gradually varying and can be reasonably assumed constant over short operational time frames. As a result, this equation enables estimation of the required air input based on a given flux, thus providing a quantitative basis for real-time aeration control. Analysis of actual plant air scour flow rate compared to the minimum air scour flow rate calculated using the equation above indicated the potential for significant energy savings.

This relationship enables calculation of the critical specific aeration demand per unit permeate flow $SAD_{p,Crit}$, which can serve as a baseline for system operation. In practice, a constant $SAD_{p,Crit}$, adjusted by an appropriate safety factor, can be used to maintain stable performance while minimizing unnecessary energy input. This offers a simple and practical framework for implementing adaptive air scour control using only routinely collected operational data, and it sets the foundation for further optimization strategies developed in Chapter 3.

The results of the investigations briefly summarized above have been published in a peer-reviewed journal (Jun et al. 2024).

Chapter 3 Development of a Dual-Metric Operating Model for MBRs

3.1 Introduction

This chapter builds on the results from Chapter 2 to advance the overall objective of this research: to minimize the air scour energy required for sustainable membrane operation in the MBR process. Chapter 2 established a critical hydrodynamic relationship defining the conditions necessary to avoid rapid solids accumulation. Specifically, the model demonstrated that the minimum ratio of air scour airflow ($Q_{A,Crit}$) to the permeate flow (Q_P), the critical air scour ratio, is linearly related to the MLSS concentration and the total resistance (R_T), characterized by the empirically determined proportionality constant, K_{Lim}.

In practice, the MLSS concentration is often dictated by the required level of biological treatment. While operating at the lowest feasible MLSS minimizes aeration, this variable is typically constrained. Therefore, R_T (the inverse of permeability) emerges as the primary controllable variable for further air scour optimization. Maintaining low R_T directly minimizes the necessary air scour intensity. Thus, achieving further energy efficiency hinges on a deeper understanding of the factors governing R_T, specifically, the dynamics and characteristics of membrane fouling.

Effective management of membrane fouling is critical, yet complex. Fouling is often categorized into reversible and irreversible forms (Ladewig and Al-Shaeli 2017); however, this distinction is dynamic and operationally dependent rather than absolute. Reversible fouling (cake fouling) involves the deposition of sludge flocs on the membrane surface and is typically managed with mechanical cleaning (e.g., air scouring or BP). Note, if the rate of deposition

consistently exceeds the rate of removal, this 'cake' layer accumulates (Jørgensen et al. 2014; Miller et al. 2014). Under sustained pressure (high TMP), this accumulated layer can undergo physical changes, such as compression and consolidation (Bugge et al. 2012; Díaz et al. 2024; Jørgensen et al. 2014), making it operationally persistent and effectively irreversible. Irreversible fouling (e.g., pore blocking, strongly adhered materials) is inherently more tenacious and requires chemical intervention (Ehsani et al. 2021; Guo et al. 2012; Judd 2008).

These different fouling dynamics necessitate distinct mitigation approaches, highlighting a critical limitation of relying solely on the K value. The K value quantifies hydrodynamic stress but cannot diagnose the nature of the accumulated fouling. Crucially, persistent or irreversible fouling is often unresponsive to increased aeration. Attempting to manage all fouling scenarios solely through hydrodynamic adjustments (i.e., increasing air scour) is therefore often ineffective and leads to significant energy waste. A diagnostic capability to quantify various fouling components and track their dynamic transitions is essential to guide targeted interventions and optimize cleaning strategies.

To address this challenge, this chapter investigates the fouling dynamics of a full-scale, highly loaded MBR facility (Plant C). This facility actively employs back-pulsing (BP) and maintenance cleaning (MC), providing the high-frequency operational data necessary for detailed analysis. To interpret this data, we apply a novel dual-metric approach that integrates two complementary components: the K value, serving as the hydrodynamic index, and diagnostic resistance components derived from BP cycles. This resistance diagnosis provides crucial insight by operationally differentiating between persistent fouling and dynamic cake accumulation.

The objective of this chapter is to leverage this dual-metric approach to characterize the dynamic interplay between hydrodynamic stress (K) and the evolving fouling state (resistance

components) under high-load conditions. Based on these insights, we develop a diagnostic control matrix, structured based on the key indicators (e.g., K value and resistance diagnostics) with empirically determined thresholds delineating different operational zones. This framework aims to guide sustainable air scouring strategies and support data-informed, proactive operational management of the MBR system.

3.2 Theoretical Framework and Metric Definition

3.2.1 The Hydrodynamic Index with Thresholds

The K value serves as a hydrodynamic index that implicitly reflects the balance between shear-induced back-transport and convective deposition. Empirically derived K value thresholds are utilized to characterize transitions in fouling behavior and define distinct system responses. Two critical thresholds are defined: First, the Limiting K value (K_{Lim}), empirically observed in Chapter 2, represents the critical hydrodynamic boundary required to prevent severe fouling conditions (the limiting condition). Operating at or below K_{Lim} poses a high risk of rapid system deterioration, which can lead to sludging if not promptly addressed. Second, the Target K value (K_{Targer}) is defined as the hydrodynamic breakpoint marking the onset of a noticeable increase in resistance. K_{Targer} serves as a practical operational threshold corresponding to the fouling transition zone, a state where fouling accumulation accelerates but remains manageable.

3.2.2 Fouling State Diagnostics (Analysis of Resistance Components)

To diagnose the fouling state, R_T is decomposed into specific components based on a resistance-in-series model (Equation 3.1). R_T comprises reversible fouling (R_{cake}), irreversible fouling (which includes strongly adhered materials (R_{if}) and pore narrowing or blocking (R_{pore})) and intrinsic membrane resistance (R_m).

$$R_T = R_{cake} + R_m + R_{Pore} + R_{if} \quad \text{Equation (3.1)}$$

The analysis utilizes data from BP cycles to quantify these components in-situ. Diez et al. proposed that back-pulsing resistance (R_{BP}) primarily reflects R_m and R_{pore} (Diez et al. 2014). While acknowledging this foundational work, this study extends the interpretation of R_{BP}. Here, R_{BP} is utilized to quantify the sum of R_m, R_{pore}, and persistent external irreversible fouling, R_{if} as shown in Equation 3.2.

$$R_{BP} = R_m + R_{Pore} + R_{if} \quad \text{Equation (3.2)}$$

This extended interpretation of R_{BP} is based on the rationale that BP rarely achieves complete removal of all accumulated foulants. Foulant removal is inherently partial, constrained by the specific duration and intensity of the applied BP protocol. Strongly adhered external materials and internal pore constrictions developed during permeation may resist the applied BP protocol. Consequently, R_{BP} serves as the operational metric for persistent or 'intact' fouling. R_{cake} is calculated as the difference between total resistance during permeation (R_T) and R_{BP} ($R_{cake} = R_T - R_{BP}$). An increase in R_{cake} signifies the dynamic accumulation of a thickening cake layer during the permeation cycle. As this layer develops, it provides additional consistent hydraulic resistance and undergoes compaction, making it increasingly difficult to manage solely through mechanical cleaning (e.g., air scour and BP).

The accumulation of all these resistances (both R_{BP} and R_{cake}) contributes to an overall increase in R_T. Under constant flux operation, this necessitates higher TMP. This elevated pressure increases the localized convective stress near the membrane surface, leading to

accelerated foulant attachment. This distinction, based on the measurable response to back-pulsing, provides the necessary insights to guide targeted interventions.

3.3 Methods

3.3.1 Full-Scale MBR System Evaluated

A year-long historical dataset (February 2024–February 2025) from a full-scale MBR facility treating largely domestic wastewater was analyzed and used to develop the dual metric membrane control framework presented here. The plant practices BP and MC to manage the development of R_T, and recovery clean (RC) as needed. To clearly identify operational trends and system responses, the entire dataset was segmented into five distinct periods reflecting different operating conditions. Given the dynamic fluctuations and inherent noise typical in full-scale MBR systems, extensive data processing and feature engineering were performed, as detailed in the subsequent sections. An overview of the MBR system is provided in Table 3.1, and the information for each analysis period is defined in Table 3.1.

Table 3.1: Summary of Operational Conditions

Items	Description	Note
Membrane type	Corrugated flat sheet	
Number of trains	4	
Surface Area per Train (m^2)	17,419	Per Train
TMP (kPa)	24.70 (±9.28)	Mean (±std)
Flux [LMH][a]	20.16 (± 2.64)	Mean (±std)
MLSS [g/L]	7.29 (± 1.65)	Mean (±std)
Specific Air Demand per Membrane Area (SAD_m) ($m^3/m^2/hr$)	0.21 (± 0.03)	Mean (±std)
Specific Air Demand per Permeate (SAD_p) (dimensionless)	10.49 (± 1.10)	Mean (±std)

Return Activated Sludge (RAS) to Permeate Flow Ratio (dimensionless)	4.88 (± 0.51)	Mean (±std)
Permeation/Back-pulse Cycle Ratio[b]	4:1 (1:1 to 6:1)	Mean (Min to Max)
Back-pulse Flux (LMH)	6 (10.3)	Mean (Max)
Chemical Cleaning Frequency (day) Hypochlorite Citric Acid	 4 (1 to 8) 19 (4 to 14)	 Mean (Min to Max) Mean (Min to Max)
Temperature	23 (± 3.1)	

[a] LMH: Liters per square meter per hour.

[b] Cycle Ratio: Refers to the ratio of permeation cycles to back-pulse cycles. Each permeation cycle was 5 minutes, and each back-pulse cycle was 1 minute. For example, a 4:1 ratio means 20 minutes of permeation followed by 1 minute of back-pulse.

Table 3.2: Segmented Historical Dataset

Phase	Data Range	Features
P1	Feb. 01, 2024 – May 01, 2024	High MLSS loading
P2	May. 02, 2024 – Jul 17, 2024	Subsequent limiting conditions
P3	Jul. 18, 2024 – Sep 27, 2024	Stable condition followed by upset
P4	Sep. 28, 2024 – Nov. 30, 2024	After RC, another cycle
P5	Dec. 01, 2024 – Feb. 13, 2025	Stressing condition with elevated R

3.3.2 Data Acquisition and Processing

High-frequency sensor data (recorded at 500-millisecond intervals), including TMP, permeate flow rate, air scour flow rate, and Return Activated Sludge (RAS) flow rate from the membrane tank to the bioreactor, were obtained from the plant Supervisory Control and Data Acquisition (SCADA) system. To reduce computational load while preserving essential information, the data were resampled at 15-second intervals. This resampled data was then processed using an extraction algorithm (detailed in Appendix B) to clean the signals and isolate individual permeation, back-pulsing, and cleaning cycles. Separately, other key parameters like MLSS and wastewater temperature were recorded periodically, resulting in datasets with gaps.

Manually recorded temperature data was linearly interpolated on a daily basis to create a continuous time series.

Handling the MLSS data required particular care, as its concentration varies not only temporally but also spatially within the membrane tank due to solids thickening dynamics (Cho and Fane 2002; Romero and Davis 1988). In flat-sheet membranes, as permeation occurs, the solids concentration increases along the height of the membrane tank. Using an MLSS measurement from the bioreactor to reflect that in the membrane tank would underestimate the actual concentration in the membrane tank. Since direct experimental measurement of RAS concentration is often unavailable, an arithmetically averaged MLSS concentration within the membrane tank was computed using a mass-balance-based derivation (Equations 3.3–3.6). For periods with missing or unreliable sensor readings (due to drift or malfunction), feed MLSS concentrations were first imputed using interpolation, under the assumption that MLSS changes gradually over a daily period. The mean membrane tank MLSS was then computed using the available data, as follows:

$$\left(Q_{perm} + Q_{RAS}\right) \cdot X_{ML} = Q_{RAS} \cdot X_{RAS} \qquad \text{Equation (3.3)}$$

$$X_{RAS} = \frac{\left(Q_{perm} + Q_{RAS}\right) \cdot X_{ML}}{Q_{RAS}} \qquad \text{Equation (3.4)}$$

$$X_{tank,avg} = \frac{X_{ML} + X_{RAS}}{2} \qquad \text{Equation (3.5)}$$

$$X_{tank,avg} = \frac{X_{ML} + \frac{\left(Q_{perm} + Q_{RAS}\right) \cdot X_{ML}}{Q_{RAS}}}{2} = \frac{\left(Q_{perm} + 2Q_{RAS}\right) \cdot X_{ML}}{2Q_{RAS}} \qquad \text{Equation (3.6)}$$

$$\frac{X_{tank,avg}}{X_{ML}} = \frac{1}{2}\frac{Q_{perm}}{Q_{RAS}} + 1 = \frac{1}{2}\frac{1}{RAS\ Q} + 1 \qquad \text{Equation (3.7)}$$

Where $X_{tank,avg}$ is the mean MLSS concentration in the membrane tank (g/L), X_{ML} is the feed MLSS concentration (g/L), X_{RAS} is the RAS concentration (g/L), Q_{perm} is the permeate flow rate (m^3/day), Q_{RAS} is the RAS flow rate (m^3/day), and RAS Q is the dimensionless ratio of RAS flow rate to permeate flow rate (Q_{RAS}/Q_{Perm}).

Finally, the processed sensor data were combined with the mean MLSS and temperature data. This dataset was then used to compute the hydrodynamic index (K), resistance values, and fouling rates, using the algorithms detailed in Appendix B. This process was crucial for creating a robust dataset that enabled a comprehensive analysis across multiple time scales, from high-resolution data capturing transient events to low-resolution data revealing long-term trends. Daily average statistics are primarily used in this study to assess long-term trends, as this approach effectively smooths out the diurnal variability typical of municipal wastewater influent, thereby clarifying underlying operational conditions and system responses. All data processing and analysis were performed in MATLAB (R2024b), and all variables were converted to standard SI units.

3.3.3 Calculation of Metrics and Application

3.3.3.1 Hydrodynamic Index

The hydrodynamic Index, K value, was calculated using a rearranged form of Equation 2.2 using the actual operating conditions at a particular point in time, as follows:

$$K = \frac{Q_A}{Q_P} \cdot \alpha_s \cdot \frac{1}{\mu_{app} \cdot MLSS_{tank,avg} \cdot R_T} \qquad \text{Equation (3.8)}$$

where K is the hydrodynamic index (m·s/kg), Q_A is the actual air scour flow rate (m^3/hr), and the other parameters are as defined previously.

By comparing the operational K value against predefined thresholds (e.g., K_{Lim}), the hydrodynamic state of the MBR can be characterized relative to a spectrum of predictable fouling behaviors. For instance, an operational K value greater than the empirically determined K_{Lim} indicates that the air scour energy input exceeds the minimum required to prevent rapid solid deposition (sludging). This comparison, therefore, serves as a real-time diagnostic tool to assess the sufficiency of the air scour and to quantify the operational safety margin. For this study, the values for K_{Lim} and K_{Target} were set to 1.2×10^{-8} m·s/kg, as established in Chapter 2, and 2.0×10^{-8} m·s/kg, respectively.

3.3.3.2 Resistance Computation

To facilitate straightforward tracking of these resistance trends with practical units (e.g., kPa/LMH, where LMH is liters per square meter per hour), a normalized resistance value rather than the units derived directly from Darcy's Law (e.g., m^{-1}) is used. A temperature correction factor is further applied to accurately account for the significant influence of variations in permeate viscosity due to seasonal temperature changes. The general form of the equation is as follows:

$$R = \frac{TMP \cdot \mu_{water,20°C}}{J \cdot \mu_{water,T}} \qquad \text{Equation (3.9)}$$

where 'R' generally represents resistance (kPa/LMH), TMP is the Transmembrane Pressure (kPa), J is the permeate flux (LMH), $\mu_{water,T}$ is the water viscosity at the operating temperature (T), and $\mu_{water,20°C}$ is the water viscosity at the reference temperature of 20°C.

Because R_T and R_{BP} are calculated from data measured at different times (during the permeation and BP cycles, respectively), a direct, instantaneous comparison between them is not feasible. To enable a meaningful comparison for calculating R_{cake}, daily averaged data is used instead. Therefore, the resulting daily values in this study represent the residual resistance that persists after a full day of operational dynamics and cleaning protocols. Consequently, on days with more challenging operational conditions, these resistance values are expected to be higher.

3.3.4 Evaluation of Fouling Rate

The fouling rate (FR) was calculated as the rate of TMP increase. This was first computed for each 15-second interval within a permeation cycle and then averaged on a daily basis, a method enabled by the high-resolution data preparation described previously. Measuring the rate of change of TMP (expressed as dTMP/dt) offers a direct basis for comparing different operational conditions, as it isolates the response of the system to a single, easily interpretable variable, unlike measuring the rate of change of resistance. To ensure a consistent comparison independent of permeate viscosity, the raw TMP increase rate was normalized to a reference temperature of 20°C, as defined in Equation 3.10:

$$FR = \frac{\Delta TMP_{20°C}}{\Delta t} \qquad \text{Equation (3.10)}$$

where FR is the fouling rate (temperature corrected) (kPa/s), $\Delta TMP_{20°C}$ is the change in TMP over a permeation cycle, normalized to 20°C (kPa), and Δt is the time interval (s).

It is worth noting that the limiting condition for the FR, as defined in Chapter 2, was approximately 0.017 kPa/s. This value was determined at the individual cycle level, which contrasts with the results presented here which are based on daily averages. The average FR

values presented here will naturally be lower than the instantaneous values observed in individual cycles, even when some cycles exceed the limiting threshold.

3.3.5 Statistical Evaluation of Operating Categories

Statistical analysis was conducted to evaluate the categorization of operating conditions proposed by the dual-metric control framework. Specifically, the analysis evaluated whether the FR characteristics were statistically different across the defined operating regions. First, Levene's test was conducted to test for homogeneity of variances. This test was used to assess whether the variance of the FR was equal across the different operating groups (i.e., the nine regions of the control matrix in Figure 3.7). As the assumption of equal variances is often not met with complex, real-world operational data, this step was crucial for selecting the appropriate subsequent statistical test for comparing the groups. Given that the data did not meet the assumptions for parametric tests (e.g., normality and homogeneity of variance, data not shown), the non-parametric Kruskal-Wallis H test was employed. This test was used to determine if there were statistically significant differences in the median FR among the categorized operational regions. For this analysis, a p-value of less than 0.05 was considered statistically significant.

3.4 Results

3.4.1 Summary of Plant Operation

Figure 3.1 presents the daily average TMP, flux, Specific Air Demand per Membrane Area (SAD_m), and $MLSS_{tank}$, for the three operating trains throughout the observation period. Overall, the permeate flux started at approximately 15 LMH before it increased at the end of March 2024 and remained relatively stable at approximately 20 LMH. The air scouring flow rate (represented by SAD_m) gradually increased during an initial phase before being maintained at a constant level from June 2024 to the end of the study period. $MLSS_{tank}$ concentration reached a

high value above 10 g/L initially and maintained within a concentration range of 6 - 8 g/L throughout the remaining periods. The K value, starting high with clean membranes, decreased rapidly during the initial period and subsequently fluctuated around K_{Lim}, as shown by the horizontal red line. A more detail investigation of each period from P1 to P5 is highlighted below:

1. High solid mass loading (P1): During P1, the $MLSS_{tank}$ concentration was higher than 10 g/L (max 13 g/L), and once flux increased to around 20 LMH at the end of March 2024, the TMP values spiked rapidly from 10-20 kPa to 30-40 kPa. The TMP continued to increase despite decreased flux at the end of the first period. In this period, SAD_m gradually increased from 0.15 to around 0.20, but did not mitigate the situation. The K value indicated a limiting condition later in P1. RCs were conducted for all trains.
2. Subsequent limiting condition (P2): After the first RC, TMP values were lowered. However, once the flux slightly increased mid-period, the K value declined to the K_{Lim} boundary. Consequently, the TMP started to increase rapidly, reaching TMP values around 50 kPa. During this period Train 4 had two RC's. The TMP gradually decreased during the later portion of P2; these profiles corresponded to the gradual flux relaxation and $MLSS_{tank}$ decrease, also showing increasing trend in K.
3. Stable operation (P3): Operational conditions were highly stable, even with relatively higher permeate flux, for more than two months. From late September, Trains 3 and 4 showed increasing TMP trends, which were followed by RCs for those two trains.
4. Stressing operations (P4 and P5): The remaining periods showed more fluctuating conditions. In P4, there was another upset in Trains 3 and 4, characterized by K

values falling below the K_{Lim} threshold; this was mitigated even without RC. In P5, the K value remained generally below the K_{Lim}, also indicating highly stressed conditions with consistently elevated TMP values.

Notably, K consistently dropped below the K_{Lim} threshold during each of these elevated TMP periods (limiting conditions), reinforcing its effectiveness as an indicator of rapid resistance increases. Significantly, the numerical value of K_{lim} value, obtained from two other full-scale MBR systems in the Chapter 2, proved to be a consistently effective threshold in this system as well, despite the different operating conditions.

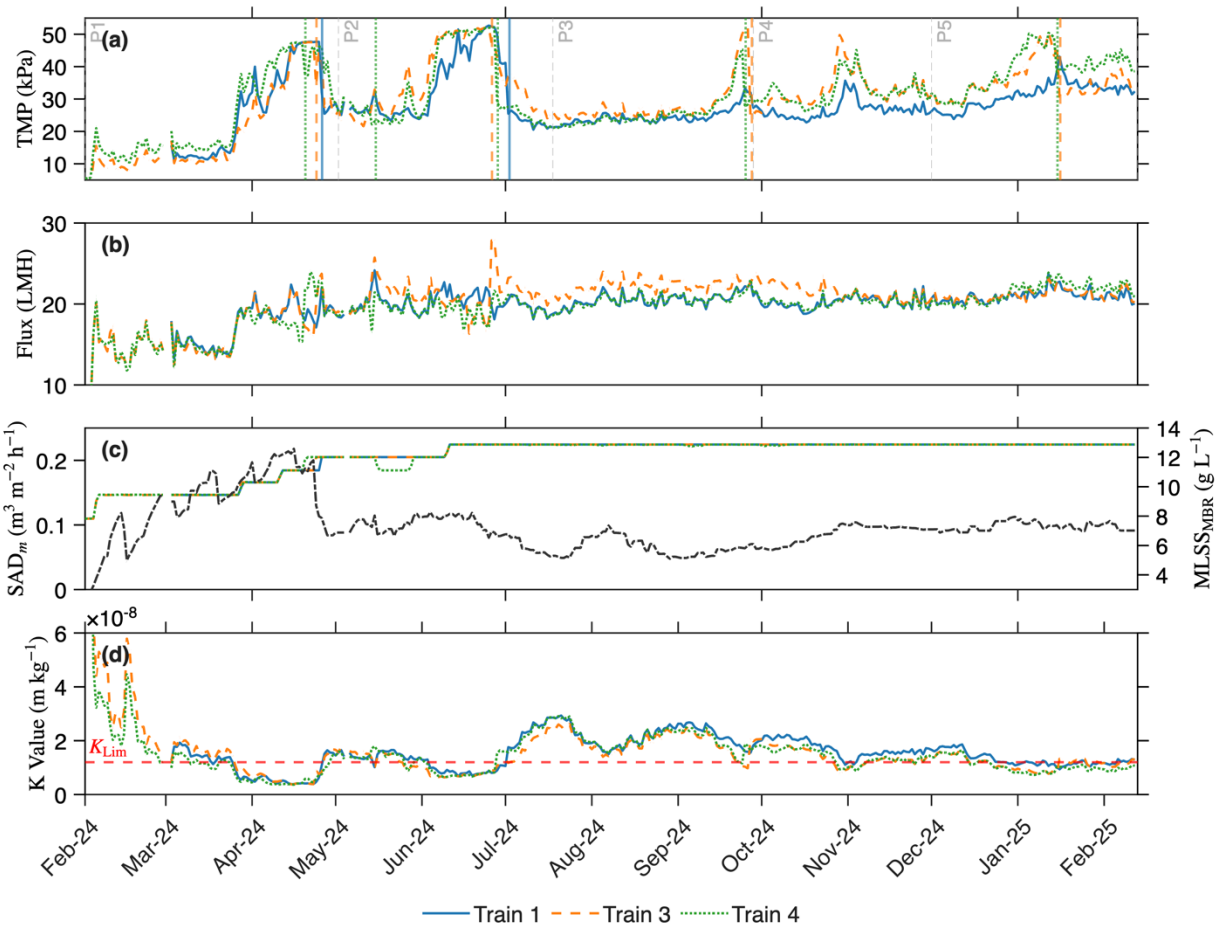


Figure 3.1: Daily average variations of key operational variables for Plant C. Panel: (a) Transmembrane Pressure (TMP) with five segregated periods (P1-P5) indicated, (b) permeate flux, (c) Specific Air Demand per Membrane area (SAD_m) and mean MLSS concentration in the MBR tank ($MLSS_{tank}$), and (d) the hydrodynamic index (K). The horizontal red dashed line in the panel (d) indicates the limiting value of K (K_{Lim}).

Figure 3.2 presents daily average trends in R_T, R_{BP}, and R_{cake} over the operating period. R_T in all three operating trains began to increase rapidly in mid-March and, by the time back-pulsing began on April 9, 2024, both R_{BP} and R_{cake} were already elevated in all trains. Resistance data from MC events was interpolated to characterize the R_{BP} during this pre-back-pulsing period. The resulting trend for both resistance types suggests a rapid increase from the end of March. This corresponded to the increased flux conditions, suggesting the solid flux loading at that period was unsustainable, even though the flux itself was not spiking. Train 4 had a higher R_{BP} from the beginning and showed a faster increase in resistance than the other trains. RCs conducted at the end of P1 and again at the end of P2 reduced R_T, but not to the low levels in the early phase.

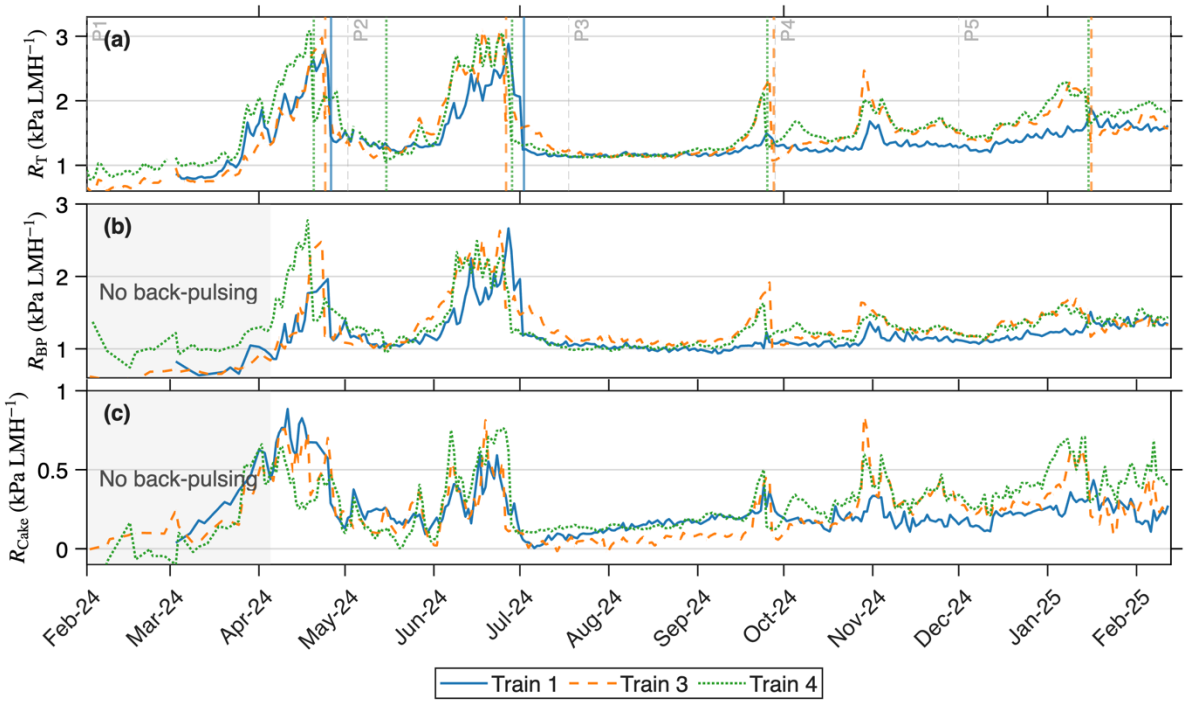


Figure 3.2: Daily averaged variation of resistance components. Panel: (a) total resistance (R_T), (b) back-pulsing resistance (R_{BP}), and (c) cake resistance (R_{cake}). Vertical lines denote recovery clean events, color-coded by train. (Blue: Train 1; Orange: Train 3; Green: Train 4).

From July (P3) onward, resistance levels decreased and remained stable until late September, when Trains 3 and 4 again exhibited rapid resistance increases, followed by

additional RCs. From October (P4) onward, the resistance baseline remained elevated and exhibited further fluctuations in late October and late December 2024, which were also followed by RCs. Notably, the latest RC did not reduce the resistance level as effectively as previous cleans, suggesting that more recalcitrant fouling had progressed in the system during the extended period of elevated resistance.

A pattern emerged during periods of resistance increase: an initial, rapid rise in R_{BP} was consistently followed by a noticeable increase in R_{cake} a few days later. This observation suggests a fouling pathway, particularly for a system operating from a clean baseline, where an increase in R_{BP} initiates the limiting condition. The resulting localized resistance likely increased local flux and established conditions favorable for subsequent, rapid cake layer accumulation (Bacchin et al. 2005; Le-Clech et al. 2006; Miller et al. 2014; Wang and Wu 2009). Moreover, as these limiting conditions were repeated, the baseline of both resistance components became progressively elevated. This indicates the formation of more permanent, irreversible fouling, which degraded system hydrodynamics and increased susceptibility to future fouling events.

3.4.2 Relationship Between Hydrodynamic Index (K) and Total Resistance (R_T)

Figure 3.3 correlates the daily average R_T with the corresponding daily average value of the hydrodynamic index (K) for the three membrane trains. Their temporal progression is depicted using the color scale. Two thresholds for K values are drawn, marking transition points in the relationship between K and R_T. The first, K_{Lim} indicates a point below which R_T increases rapidly. A second, K_{Target} marks the onset of fouling progression.

The relationship between these K thresholds and fouling progression reveals several key insights. Operating conditions corresponding to K values above K_{Target} result in a minimal increase in R_T, suggesting sustainable operation. As K decreases below K_{Target}, a linear increase

in R_T is typically observed. While the specific fouling progression profile varies across operating periods (indicated by colors), this general trend is consistent, suggesting that hydrodynamic conditions are becoming insufficient to the point that daily mechanical cleaning protocols cannot fully remove the accumulating foulant layer. A more critical transition occurs when K falls below K_{Lim}. At this point, a rapid and significant increase in R_T is observed, signifying a severely compromised hydrodynamic state that can induce sludging and unsustainable fouling, as discussed previously.

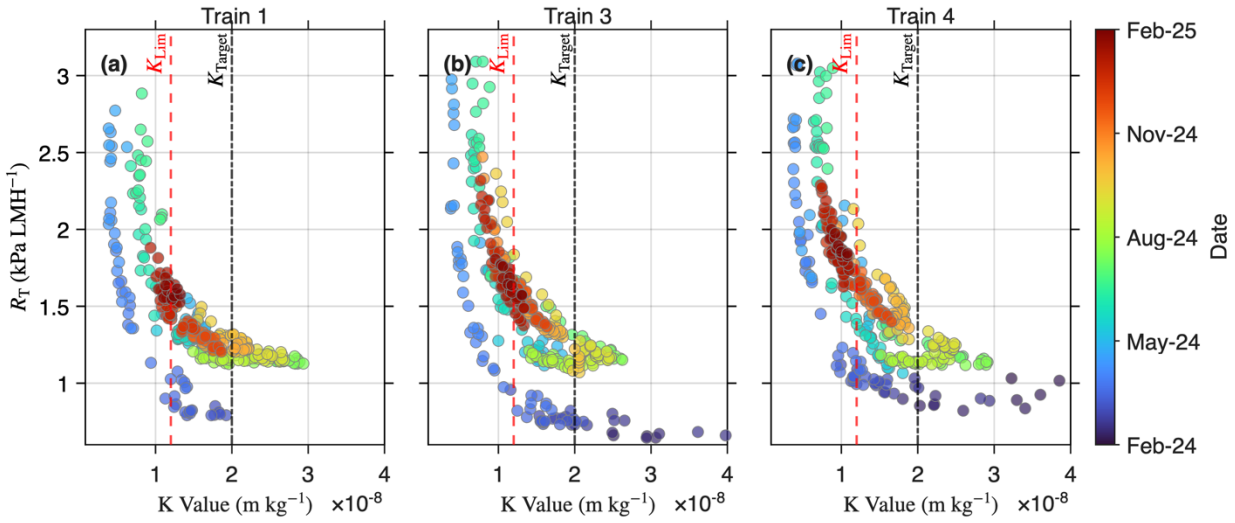


Figure 3.3: Daily Average Correlation between the Hydrodynamic Index (K Value) and Total Resistance (R_T) for Trains 1, 3, and 4 (panel (a), (b), and (c) respectively): Data points are color-coded to indicate the date of operation, showing the temporal progression of the system's state. The solid red vertical line represents the limiting K value (K_{Lim}), and the dashed black vertical line represents the target K value (K_{Target}).

Interestingly, during the initial operating period (P1: February to March; blue color points), R_T was relatively low even for K values nearing K_{Lim}. These low K values were due to high MLSS concentrations, albeit with comparatively lower flux. This suggests that, while the value of K indicates a potentially vulnerable state, the hydrodynamic conditions might have remained sufficiently robust to initially prevent rapid fouling progression. Once the value of K dropped below K_{Lim}, however, these early-period data exhibited the same characteristic sharp increase in R_T observed in other periods. This consistent behavior below K_{Lim}, despite variations

in the baseline fouling levels across the different operating periods, underscores the general applicability of the K_{Lim} threshold. Nevertheless, the nuanced fouling responses, particularly that different operating periods exhibit slightly different R_T variations for similar K values, highlight the need for a detailed analysis of the resistance components.

3.4.3 Analysis of Resistance Responses

Figure 3.4 presents correlations between the components of R_T (R_{BP} and R_{cake}) and R_T, with data points color-coded by corresponding K value. Horizontal dash-dot lines denote empirically determined resistance thresholds, marking inflection points in resistance profiles. A 1:1 reference line is provided for comparison. The slopes of these correlation plots characterize the relative contribution of each component to overall resistance development.

The resistance profiles exhibit distinct phases defined by these thresholds:

1. Gradual Fouling (Phase 1): Below the first thresholds (R_{BP} < 1.2 kPa/LMH; R_{cake} < 0.2 kPa/LMH), R_{BP} increases proportionally with R_T, indicating it is the primary contributor, and that R_{cake} values remain low.
2. Cake Development (Phase 2): Between the first and second thresholds, R_{cake} increases linearly with R_T. Concurrently, the slope of R_{BP} versus R_T decreased, signifying that R_{cake} accounts for a larger fraction of the incremental increase in R_T.
3. Consolidation (Phase 3): Above the second thresholds (R_{BP} > 1.6 kPa/LMH; R_{cake} > 0.5 kPa/LMH), the contribution of R_{cake} diminishes, and R_{BP} again becomes the dominant contributor, accelerating rapidly.

These trends suggest a gradual and cyclical fouling mechanism (Pathway A). Progressive accumulation of irreversible fouling (phase 1) likely creates heterogeneous permeability across the membrane surface, imposing an elevated local flux on the permeable (less-fouled) areas by

cascading further increase of local flux (Flux Redistribution). This condition forces the system to operate beyond its sustainable flux limit, leading to the development and thickening of a cake layer (phase 2). Subsequently, compression of this cake layer under increasing TMP appears to trigger a transition (phase 3). The accelerated increase in R_{BP} suggests that the cake layer deforms, potentially forcing particles into membrane pores or deeper compacted regions (Du et al. 2017; Meng et al. 2005; Shen et al. 2015). This marks a limiting transition point where cake fouling begins to transform into irreversible fouling.

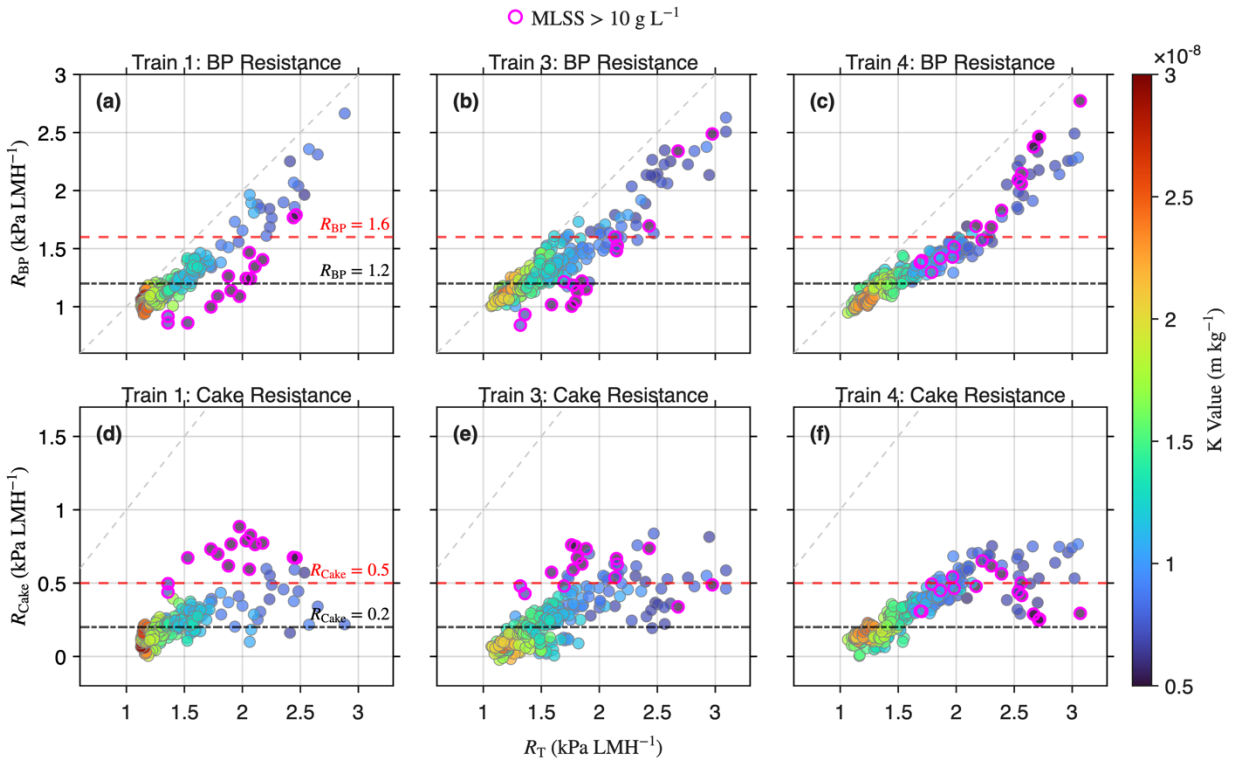


Figure 3.4: Correlation of resistance components with total resistance (R_T) for Trains 1, 3, and 4, colored by the corresponding K value. The top row (panels (a), (b), (c)) shows Back-pulsing resistance (R_{BP}) vs. R_T, while the bottom row (panels (d), (e), (f)) shows Cake resistance (R_{cake}) vs. R_T. Horizontal dash-dot lines represent empirically determined thresholds for each resistance component. The solid red line is a 1:1 reference line. Pink highlighted circles indicate high solid loading conditions (MLSS > 10g/L).

Analysis of the temporal dynamics across the trains provides a context regarding an alternative fouling progression pathway, particularly under high solid loading stress. At the commencement of monitoring in February 2024, the initial resistance hierarchy reflected varied operational histories (Figures 3.1 and 3.2). This difference in fouling maturity is attributed to the

plant's start-up order; Train 4 was used to initiate the biology during the plant start-up and was thus exposed to 'young sludge' from the biological reactor, which is known to be highly fouling. This resulted in higher initial irreversible resistance (R_{BP}) compared to Trains 1 and 3, which started later. When high solids loading conditions ($MLSS_{tank}$ > 10 g/L) began in mid-March, resistance increased across all trains. Notably, Train 4, having the highest initial resistance, exhibited the most sensitive response in increasing R_T (Figure 3.2), indicating that the prior state of fouling (fouling maturity) dictates sensitivity to operational stress. Detailed resistance component data (R_{BP}, R_{cake}), derived from intermittent BP initially and consistent application from early April onward, reveals the nature of the fouling state during the high solid loading event. In Figure 3.4, during this period (highlighted as pink edges), the severity of R_{BP} followed the established order of maturity: Train 4 > Train 3 ≈ Train 1. Intriguingly, R_{cake} showed the inverse trend: Train 1 ≈ Train 3 > Train 4.

This inverse relationship suggests an alternative fouling progression sequence driven by high solids loading (Pathway B), where R_{cake} leads to increased R_{BP}. The trains represent snapshots of different responses with regard to fouling maturity. Train 1 and Train 3, with the lower fouling resistance, responded primarily through rapid cake accumulation (high R_{cake}, low R_{BP}). Conversely, Train 4 represents a mature state where the cake transitioned faster into a compacted, irreversible layer (high R_{BP}, low R_{cake}) due to higher resistance (higher pressure). Train 3 exhibits characteristics similar to Train 1, though somewhat intermediate. Essentially, under similar external operational stress, the system response varied according to the existing fouling maturity. The extensive cake formation induced by high solids loading serves as a direct precursor to consolidated irreversible fouling, which accelerates as the pre-existing fouling layer matures.

The K value colormap provides insight into the hydrodynamic conditions associated with these patterns. When the K value drops below K_{Target} (2.0×10^{-8} m·s/kg), the system's fouling state typically crosses the first resistance thresholds. This event marks the transition from Phase 1 to Phase 2 and signals the initiation of accelerated cake fouling development. Similarly, when hydrodynamic conditions worsen and the K value falls below K_{Lim} (1.2×10^{-8} m·s/kg), the fouling progression tends to cross a second resistance threshold, suggesting the onset of fouling layer consolidation. Notably, this transient behavior is observed regardless of the initial fouling pathway.

3.4.4 Development of Fouling Resistance Components: Trajectory Analysis

To further elucidate the observed fouling dynamics, the daily trajectories of R_{BP} versus R_{cake} over several distinct periods were analyzed (Figures 3.5 and 3.6). The daily averaged K value is indicated by the colormap. The empirically derived resistance thresholds for R_{BP} and R_{cake} (from Figure 3.4) are shown as grey dash-dot lines. Asterisks denote the first day of each period, squares indicate the last day, and diamonds mark RC events. The diagonal lines represent iso-resistance thresholds ($R_T = R_{BP} + R_{cake}$).

3.4.4.1 Pathway A Visualization

Figure 3.5 illustrates the trajectories from July 2024 onward (P3 to P5), when Pathway A became dominant. In this pathway, the increase in R_{BP} typically precedes or occurs concurrently with the increase in R_{cake}. During stable operation (Phase 1 in panels a-c), the system remained below the first thresholds, with the values of K generally above K_{Target}. As fouling progressed, resistances began to rise, leading to increased operational stress. Notably, the transition to accelerated fouling (Phase 2) in Pathway A was triggered when the combined resistance crossed the first iso-resistance threshold (1.4 kPa/LMH), which subsequently accelerated R_{cake}

accumulation. This is particularly evident in panel b, where initial R_{cake} was minimal. Crossing the first R_{cake} threshold alone did not appear critical (panel a). However, the level of residual R_{cake} predisposed the system to earlier acceleration; in panel c, the iso-resistance threshold was reached sooner due to higher initial R_{cake}. Once acceleration started, the system followed a characteristic diagonal trajectory toward the second iso-resistance threshold lines, necessitating RC as the system approached limiting conditions (Phase 3).

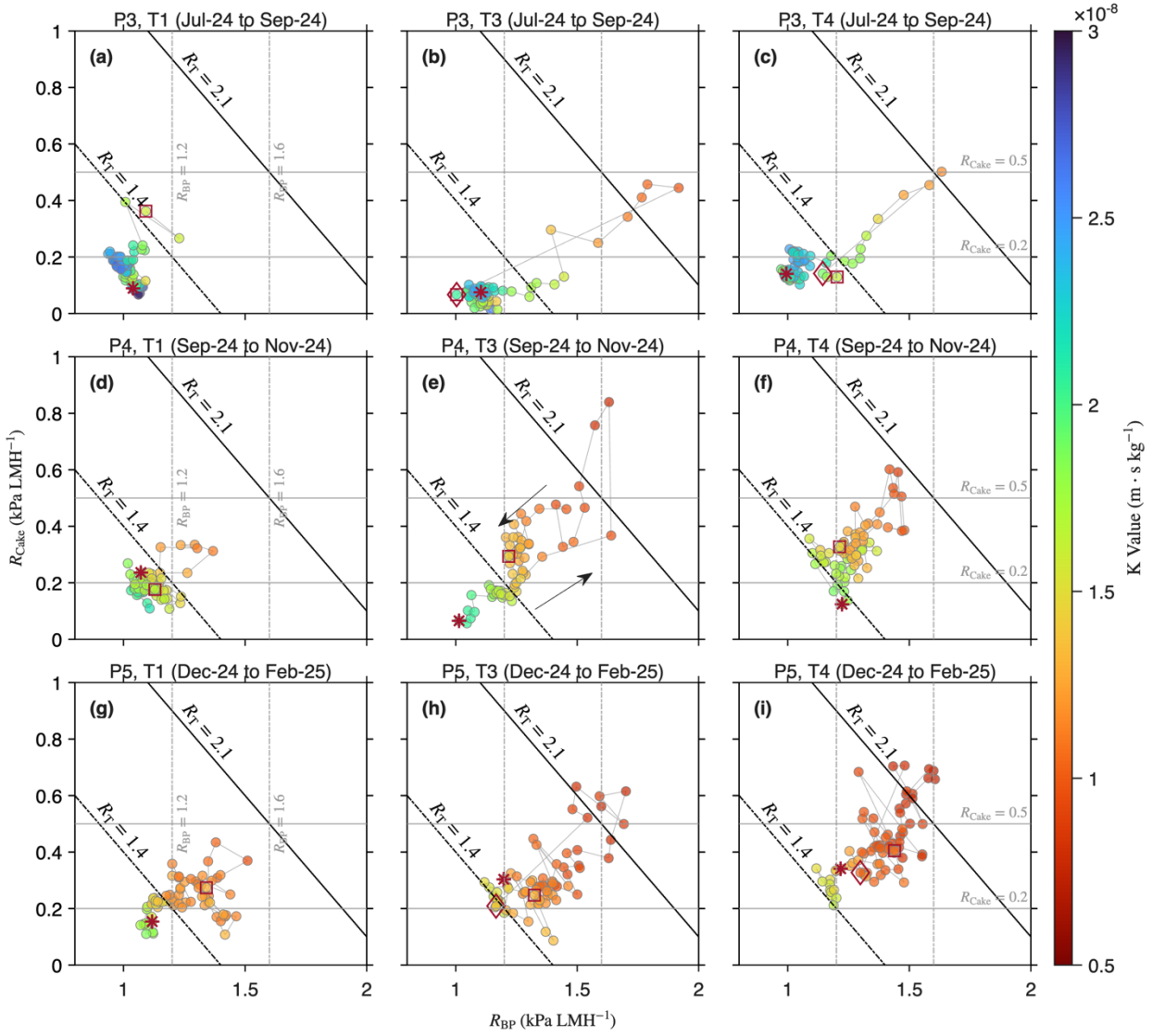


Figure 3.5: Periodic trajectory analysis (Period 3-5: July 2024 onward) of R_{BP} versus R_{cake} for Trains 1, 3, and 4, illustrating Pathway A. Data points are colored by the K value (m·s/kg). Dash-dot lines represent the resistance thresholds. Diagonal lines are iso-resistance reference lines. Each panel (a-l) represents a distinct operational period.

Asterisks denote the first day of each period, squares indicate the last day, and red diamonds mark recovery clean events.

Elevated baseline resistances fundamentally lower the sustainable operating capacity. Panels d-f illustrate subsequent cycles for Pathway A, with a higher degree of fouling. Similarly, once resistance crossed the first iso-resistance threshold, fouling accelerated. In panel e (black arrows), after the resistance upset was mitigated without RC, R_{cake} remained elevated, indicating a hysteresis effect where the severe fouling pathway is not fully reversible without rigorous cleanings. Furthermore, sustained operation under limiting conditions resulted in higher and more persistent residual resistances, even after RCs (e.g., panels g-i), rendering the system highly sensitive to subsequent stress. This underscores the necessity of preventing entry into limiting conditions or implementing immediate corrective actions if they occur.

3.4.4.2 Pathway B Visualization

Figure 3.6 illustrates the trajectories during the initial operating period (February – July 2024, P1 and P2). This period was characterized by high mass loading and subsequent limiting conditions, leading to the dominance of the Pathway B mechanism where R_{cake} escalation precedes R_{BP} increase. The trajectories in panels a-c demonstrate the initiation of Pathway B under high solids loading stress ($MLSS_{tank}$ > 10 g/L). In Trains 1 and 3 (panels a and b), operation began with low R_{BP}. The initial response was a rapid escalation of R_{cake}, while the increase in R_{BP} was minimal until R_{cake} approached its second threshold. Notably, this also crossed the first iso-resistance threshold, after which the trajectory slope shifted, indicating a concurrent increase in both R_{BP} and R_{cake}. Crucially, when the overall resistance approached and surpassed the second iso-resistance threshold, the trajectories exhibited a distinct shift to the right. This indicates the transition of the extensive cake layer into R_{BP} (consolidation and

compression). While resembling the final stages of Pathway A, this case led to more severe limiting conditions.

At the end of May 2024, RCs were conducted on all trains, which reduced R_T, however, the residual resistances remained elevated (panels a-c). Although MLSS levels had begun to normalize (~8 g/L) during Phase 2 (P2; panels d-f), the system entered this period with an elevated R_{BP} (near or above its first threshold). This persistent fouling, inherited from the previous upsets, rendered the system hypersensitive to operational stress.

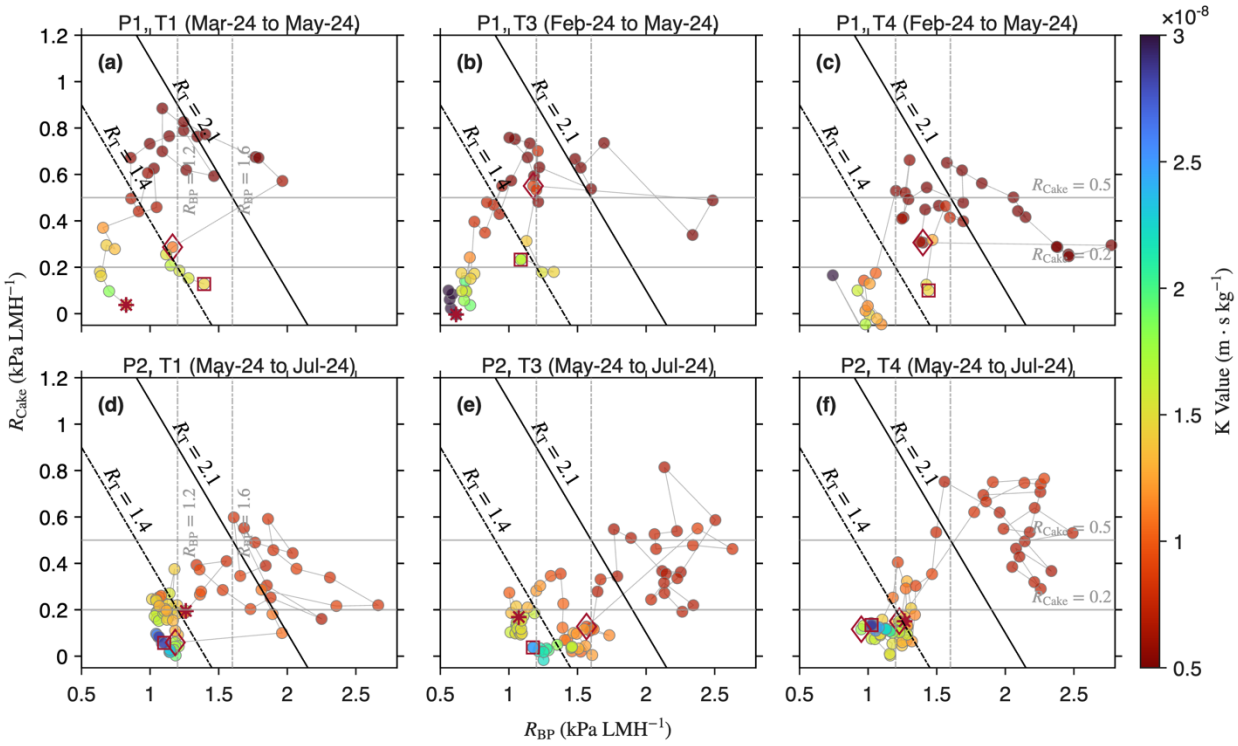


Figure 3.6: Periodic trajectory analysis (Period 1-2: Feb. – July 2024) of R_{BP} versus R_{cake} for Trains 1, 3, and 4, illustrating Pathway B. Data points are colored by the K value (m·s/kg). Dash-dot lines represent the resistance thresholds, and diagonal lines are iso-resistance reference lines. Each panel (a-f) represents a distinct operational period. Asterisks denote the first day of each period, squares indicate the last day, and red diamonds mark recovery clean events.

The subsequent fouling progression resembled Pathway A. These observations confirm that Pathway B is initiated by extensive cake formation, leading to a rapid elevation of R_{BP}, a process that would otherwise occur gradually over time. This dynamic accelerates the system's

vulnerability and the development of irreversible fouling, effectively setting the stage for the dynamics observed in Pathway A. Furthermore, this underscores that approaching the second iso-resistance line signifies entry into the limiting condition, regardless of the initial fouling pathway.

3.4.5 Categorization of Operating Conditions using Dual-Metric Control Matrix

Figure 3.7 presents a "control matrix" that categorizes operating states using daily averaged data from all trains after July 2024, focusing on the more common Pathway A scenario as it represents a more typical challenge from a plant operational perspective. The main plot (Figure 3.7a) shows a two-dimensional matrix plotting the K value on the x-axis and R_T on the y-axis. The two supplemental plots (right) provide diagnostic insight by decomposing R_T, showing R_{BP} (Figure 3.7b) and R_{cake} (Figure 3.7c) against the K value. Empirically determined thresholds for these axes (K_{Target}, K_{Lim}, and the first/second resistance thresholds) divide the matrix into nine distinct, color-coded regions, each signifying a different fouling state: Regions 1, 2, 3, 4, and 7 (red) denote limiting conditions; Region 5 (orange) indicates linear resistance development; Regions 6 and 8 (yellow) represent the onset of resistance increase; and Region 9 (green) signifies stable operation. A numerical value within each region indicates the median fouling rate (FR), defined as dTMP/dt [kPa/sec]).

The matrix effectively captures general fouling patterns. Region 9 represents stable operating conditions with the lowest median FR (0.0098 kPa/sec) (Figure 3.7a). Transitioning into the yellow zones (Regions 6 and 8) indicates increased system sensitivity and marks the onset of resistance increase, with an approximately 8% higher median FR. Region 5 (orange) shows a 35% increase in median FR compared to Region 9. The limiting regions (red) exhibit the highest FR, exceeding the stable region by over 44%. Given that these are median statistics, the

maximum FR during individual permeation cycles within these limiting zones can be substantially higher.

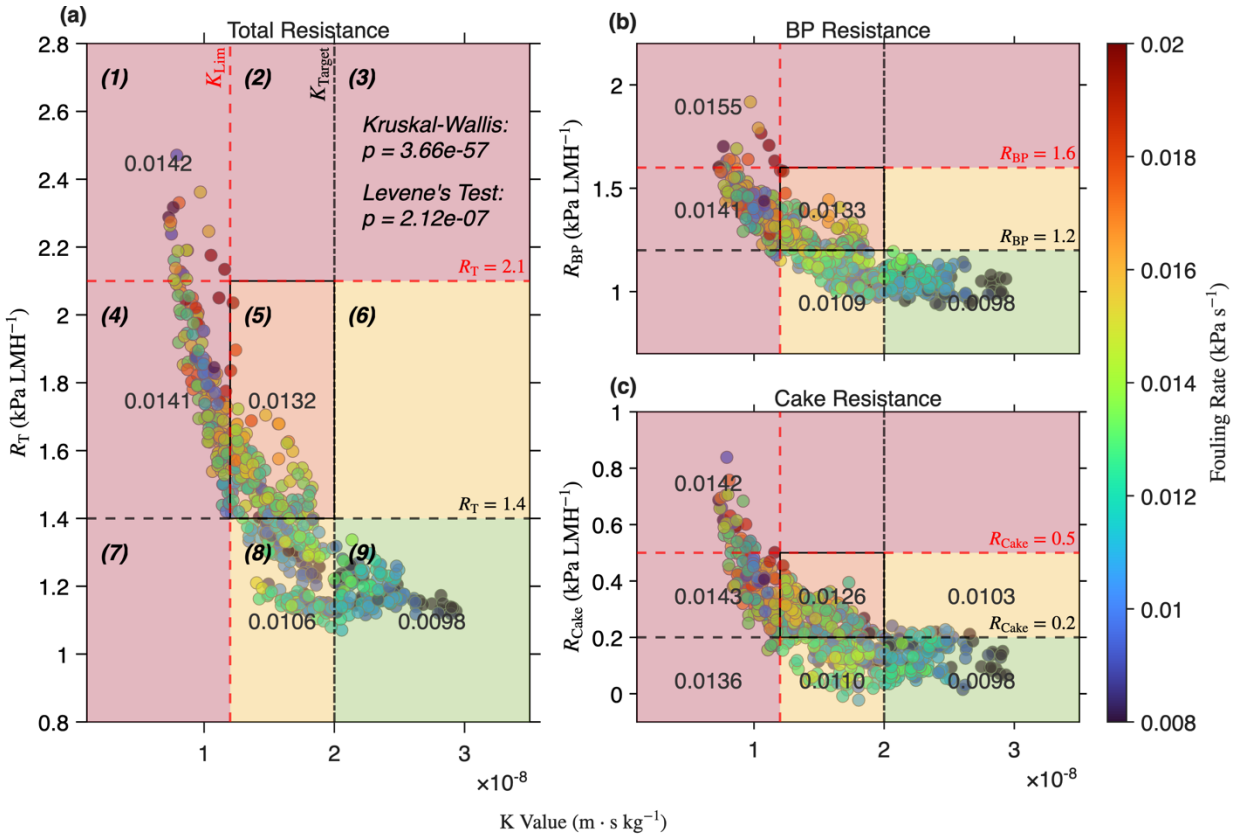


Figure 3.7: Control matrix based on the K Value and Resistance Thresholds: The main plot (panel (a)) shows Total Resistance (R_T) vs. K value. The supplemental plots show the same data space but are separated into Back-Pulsing Resistance (R_{BP}, panel (b)) and Cake Resistance (R_{cake}, panel (c)). Data points are color-coded by the fouling rate (dTMP/dt), and the median fouling rate for each of the nine operational regions is annotated.

The supplemental plots (Figure 3.7b, c)) provide diagnostic information not apparent from the R_T plot alone. For instance, while Region 9 is defined as sustainable, the R_{BP} plot (Figure 3.7b) reveals that some data points are near the first R_{BP} threshold (1.2 kPa/LMH). This indicates an underlying vulnerability; systems with higher baseline R_{BP}, even if currently stable ($K > K_{Target}$), are more sensitive to cake deposition under external operational variations. Notably, the intersection of K_{Target} and the first resistance thresholds for R_T and R_{BP} clearly separates the boundary of the stable operating window. The scarcity of data in Region 6 (High K value, High R_T or R_{BP}) indicates that these thresholds represent sharp limits; it is uncommon for

the system to operate with elevated resistance while simultaneously maintaining highly favorable hydrodynamics.

Statistical analysis on Figure 3.7a confirmed that these nine operational regions exhibit significantly different FR characteristics. The Kruskal-Wallis test validated the significant differences in median FR across the regions ($p < 0.001$), with values ranging from 0.0098 to 0.0142 kPa/sec. Furthermore, Levene's test (for homogeneity of variances) indicated significant differences in the variance of FR within each region ($p < 0.001$). This statistically validated categorization supports the use of this matrix as a "control matrix," providing a foundation for recommending specific operational actions tailored to each identified fouling state.

3.4.6 Development of Action Matrix

Diagnosing fouling conditions using the developed control matrix can effectively guide appropriate operational actions. While the nine distinct regions provide detailed insight, they can be conceptually simplified into a 2×2 management framework for practical decision-making, as illustrated in Figure 3.8. This framework is defined by the K_{Target} and the first resistance threshold. It establishes an Optimal Zone (Green; favorable hydrodynamics and low resistance), two Attention Zones (Yellow; either unfavorable hydrodynamics OR elevated resistance), and a Limiting Zone (Orange; unfavorable hydrodynamics AND elevated resistance). The emphasis is on proactive interventions in the Attention Zones to prevent progression to the Limiting Zone.

In the Optimal Zone (low resistance, favorable hydrodynamics), the primary opportunity is to optimize air scouring flow rate. With relatively stable MLSS concentration and fouling conditions, the required air scouring intensity can be derived from the K_{Target} value (e.g., using Equation 3.8). This requirement can be implemented through various control parameters, such as SAD_p, SAD_m, or direct air flow rate, depending on the plant's control infrastructure. This allows

for dynamic adjustment of blower operation, reducing unnecessary air scouring energy consumption while ensuring hydrodynamic conditions remain favorable.

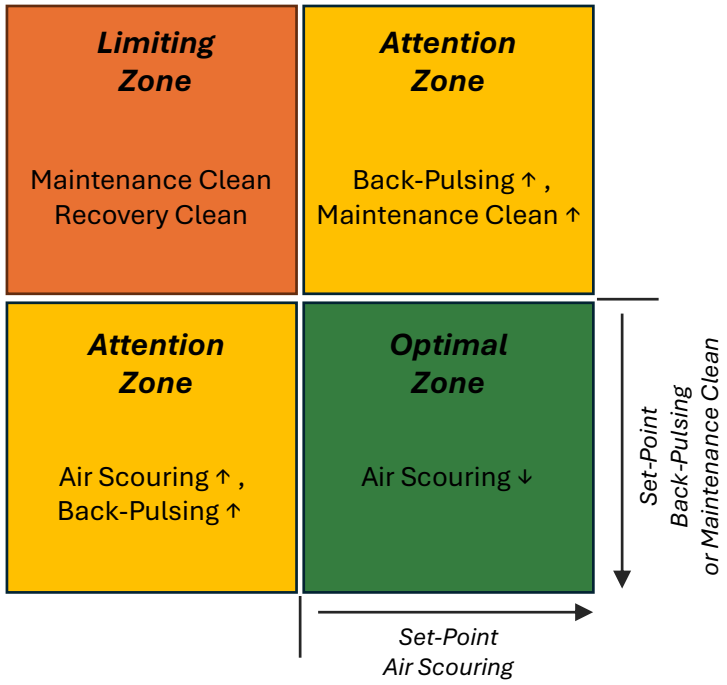


Figure 3.8: A conceptual 2x2 management framework derived from the control matrix. The x-axis represents the hydrodynamic state relative to the K_{Target} threshold (e.g., 2.0×10^{-8} m·s/kg), and the y-axis represents the fouling state relative to the first total resistance (R_T) threshold (e.g., 1.4 kPa/LMH). Each quadrant suggests targeted operational actions to maintain or restore system stability.

In the Attention Zones (Elevated resistance or Unfavorable hydrodynamics), the objective is to apply corrective actions to return the system to the Optimal Zone. The specific actions required depend on the root cause, diagnosed using the supplemental diagnostic plots (Figure 3.7b and c):

1. If the system enters an Attention Zone due to unfavorable hydrodynamics (low K and low resistance), increasing the air scouring rate is the primary response. Operators can also evaluate if the RAS Q rate is sufficient to manage the current solids loading and prevent localized concentration, especially if MLSS is high. More intensive BP can also be applied to minimize reversible fouling accumulation under less favorable hydrodynamic conditions.

2. If the system enters an Attention Zone due to elevated resistance (high resistance, high K), the operator should determine whether R_{BP} or R_{cake} is the main contributor. More intensive BP (e.g., increased BP intensity or frequency) can help alleviate both components. If R_{cake} is elevated, increasing RAS Q can be an effective strategy to enhance the physical removal of the accumulated cake layer. If both are increasing, or if R_{BP} is particularly high, more rigorous MC is necessary to remove the more recalcitrant fouling.

When operating within the Limiting Zone, timely and rigorous MC are crucial to prevent progression into highly irreversible conditions. Since RC requires significant logistical preparation and downtime, performing a proactive and intensive MC at this stage can help prevent severe, potentially permanent loss of permeability, thereby safeguarding overall system performance and capacity.

In summary, the proposed framework serves a dual purpose. Under normal conditions, it acts as a proactive control tool, guiding targeted interventions that maintain the system within the Optimal Zone and reduce resource inputs. Should the system experience an unexpected fouling escalation and enter the Limiting Zone, the framework shifts to a diagnostic resource, providing clear guidelines for aggressive and targeted remedial actions aimed at reducing the resistance components below their first thresholds. This dual capability provides a comprehensive foundation for sustained system stability and efficient fouling management.

3.5 Discussion

This study extends the concept of the single limiting index (K_{Lim}) established in Chapter 2 by developing and validating a dual-metric operating model that considers detailed components of membrane resistance (R_{BP} and R_{cake}). This model provides not just a diagnostic tool, but a

practical decision-making framework for the stable and, most importantly, economical operation of MBR processes, directly addressing the needs of plant operators who must manage current conditions while preparing for future uncertainties.

One of the most important findings is the existence of two distinct, operationally meaningful thresholds based on the hydrodynamic index, K. The first, K_{Target} represents the sustainable capacity of the membranes in the system. Operationally, crossing below K_{Target} marks the transition from stable operation (Phase 1) to accelerated fouling (Phase 2). This point signifies the onset of accumulating recalcitrant fouling, aligning with the literature concept of a "critical flux for irreversibility" (Bacchin et al. 2006). This corresponds to the point where the local foulant concentration exceeds the system's stability limit (e.g., critical concentration or energy barrier), initiating a phase transition from dispersed to condensed matter (Appendix A).

The second, K_{Lim}, defines the absolute maximum capacity, marking the entry into a limiting condition (Phase 3), a state of non-sustainable operation that the system can only handle for short durations, such as during a storm event. This condition is analogous to the limiting flux condition (Astudillo-Castro 2015; Jørgensen et al. 2012), corresponding to the transport limit (Appendix A). While theoretically defined as the point where the concentration of solids at the membrane surface reaches its physical limit (C_{max}), in compressible systems like MBRs, this limit is practically reached when a Critical TMP (Astudillo-Castro 2015; Drews 2010) initiates the physical collapse (compression) of the fouling layer. This triggers a vicious cycle, Cake Compression Feedback. Initial compaction increases specific resistance, necessitating a higher TMP to maintain flux. This elevated TMP, in turn, drives further compression of the existing cake, leads to the penetration of small particles into the cake structure, and intensifies Flux

Redistribution toward less-fouled areas, which accelerates the deposition of new solids. This self-reinforcing cycle can lead to a non-linear fouling acceleration well before C_{max} is achieved.

Under the high-pressure conditions resulting from this feedback cycle (e.g., TMP > 40 kPa), a critical resistance transition known as consolidation occurs (Figure 3.9).

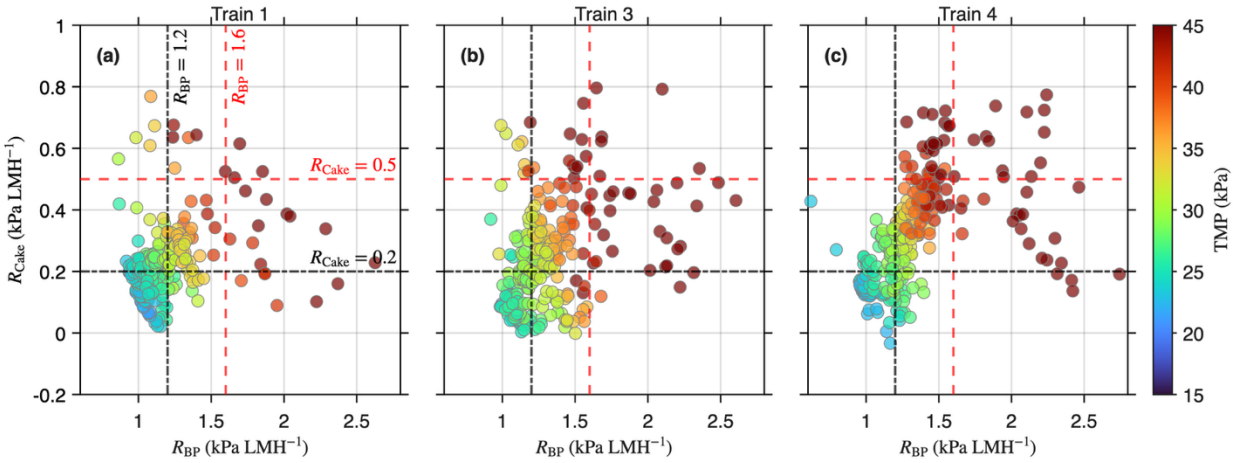


Figure 3.9: Correlation plots of cake resistance (R_{cake}) versus back-pulsing resistance (R_{BP}) for Trains 1, 3, and 4 (panel (a), (b), and (c)). Data points are color-coded by the corresponding Transmembrane Pressure (TMP). The plot illustrates the critical fouling transition phenomenon (consolidation) where, under high TMP (red points), Rcake may decrease as R_{BP} increases

This phenomenon is characterized by an escalation in R_{BP} while R_{cake} stabilizes or decreases. Consolidation is driven by extreme compression (Guo et al. 2012) when the TMP exceeds the cake's compressible yield stress, a threshold pressure required to initiate compression (Díaz et al. 2024; Poorasgari et al. 2015). This causes irreversible structural deformation involving floc deformation and particle rearrangement (Benkahla et al. 1995; Bugge et al. 2012; Lykkegaard Christensen 2006). This process leads to a significant reduction in porosity and the formation of a dense skin layer adjacent to the membrane (Astudillo-Castro 2015). The densified layer exhibits increased cohesive strength (Jørgensen et al. 2012) and resists removal by the standard back-pulsing protocol (Jeison and Van Lier 2006; Van Der Marel et al. 2009). Consequently, this consolidated layer functionally integrates into the persistent, hydraulically irreversible fouling measured by R_{BP}. This transition initiates the severe, escalating cycle, where

exponentially increasing resistance drives higher TMP, which in turn drives further irreversible compression, and is the primary mechanism behind the TMP Jump phenomenon.

This dual-threshold system moves beyond a simple 'normal/failure' dichotomy, providing operators with a multi-stage warning system: K_{Target} acts as an early warning to implement corrective actions, thereby preventing the system from ever reaching the critical failure point, defined by K_{Lim}. This study also provides significant insight into fouling progression mechanisms by identifying two primary pathways and the critical role of fouling maturity. Pathway B (Cake-dominant) is typically initiated by acute stress, such as high solids loading or peak flux events. Here, rapid cake formation (R_{cake}) subsequently penetrates and compacts, contributing to R_{BP}. Pathway A (R_{BP} -initiated) represents the more typical long-term degradation cycle, where a gradual increase in R_{BP} causes Flux Redistribution and Cake Compression Feedback loop. Crucially, the system's response to stress is dictated by its fouling maturity. Membranes with a mature, elevated R_{BP} baseline are hypersensitive and tend to follow Pathway A rapidly, whereas cleaner membranes might initially exhibit Pathway B characteristics under shock loads. Regardless of the initiation pathway, the progression converges as the system approaches K_{Lim}.

The 'Control Matrix' (Figure 3.7) and its simplified 'Action Matrix' (Figure 3.8) translate these findings into practical operational tools. While the framework is broadly applicable, the numerical thresholds for K_{Target}, K_{Lim} and resistance require site-specific calibration. It is important to note that the specific resistance thresholds (kPa/LMH) identified here are contingent on the operating flux range of the studied system (approximately 15-20 LMH). Since phenomena like cake compression are pressure-dependent, systems operating at significantly different nominal fluxes may exhibit different specific resistance thresholds. Therefore, calibration using

historical data or in-situ experiments (e.g., systematically decreasing air scour to identify accelerated TMP rise) is essential. This practical calibration method guides subsequent operations, assuming relatively consistent short-term MLSS characteristics.

While the analysis presented here utilized data from corrugated flat sheet membranes, the underlying principles of the dual-metric framework are expected to be applicable to all types of immersed membranes that use aeration for scouring, including hollow fiber systems. The framework is based on the fundamental balance of forces at the membrane surface (shear vs. convection) and the resulting resistance characteristics. These phenomena are universal to immersed MBRs cleaned with air scouring. Although specific configurations (flat sheet vs. hollow fiber) influence local hydrodynamics, packing density, and aeration efficiency, which would necessitate different empirically determined coefficients (e.g., K_{Lim} and K_{Target}), the core assumptions and the diagnostic approach of characterizing the operating state relative to these thresholds should remain valid across different immersed membrane geometries.

A well-established theoretical relationship, often termed the "2/3 rule," exists between the critical flux (J_c) and the limiting flux (J_{lim}) (Astudillo-Castro 2015; Bacchin 2004; Diez et al. 2014). This principle was first established theoretically for colloidal systems and has since been validated across different models and experimental conditions, with studies consistently finding that the critical threshold is approximately 0.63–0.67 times the limiting value. Notably, a similar relationship was observed for the high-dimensional K value thresholds determined in this study. The ratio between the empirically identified K_{Target} and K_{Lim} was also found to be approximately 0.6. This consistency with fundamental fouling principles provides a practical advantage: once the absolute limiting condition (K_{Lim}) is identified, the sustainable operational target (K_{Target}) can be readily estimated.

Upon determining a reliable K_{Target}, a key application is the implementation of dynamic air scour control. The calibrated K_{Target} serves as a robust setpoint. Operators can use this setpoint to calculate the required air scouring intensity and adjust blower operation accordingly. Furthermore, when hydrodynamic conditions are unfavorable (low K), particularly due to high solids loading, increasing the RAS flow rate is a viable strategy alongside air scour adjustment. Increased RAS flow enhances the upward ML crossflow velocity, which contributes additional homogeneous shear and, critically, accelerates the removal of solids from the membrane tank. It also reduces the MLSS concentration in the membrane tank. This helps mitigate solids thickening near the membrane surface, thereby improving the overall hydrodynamic balance. This strategy is not only more energy-efficient but also more effective. As this study demonstrates, however, once a recalcitrant fouling layer forms, simply increasing air scour may become futile and wasteful, highlighting why the dual-metric approach, monitoring both hydrodynamics stress (K) and system health (resistance), is essential for optimal control.

It is important to acknowledge that the analysis results in this study are based on daily average data. This approach effectively smooths diurnal variability for clear operational assessment, but it inherently incorporates the underlying dynamics: for part of the day, flux can be above the sustainable capacity of the system (i.e, above flux computed from K_{Target}), leading to net accumulation, while for the other part it is below, allowing for some removal. Acknowledging this dynamic strengthens the practical basis of the model.

A novel aspect of this framework is its ability to implicitly account for complex changes in sludge characteristics. Operators are often concerned about unpredictable system responses to variations in sludge properties (e.g., EPS/SMP concentrations), which alter the underlying Force Balance and fouling propensity (Appendix A). The K value model, being phenomenological,

does not explicitly predict these changes as it does not monitor inputs in real-time. Rather than requiring challenging real-time analysis of feed MLSS properties, the model uses direct output measurements like TMP. This allows the calculated resistance and K value to capture the net effect of any changes in sludge properties. This data-driven, diagnostic approach enables operators to respond promptly without the need for advanced laboratory analysis. By monitoring the dual-metric indicators, the resulting system status can be assessed, and appropriate interventions initiated according to the established guidelines (Action Matrix). This enables effective management of the consequences, even if the root cause (sludge change) was unpredictable.

This control framework also minimizes the necessity for RC events. Proactive interventions guided by the control matrix can substantially reduce long-term operational expenditures (OPEX) by lowering costs related to energy, chemicals, labor, and downtime. By preventing severe fouling, the framework also helps preserve membrane longevity, which is inversely correlated with cumulative chemical exposure. Therefore, the dual-metric model provides a powerful tool to shift the MBR operational paradigm from reactive response to proactive prevention and optimization, enhancing the long-term reliability and economic viability of MBR technology.

3.6 Conclusions

One year of data from a highly loaded corrugated sheet submerged MBR facility largely treating municipal wastewater were analyzed to extend previous work quantifying the operating factors limiting the permeate flux through the membranes. The result was the development of a dual-metric approach that assesses the hydrodynamic conditions in the membrane bundle and the condition of the membranes, quantified by the level of fouling (resistance).

1. The hydrodynamics in the membrane bundle are quantified by the calculation of a metric referred to as the K value, developed in the previous research. The numerical value of K for current operating conditions is compared to two benchmarks. K_{Target} represents the onset of hydrodynamic imbalance and accelerated fouling (sustainable capacity). K_{Lim} represents a critical boundary where severe hydrodynamic stress likely induces physical changes in the fouling layer, such as compression (maximum capacity). The condition of the membranes is quantified by the R_T.
2. These two measures define a matrix (Control Matrix) that can be further divided into an optimal zone, two attention zones, and a limiting zone based on the combined values of K and R_T. Statistical analysis confirmed significant differences in the median FR across these regions (Kruskal-Wallis test, $p < 0.001$), validating its use as a diagnostic tool.
3. The optimal zone is defined by a value of K computed using current operating parameters greater than a value referred to as K_{Target} and R_T below a target value. A numerical value of K computed using current operating parameters less than K_{Target} and/or R_T above the target value marks transition to the attention and/or limiting zones where action is required to transition back to the optimal zone to avoid the premature need for recovery cleaning of the membranes.
4. Numerical values of K_{Target} and the limiting R_T can be identified by analysis of historical data and/or by sequential application of membrane operating conditions to create and quantify these limiting conditions.
5. Sustainable long-term operation of the membranes between recovery cleans is achieved by consistent operation in the optimal zone. K is maintained above K_{Target} by providing sufficient air scour flow, avoiding MLSS concentrations greater than needed to meet

overall process requirements, and minimizing R_T. When the numerical value of K based on current operating parameters is greater than K_{Target}, the scour air flow rate can be reduced to reduce energy costs. R_T is managed by maintenance of K greater than K_{Target}, back pulsing, and maintenance cleans.

6. Segmenting R_T into R_{BP} (measuring during back pulsing) and R_{cake} (dynamic cake accumulation; difference between R_T and R_{BP}) facilitates the diagnosis of factors (fouling maturity) leading to R_T increases and identification of actions needed to reduce R_T.
7. Two pathways for the progression of membrane fouling were identified, with the response dictated by fouling maturity. The first pathway (Pathway A) represents typical long-term degradation, where a gradual increase in R_{BP} elevates local fluxes, promoting subsequent R_{cake} formation in a self-reinforcing cycle. The second pathway (Pathway B) is initiated by acute stress (e.g., high solids loading or peak flux), characterized by rapid R_{cake} accumulation. Furthermore, a critical dynamic transition, termed 'consolidation,' was observed under high stress (e.g., critical TMP > 40kPa or near K_{Lim}), R_{cake} physically transforms into R_{BP} as the cake layer compresses or penetration into hydraulically persistent fouling. Understanding these two membrane progression pathways is essential for effective MBR management.

Chapter 4 Integrated Framework for MBR Operation and Generalization

4.1 Introduction

This chapter builds on the results presented in Chapters 2 and 3 to advance the overall objective of this research in minimizing the air scour energy used to operate membranes in the MBR process while maintaining stable performance.

Chapter 2 introduced a data-driven approach for characterizing threshold limiting conditions based on the hydrodynamic balance between foulant deposition and removal. This work developed the K value as a physically interpretable metric that incorporates key operational variables to represent hydrodynamic conditions in a cross-flow filtration system. The identification of critical K value thresholds, such as the limiting K value (K_{Lim}) and the target K value for sustainable operation (K_{Target}), demonstrated the potential for dynamic air scour optimization and energy/resource savings in full-scale MBR systems. However, while the K value indicated proximity to hydrodynamic limitations, it did not fully characterize the state or nature of the accumulated fouling, particularly the persistent fouling components that are unresponsive to adjustments in air scouring.

Acknowledging this limitation, Chapter 3 introduced a dual-metric approach that combines the hydrodynamic index (K) with metrics reflecting the fouling state. Based on extensive analysis of operational data from a full-scale MBR (Plant C), this approach utilized diagnostic resistance components derived from process data, such as BP resistance (R_{BP}) and cake resistance (R_{cake}), to diagnose the fouling status. This analysis revealed critical insights into fouling dynamics, specifically the interplay between hydrodynamics and the resulting system

response, highlighting the importance of maintaining low resistance for preserving high membrane permeability and overall system stability. The development of an empirically derived Control Matrix, using thresholds for the K value and resistance components, provided a framework for categorizing operational conditions and identifying associated fouling rates. This diagnostic framework facilitates the development of an Action Matrix, which provides prescriptive guidance for optimizing system operation and resource inputs (e.g., reducing aeration energy and implementing effective chemical cleaning).

While Chapter 2 established a method for dynamic air scour optimization and Chapter 3 provided tools to diagnose the fouling state, a comprehensive and generalized strategy requires integrating these insights. This chapter presents such an integrated framework, aiming to test its generalizability and adaptability beyond the initial system (Plant C). We will first apply this dual-metric approach to Plant A. Subsequently, we will analyze Plant B, a system with distinct operational characteristics and data limitations. This structured comparison will provide critical insights into which aspects of the framework are universal and which require plant-specific adaptation, ultimately validating a holistic operational philosophy centered on the concept of a system's dynamic "Actual Capacity."

4.2 Method

4.2.1 Data Sources and Processing

This chapter utilizes historical operational datasets from three full-scale MBR systems: Plant A, Plant B, and Plant C. These systems were previously investigated in Chapters 2 and 3. Initial data analysis for Plants A and B (Chapter 2) focused primarily on permeation cycles to identify the K_{Lim}. Chapter 3 involved a more comprehensive investigation of Plant C, including detailed fouling diagnosis by tracking R_{BP} and R_{cake}. This utilized an updated data extraction

algorithm (detailed in Appendix B) compared to the initial work in Chapter 2. To enable a rigorous cross-plant comparison and generalization, this chapter applies the updated data processing framework and analytical approach from Chapter 3, particularly the dual-metric concept, retrospectively to Plants A and B.

Table 4.1 compares the physical configurations and maintenance protocols of the three plants. Plant C has the largest capacity (membrane surface area), followed by Plant A and Plant B. All trains have similar production times (permeation duration), but cleaning protocols differ. Plants A and C utilize relaxation and BP, whereas Plant B only uses relaxation. MCs were conducted using hypochlorite and citric acid following typical protocols. Plant A scheduled one or two MCs per week, while the others scheduled one per week. However, the actual frequency was determined based on the severity of fouling.

Table 4.1: Comparison of Physical Configurations and Cleaning Protocols for Plants A, B, and C

Plant ID	Total Surface Area [m^2]	Permeation Duration [min]	Mechanical Clean	Maintenance Clean
Plant A	23,410	5	Relax/ Back-pulse	One or two per week
Plant B	8,361	5	Relax	One per week
Plant C	52,257	5	Relax/ Back-pulse	One per week

Table 4.2: Detailed Configuration of MBR Plants

Plant ID	Trains	Cassette per Trains	Stacks per Trains	Modules per Stack	Surface Area per Module [m^2]
Plant A	2	6	3	14	46.45
Plant B	1	3	3	25	37.16
Plant C	3	5	3	25	46.45

To facilitate comparison across different systems, specific data standardization procedures and assumptions were applied:

1. Consistent with Chapter 3, this analysis uses the simplified and operationally relevant resistance unit of kPa/LMH instead of the standard hydraulic unit (m^{-1}). This simplifies the interpretation of results from an operational perspective and ensures consistency across all datasets.
2. The simplified resistance and water viscosity values for Plants A and C were temperature-corrected to a standard temperature of 20°C. For Plant B, however, temperature data were unavailable. Consequently, a standard temperature of 20°C was assumed for its data processing and corrections. It must be acknowledged that this assumption introduces uncertainty, as actual temperature variations affect viscosity and thus filtration resistance. However, given that the plant is located in a region with a moderate climate in North America, temperature effects are not expected to significantly alter the primary trends and conclusions drawn from the long-term comparative analysis.
3. FR is quantified by the daily-averaged rate of change in TMP (dTMP/dt), serving as the primary indicator of fouling acceleration. This daily average is computed from the fouling rates of individual permeation cycles.

4.2.2 Fouling State Diagnosis and Correlation Analysis

The fouling state for Plants A and B was diagnosed according to their different operational characteristics and data availability. For Plant A, which includes BP in its operational cycle, the fouling state was diagnosed using the diagnostic resistance components developed in Chapter 3, calculating R_{BP} and R_{cake}. Additionally, statistics on mechanical cleaning and MCs for Plants A and C were used to infer the correlation between each distinct fouling condition and those cleaning practices. Plant B does not utilize BP, making a direct calculation of R_{BP} and R_{cake} impossible. Therefore, the fouling state was assessed indirectly using R_T, inferring its relation to

MC cycles to understand the progression of fouling and the degradation of the system's overall performance.

4.2.3 Evaluation of System Responses and Generalization

The patterns and correlations identified through the integrated analysis were used to revisit and interpret the previously observed performance characteristics of Plants A and B. By first establishing a comparable set of dual metrics for all trains of the three plants, a more rigorous comparison of the underlying fouling mechanisms driving their distinct operational behaviors can be observed. The analysis aims to demonstrate how combining hydrodynamic insights with fouling state diagnosis provides a more nuanced explanation for distinct system responses leading to limiting conditions. The results inform the discussion on the generalizability of the dual-metric concept and support the design of a flexible control strategy.

4.2.4 Visualization of Actual Capacity

To conceptualize and visualize the "Actual Capacity" of each system, the multi-dimensional relationships between permeate flux (J, primary driver), FR, and R_T were quantified. While the true system behavior is a high-dimensional consequence of numerous variables, this analysis approximates this complexity by focusing on the interplay between these three key operational components. For each plant, a 3D surface model describing R_T as a function of J and FR (i.e., $R_T = f(J,FR)$) was generated from the aggregated operational data points. A non-parametric Locally Weighted Scatterplot Smoothing (LOWESS) regression was fitted to the data to create a continuous surface representing the system's resistance response under varying operational conditions. This visualization method allows for a direct comparison of the operational windows and identifies the conditions (i.e., the J and FR combinations) under which R_T remains low (sustainable capacity) or accelerates (limiting conditions).

4.3 Results

4.3.1 Comparison of Historical Operational Conditions

Figure 4.1 presents the historical operational data for Plants A, B, and C, plotting the daily averaged R_T for each train against the plant-wide average permeate flux. These plots provide a high-level overview of the distinct fouling behaviors of each system.

Plant A (Figure 4.1 (a)) demonstrated significant sensitivity to flux dynamics and the impact of historical fouling. Initially operating at a moderate flux (~10 LMH), the trains exhibited divergent resistance levels following an initial RC on Train 2 in August 2022; Train 1 subsequently maintained a persistently more fouled condition (higher R_T). Following RCs on both trains in March 2023, a high-flux event in April 2023 triggered a rapid increase in R_T across both trains, necessitating frequent MCs. Notably, when the flux was later reduced, Train 2 recovered rapidly while Train 1 remained elevated. This divergence indicates that Train 1 had developed a more persistent fouling condition, reducing its resilience to subsequent stress. This highlights how underlying fouling maturity dictates a system's capacity, aligning with findings in Chapter 3.

Plant B (Figure 4.1 (b)) exhibited chronic instability characterized by frequent, sharp fluctuations in R_T, even under stable, low-flux conditions (< 10 LMH). While MCs were effective at temporarily reducing resistance, the baseline R_T showed a gradual upward trend over the operational period (e.g., April 2023 baseline higher than October 2022). This progressive accumulation of irreversible fouling intensified the magnitude of R_T fluctuations later in the study. The absence of BP in Plant B likely contributed to this accelerated development of persistent fouling.

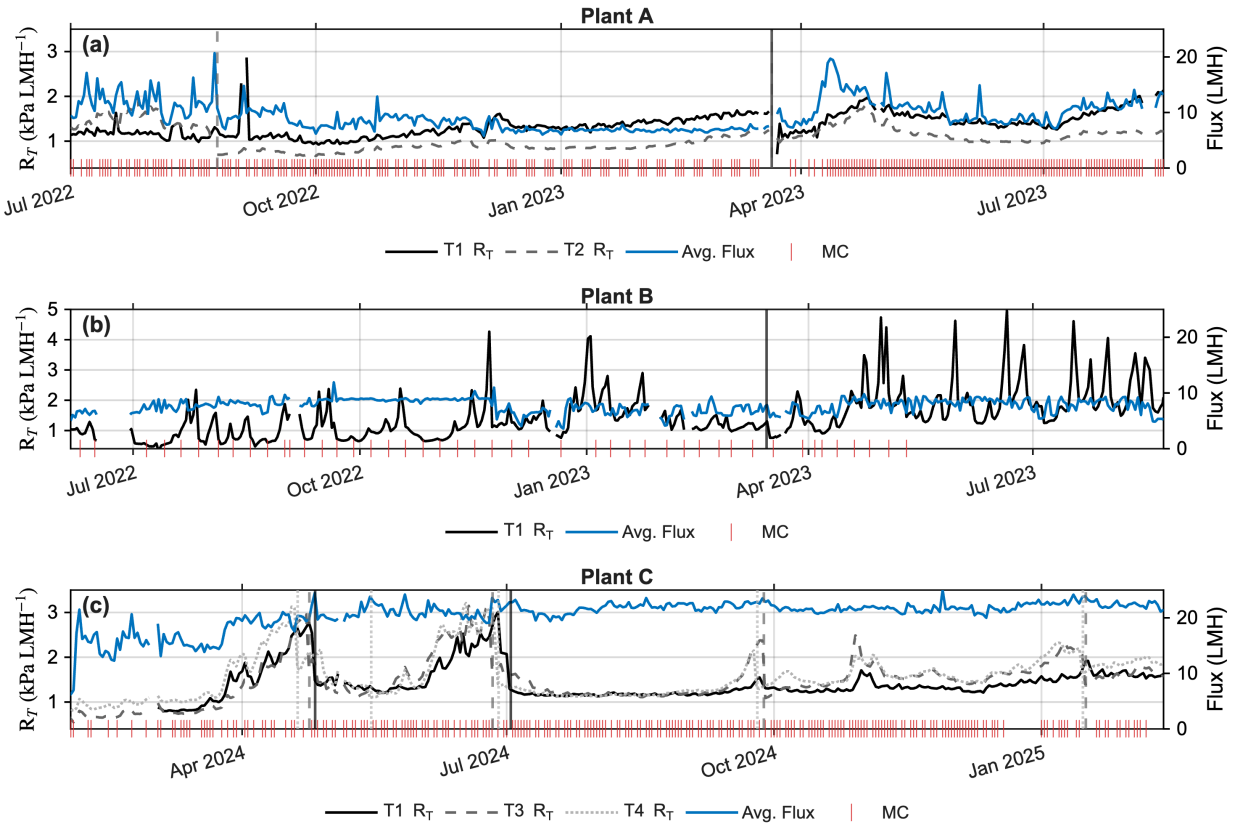


Figure 4.1: Daily averaged total resistance (R_T) and permeate flux for Plant A (panel (a)), Plant B (panel (b)), and Plant C (panel (c)). Black solid and dashed lines represent individual trains. The light blue line indicates the plant-wide average flux. Red vertical markers denote maintenance cleaning events.

Plant C (Figure 4.1 (c)) operated under the highest stress, with fluxes consistently exceeding 20 LMH. The plant began with clean membranes, but a rapid increase in R_T occurred within the first two months, a period characterized by high MLSS concentrations and the absence of BP (Figures 3.1 and 3.2). Although BP was initiated in early April 2024 and RCs, the baseline R_T did not return to its initial level. This indicates that rapid irreversible fouling occurred during the initial upset operational phase. Following a period of stable operations in mid period, the system again showed recurring R_T fluctuations, particularly in Trains 3 and 4. Similar to Plant B, this pattern suggests that repeated fouling events contributed to a rising baseline of irreversible fouling, which in turn made the system more sensitive to operational changes. This sensitivity was evident in January 2025, when an increase in the average daily flux from 20 LMH to 23

LMH triggered a disproportionately large increase in R_T. It is worth noting that the daily average flux masks the peak flux, which often approached 30 LMH during the later period.

The key operational statistics, summarized in Table 4.3, quantify these historical trends. Plant C clearly operated with the highest average TMP (24.7 ± 8.2 kPa) and flux (20.2 ± 2.4 LMH), with a consistently high mean R_T and low variance. In contrast, Plants A and B had similar, lower average TMP and flux, while Plant B had a higher mean R_T with larger variation. The high standard deviation of TMP in Plant B (± 6.5 kPa) compared to its relatively steady flux (7.7 ± 1.3 LMH) reflects the frequent, sharp resistance spikes observed in Figure 4.1. Regarding aeration (i.e., shear intensity), Plant C used the highest specific aeration demand per membrane area (SAD_m, 0.21 $m^3/m^2/hr$). However, its specific aeration demand per permeate volume (SAD_p) was the lowest among the three plants. This combination suggests that despite the high absolute air volume, the intense permeation drag at high flux created hydrodynamically unfavorable conditions, overwhelming the effects of air scour. MLSS concentrations were within typical ranges for MBRs, though Plant C's higher standard deviation reflects the instability during its initial operation, as detailed in Chapter 3. The RAS to permeate ratio (RAS Q) was maintained near the recommended value of 5. This is critical for mitigating cake layer thickening, especially under high flux conditions, due to ML thickening effects along the membrane modules.

Table 4.3: Key operational statistics for each train in Plant A, B, and C. Values are presented as mean ± standard deviation.

Plant ID	TMP (kPa)	Flux (LMH)	R_T (kPa/LMH)	SAD_m ($m^3/m^2/hr$)	SAD_p (-)	MLSS (g/l)	RAS Q [-]
Plant A T1	12.1 ± 4.6	8.7 ± 2.4	1.35 ± 0.22	0.13 ± 0.01	15.9 ± 3.3	5.8 ± 0.7	6.3 ± 0.7
Plant A T2	10.7 ± 4.7	9.8 ± 2.1	1.05 ± 0.23	0.13 ± 0.01	13.9 ± 2.0	5.8 ± 0.7	6.1 ± 0.6
Plant B T1	11.0 ± 5.2	7.7 ± 1.1	1.43 ± 0.61	0.15 ± 0.01	19.7 ± 3.0	6.6 ± 0.4	5.9 ± 0.5

Plant C T1	24.2 ± 6.9	20.9 ± 1.5	1.41 ± 0.31	0.21 ± 0.02	10.2 ± 0.6	7.3 ± 1.4	4.8 ± 0.3
Plant C T3	25.8 ± 8.2	21.3 ± 2.5	1.46 ± 0.43	0.21 ± 0.03	9.8 ± 0.7	7.2 ± 1.4	4.6 ± 0.3
Plant C T4	26.5 ± 8.3	20.4 ± 2.2	1.55 ± 0.43	0.21 ± 0.03	10.5 ± 1.0	7.2 ± 1.4	4.9 ± 0.5

In summary, the comparative analysis of the three plants reveals distinct MBR fouling behaviors. Plant A illustrates how dynamic flux drives fouling and, more critically, how a system's underlying fouling history can cause divergent performance between trains under identical operational stress. In contrast, Plant B demonstrates how the uncontrolled progression of fouling creates intrinsic instability even under a consistent permeate flux, proving that internal degradation alone (e.g., fouling progression) can drive a system toward limiting conditions. Plant C presents the most complex, hybrid scenario, simultaneously subjected to both high-flux operational stress and the development of internal fouling. The advanced state of its irreversible fouling creates persistent instability with frequent resistance fluctuations even during consistent flux periods, rendering the system critically sensitive to any further operational changes. These distinct behaviors underscore the necessity of monitoring not only operational conditions but also the underlying fouling state to maintain stable membrane performance.

4.3.2 Comparison of Different Pathways to Limiting Conditions: Plants A and C

The preceding overview identified distinct operational behaviors across the three facilities. Plants A and C, both equipped with BP, allow for a detailed diagnosis of fouling components. This section examines the dynamics of the FR in these two plants, specifically focusing on its relationship with the primary driving force, TMP, and how this relationship is modulated by R_T and flux. This analysis aims to elucidate the mechanisms underlying their different pathways to limiting conditions.

Figure 4.2 illustrates these relationships. The top panels (panels (a) and (b)), plotting FR vs. TMP, show that FR generally increases with TMP in both plants. However, the data reveals a distinct diagonal stratification when colored by R_T. This pattern indicates that the system's response is governed by the interaction between the fouling state (R_T) and the driving force (TMP). For a constant R_T, FR increases linearly with TMP. Furthermore, at a fixed TMP, a lower R_T corresponds to a higher FR. This occurs because lower R_T implies a higher permeate flux ($J = TMP/R_T$) at the same pressure, resulting in increased convective drag. This interaction reveals the system's "Actual Capacity," the sustainable treatment rate at a given state. The observed stratification is empirical evidence that this capacity is dynamic, not fixed.

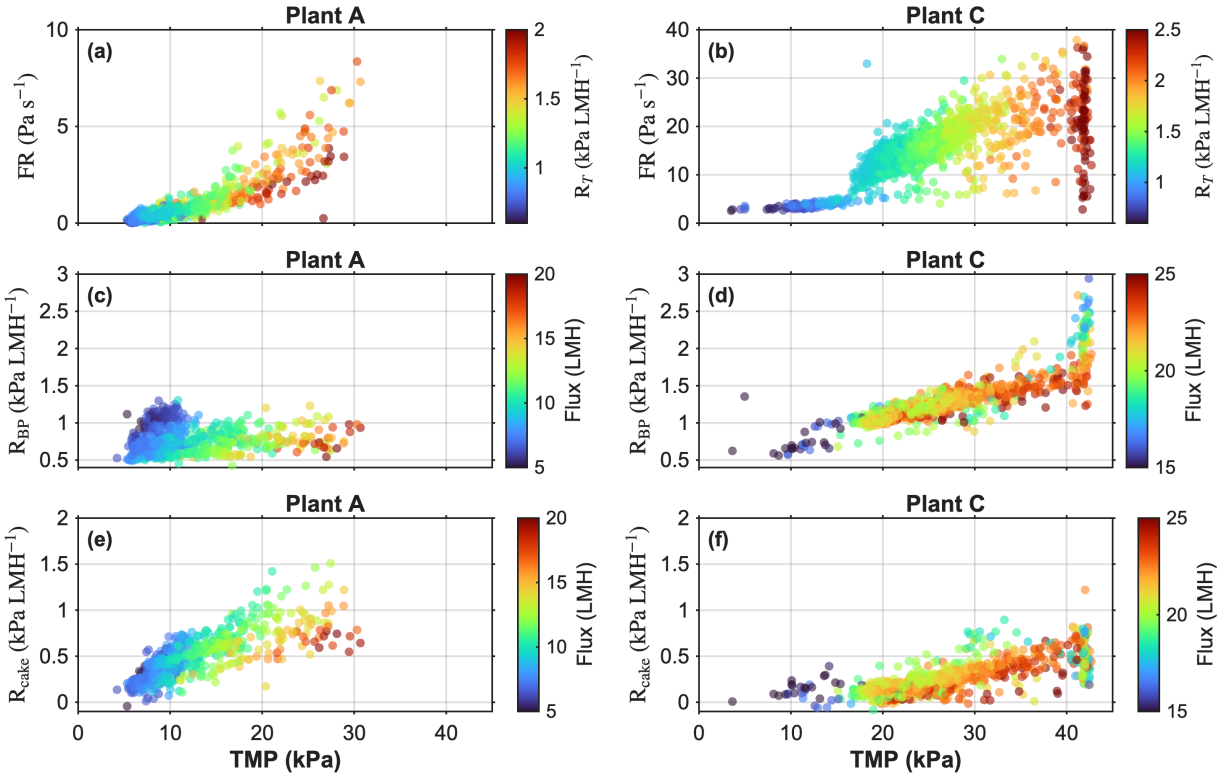


Figure 4.2: Fouling characteristics for Plant A (left column) and Plant C (right column) as a function of Transmembrane Pressure (TMP). The top row (panels (a) and (b)) shows fouling rate (FR) vs. TMP, color-coded by total resistance (R_T). The middle row (panels (c) and (d)) shows back-pulse resistance (R_{BP}) vs. TMP, and the bottom row (panels (e) and (f)) shows cake resistance (R_{cake}) vs. TMP. Data points in the middle and bottom rows are color-coded by permeate flux.

The middle and bottom panels of Figure 4.2 (c) to (f) show decomposed R_T, revealing the mechanisms driving the distinct pathways observed in Plants A and C. In Plant C (panels (d) and (f)), R_{BP} increases with TMP and accelerates sharply near 40 kPa. This behavior corresponds to the consolidation mechanism identified in Chapter 3, where high pressure drives the physical transformation of the fouling layer into a persistent state. R_{cake} in Plant C remains low until TMP exceeds approximately 25 kPa, after which it begins to rise, contributing to the reinforcing cycle (Pathway A). Plant A (panels (c) and (e)) exhibits a contrasting mechanism. R_{BP} remains low and largely independent of TMP. Instead, R_{cake} is the dominant resistance component and shows a clear linear increase with TMP. This indicates that the progression toward limiting conditions in Plant A is governed primarily by cake development (Pathway B).

This analysis demonstrates that the dominant factors leading to limiting conditions differed fundamentally between the two plants. In Plant C, the process was driven by the consolidation of persistent fouling (R_{BP}), while in Plant A, it was driven by dynamic cake accumulation (R_{cake}). This decomposition of fouling behavior, foundational to the dual-metric framework, is essential for identifying targeted mitigation strategies.

4.3.3 Investigating Fouling Dynamics in Plant A

This section investigates the fouling progression trajectory in Plant A using the diagnostic framework established in Chapter 3. This approach allows for an examination of how fouling evolves as a consequence of dynamic operational conditions and how these dynamics affect fouling acceleration (FR). The fouling trajectory for Plant A's trains, plotted as R_{cake} versus R_{BP}, is presented in Figure 4.3. This figure illustrates the temporal evolution of fouling (color-coded by date) against FR contours in the background (darker lines indicate higher FR). It includes two

iso-resistance thresholds (1.4 kPa/LMH and 2.1 kPa/LMH) determined from Plant C (Chapter 3) as benchmarks. Lastly, RC events are highlighted with red circles.

For Train 1 (panel (a)), the initial fouling state (cooler-colored markers, representing dates from July 2022) was characterized by a relatively lower R_T (R_{BP} + R_{cake}) compared to Train 2, remaining below the first iso-resistance threshold. During the low-flux period from approximately October 2022 to March 2023, R_{BP} of Train 1 gradually increased, exceeding 1.0 kPa/LMH. This rise in R_{BP} caused the R_T to exceed the first iso-resistance threshold. However, R_{cake} changes remained negligibly low, and there was no significant increase in FR during this period (sparse and dim-colored contours). This suggests that despite the elevated R_T driven by R_{BP}, the system's Actual Capacity was still sufficient to handle the prevailing low flux conditions. Then, the first RC was conducted, dramatically reducing resistance, especially for R_{cake}. Subsequently, a sharp increase in flux from April 2023 (annotated as "1st High Flux" in the figure) triggered a rapid rise in R_{cake}. Although subsequent flux reduction and rigorous MCs around July 2023 led to a slight decrease in both R_{BP} and R_{cake} (though the R_T in Train 1 remained higher than that of Train 2 at that point), R_{cake} once more rose sharply when the flux increased again in a later period ("2nd High Flux"; in July 2023, but lower flux than the first), showing a higher FR. This behavior suggests less favorable hydrodynamic conditions later due to the further elevated fouling state, indicating a reduced Actual Capacity of the system to handle the imposed flux at that time.

Train 2 (panel (b)) initially presented with a higher R_{cake} condition (earlier blue markers) before an RC shifted its fouling state towards lower R_{BP} and R_{cake} values (bottom-left red circle). Subsequently, during the low-flux period, R_{BP} in Train 2 also gradually increased, but not to the same extent as in Train 1, remaining below 1.0 kPa/LMH by the end of this period. The "1st High

Flux" event similarly caused a rapid increase in R_{cake} in Train 2, pushing its operational state across the first iso-resistance threshold line. This clearly indicated that the peak flux exceeded the system's sustainable handling capacity (i.e., Actual Capacity). Interestingly, during the "2nd High Flux" period, Train 2 did not exhibit a similar rapid escalation in R_{cake}. Instead, its R_{BP} decreased, likely attributable to more effective MCs than Train 1. Given that the daily averaged flux during this latter period was around 15 LMH, compared to peaks near 20 LMH during the first high-flux event, Train 2 appeared capable of managing the 15 LMH flux but was evidently challenged by the 20 LMH peak, thus exhibiting a different response in each high-flux period.

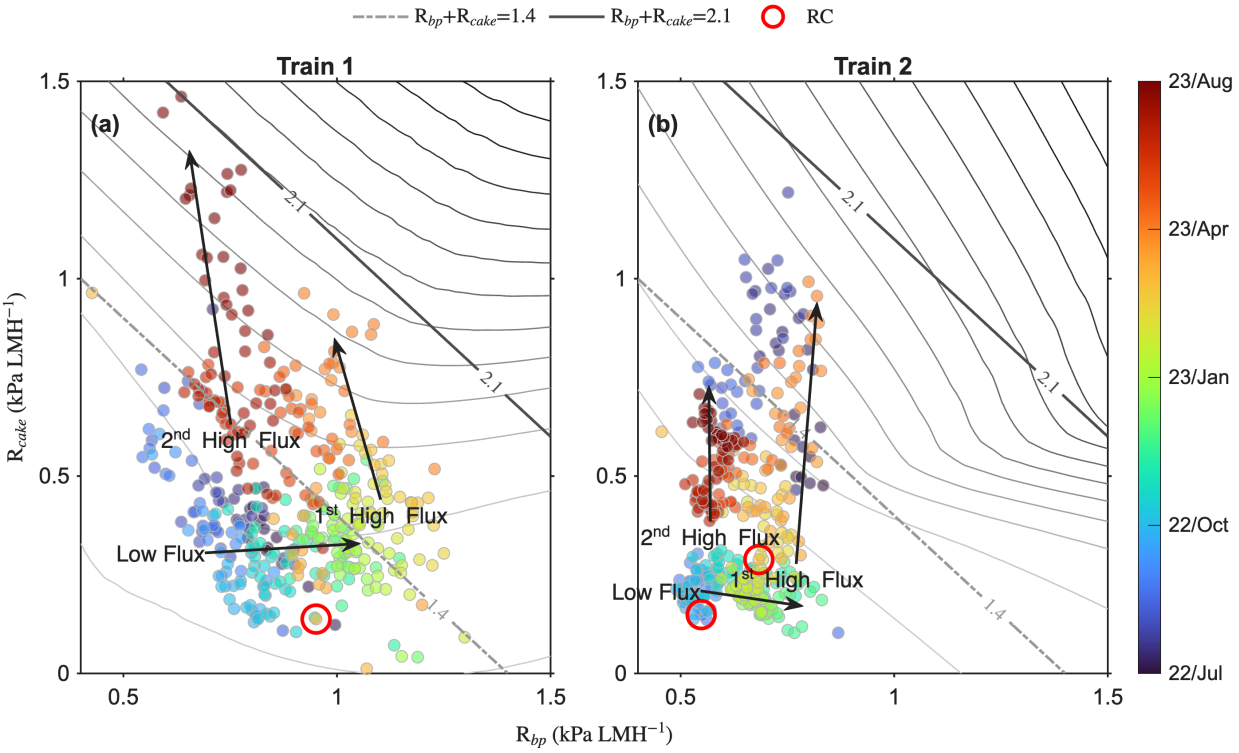


Figure 4.3: Fouling trajectory analysis plotting back-pulse resistance (R_{BP}, x-axis) against cake resistance (R_{cake}, y-axis) for Train 1 (panel (a)) and Train 2 (panel (b)) of Plant A. Data points are color-coded by date to illustrate temporal evolution. The background contour lines indicate fouling rate (FR), with darker gray lines representing higher FR values. Red circles highlight the data point immediately following a recovery clean (RC). The diagonal lines represent iso-resistance thresholds ($R_{BP}+R_{cake}$ = 1.4 and 2.1 kPa/LMH) derived from Plant C (Chapter 3) for benchmarking.

The comparison between the two trains underscores the impact of the underlying fouling maturity on system resilience. Train 1, burdened by persistently higher R_T, struggled to handle

both high-flux conditions. This implies that its compromised fouling state had reduced its Actual Capacity far more significantly than that of Train 2, rendering it incapable of managing even a 15 LMH flux without substantial cake accumulation. These observations highlight the importance of maintaining low baseline fouling resistances (both R_{BP} and R_{cake}). Furthermore, they clearly illustrate how an elevated, pre-existing fouling state sensitizes the MBR system to external stimuli, such as flux increases, leading to divergent operational responses and compromised stability.

4.3.4 Insights into Controlling Intact Fouling

Plant A was characterized by dominant cake fouling with well-controlled R_{BP}. In contrast, in Plant C, R_{BP} primarily governed the gradual fouling process and eventually triggered an increase in both resistance components. These distinct fouling pathways can be attributed to differences in flux dynamics and operational conditions. An analysis of the BP and MC practices provides insight into how these strategies influenced the observed differences.

Figure 4.4 summarizes the cleaning characteristics for Plant A and Plant C. Panel (a) illustrates the BP interval. Plant A utilized a median interval of approximately 34 minutes (corresponding to 1 BP cycle per ~6 permeate cycles). In contrast, Plant C employed a shorter median interval of 24.5 minutes (1 BP per 5 permeate cycles), indicating more frequent BP. Moreover, Plant A exhibited a tighter distribution around its median, with less variation towards shorter intervals. Plant C not only had a shorter median interval but also exhibited instances of much more frequent BP, with intervals down to 5 minutes (a 1:1 permeate/BP cycle), especially during high-stress conditions.

The middle panel (b) in Figure 4.4 displays the median BP flux intensity, indicating that more intense BP was generally applied in Plant C. While both plants varied the BP flux intensity

depending on fouling status, Plant A had a median value of approximately 4.9 LMH, while Plant C's was 6.1 LMH, roughly 27% higher. This combination of higher frequency and intensity in Plant C constitutes a more aggressive BP strategy. This approach likely explains the observation from Figure 4.2 that its R_{cake} was kept significantly lower than its R_{BP}, suggesting it was effectively controlled by this robust BP protocol.

Conversely, the approach to longer-term cleaning differed noticeably. Panel (c) in Figure 4.4, showing the interval between MC events, reveals that more frequent MC was performed in Plant A, with a median interval of approximately 1 day, compared to Plant C's 3 days. It is noted that, for Plant A, this near-daily MC was implemented primarily in the later operational period, whereas Plant C maintained a more regular MC schedule throughout its operation.

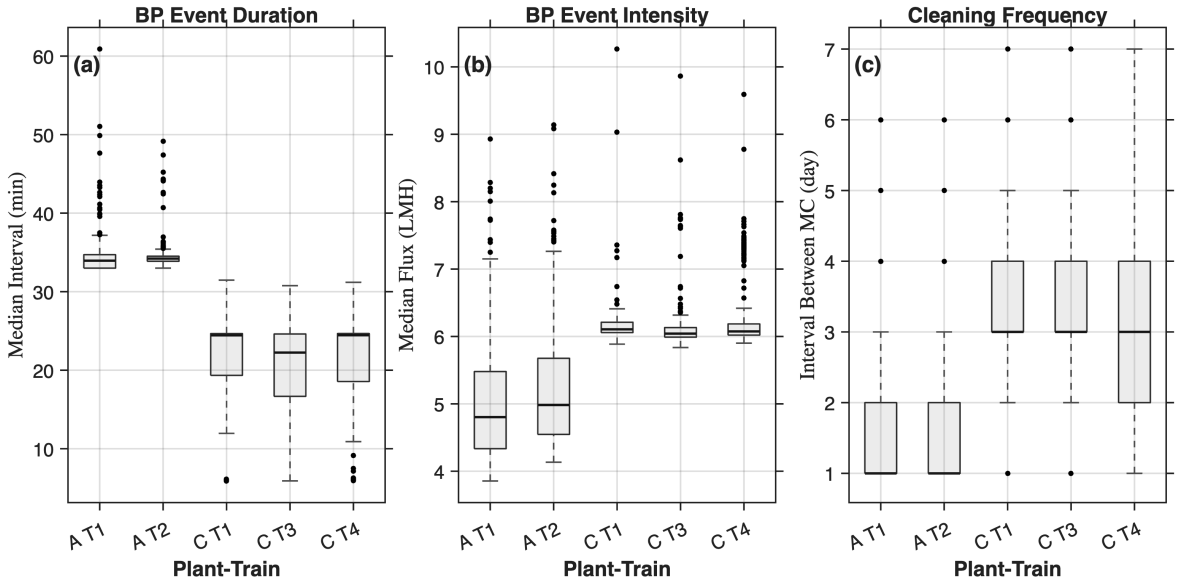


Figure 4.4: Box plot comparison of cleaning strategies implemented in Plant A (A T1, A T2) and Plant C (C T1, C T3, C T4). The panels show distributions for (panel (a)) the interval between Back-Pulsing (BP) events, (panel (b)) the intensity of BP events measured as flux, and (panel (c)) the interval between Maintenance Cleaning (MC) events. The central mark in each box indicates the median, the box edges represent the 25th and 75th percentiles, the whiskers extend to the most extreme data points not considered outliers, and outliers are plotted individually as dot marks.

Both plants operated at different mean flux levels, a key factor known to influence irreversible fouling (Chang et al. 2002; Ding et al. 2016; Miller et al. 2014). Therefore, caution is

warranted when generalizing these correlations. Nevertheless, these observations guide operational strategies based on the fouling pathway, suggesting an aggressive BP strategy (frequency and intensity) is critical for mitigating excessive R_{cake} buildup. Routine and sufficient MC is primarily effective for controlling the gradual increase of R_{BP}. However, once the system enters a limiting condition and develops highly intact fouling, which cannot be effectively removed by either standard BP or MC, both methods become less effective. This highlights the critical need for proactive, condition-based cleaning strategies that are dynamically adjusted by monitoring fouling progression, rather than relying on fixed schedules, to maintain long-term stable performance.

4.3.5 Fouling Dynamics in Plant B: An Indirect Assessment

As Plant B does not utilize BP, a direct diagnosis of the fouling state using the diagnostic framework of resistance decomposition is not possible. Therefore, one must rely on R_T and indirect evidence to infer the fouling conditions. Nevertheless, the core principle observed in Plants A and C, that elevated R_T eventually triggers a rapid increase in fouling rate once it crosses a critical threshold level, can still be applied conceptually. By monitoring changes in resistance level, it is possible to estimate the fouling progression (i.e., pathway) and determine appropriate actions.

Plant B operated under a consistent flux with regular MCs (once per week) but without BP. It frequently exhibited sharp increases in resistance, which were effectively reduced after MC events. This pattern suggests a recurring buildup of fouling that, while removable by MC, progressively reduced the system's Actual Capacity between cleanings. It can be hypothesized that, even at a relatively low flux of around 10 LMH, the accumulation of high-specific-

resistance fouling lowered the system's sustainable flux limit, leading to accelerated fouling development and eventual limiting conditions.

Figure 4.5 provides data to support this hypothesis. On Day 1 after MC, the FR shows a low and stable level onward to the fourth day after the last cleaning event. Then, FR begins to trend upwards and fluctuate after Day 5, with a more pronounced increase by Day 6, followed by MCs. This trend suggests that the system's Actual Capacity degrades as fouling accumulates in the days following a cleaning under constant low flux, making it more susceptible to accelerated fouling. This underscores the importance of proper fouling control to prevent the gradual degradation of system performance, even under seemingly stable operational conditions.

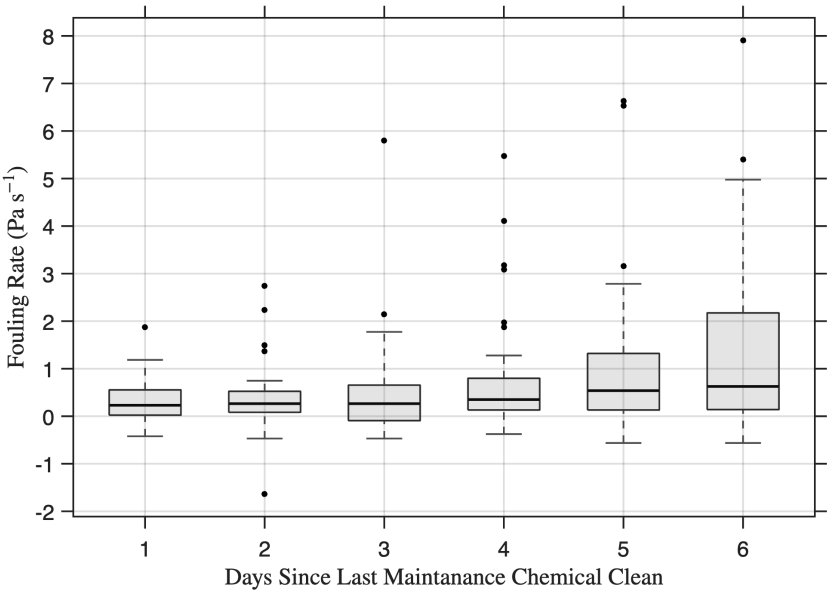


Figure 4.5: Box plot distribution of the daily fouling rate (FR) in Plant B as a function of the number of days since the last maintenance cleaning (MC) event. The central mark in each box indicates the median, the box edges represent the 25th and 75th percentiles, the whiskers extend to the most extreme data points not considered outliers, and outliers are plotted individually as dot marks.

4.3.6 Generalization of Control Matrix

For generalized operational control, the detailed resistance analysis (R_{BP} and R_{cake}) can be simplified into a direct framework using the K value and R_T. This approach relies on daily averaged data to represent the overall state of "intact" fouling by smoothing short-term

fluctuations. This section evaluates the generalization of this dual-metric control map across all three plants. Figure 4.6 presents the generalized control map, plotting the daily averaged K value against R_T for each train, with data points color-coded by normalized FR to convey the experienced stress.

This utilizes the established hydrodynamic thresholds (K_{Lim} and K_{Target}) and iso-resistance thresholds. Recognizing that K_{Target}, the point where the hydrodynamic balance becomes unfavorable, is influenced by site-specific factors such as local rheology and hydrodynamics (shear, drag, and interaction), the K_{Target} values for Plants A and B were recalibrated to 3.0×10^{-8} m·s/kg to better reflect the onset of unfavorable hydrodynamic balance at these sites. The map is divided into nine sections categorizing operational risk (Optimal, Attention, and Limiting Zones).

A key finding is the consistent transition to higher FR around these common threshold lines across all plants, despite their vastly different operational conditions and fouling pathways. This consistency demonstrates that the dual-metric Control Matrix robustly estimates a system's proximity to a fouling transition point, regardless of the specific trigger (e.g., high peak flux, high solid loading, or fouling-induced Flux Redistribution). The categorization is effective: low FR is predominantly observed in the Optimal Zone (green); FR increases upon entering the Attention Zone; and the highest FR and resistance levels are confined to the Limiting Zones.

A detailed examination of the data distribution reveals how the framework captures their distinct behaviors. In Plant A (panels (a) and (b)), data points appear in the upper Attention Zone (high R_T, high K) during the dry period. The FR increase was modest, suggesting the Actual Capacity remained above demand despite the fouled condition. Both trains exhibit high FR in the left Attention Zone (low K), characterized by hydrodynamic stress, with the highest FR observed

near K_{Lim}. Plant B (panel (c)) shows a trajectory of gradually increasing resistance and decreasing K value, leading to a gradual FR increase. This culminates in a tipping point where resistance and FR spike rapidly. Given the consistent flux, this indicates the Actual Capacity was reached due to the accumulated fouling condition.

Plant C (Panels (d), (e), and (f)) represents the most stressed scenario, operating consistently at the edge of stability due to high flux demand. Characterized by elevated R_T and K values near K_{Target}, the system had minimum operational buffer. The absence of data in the upper Attention Zone implies a rapid transition to the Limiting Zone once resistance elevates under the high-flux conditions.

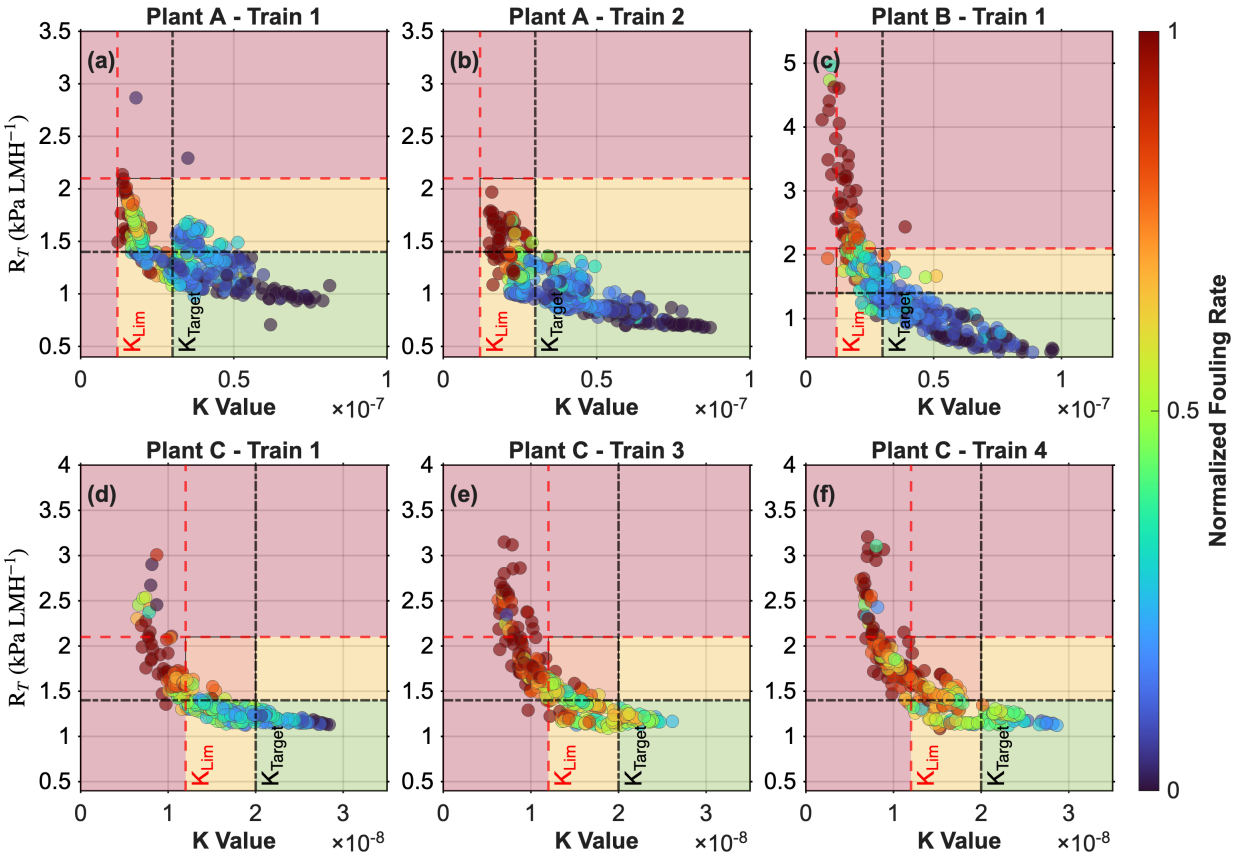


Figure 4.6: Generalized control map plotting daily averaged K value versus total resistance (R_T) for Plant A (panels (a), (b)), Plant B (panel (c)), and Plant C (panels (d), (e), and (f)). Data points are color-coded by the magnitude of the normalized fouling rate (FR). Vertical lines indicate the target K value (K_{Target}, black dash-dot) and the limiting K value (K_{Lim}, red dashed). Horizontal lines indicate the empirically determined iso-resistance thresholds: the first (black dash-dot) and the second (red dashed).

The behavior across all plants demonstrates that their distinct fouling pathways can be consistently interpreted and visualized through the dual-metric framework. K_{Target} effectively serves as a leading indicator of hydrodynamic instability. Furthermore, the sharp acceleration in FR as the system approaches K_{Lim} or resistance limits points to a common underlying failure mechanism, the physical transitions of compression and consolidation in the fouling layer.

While interpreting the precise cause of fouling solely from the visualization profile can be challenging, the pattern and location of the data points on the Control Matrix provide powerful diagnostic information. When combined with the operational context, such as recent changes in flux, MLSS levels, or cleaning history, this framework allows for a reasonable estimation of the current fouling condition and the system's stability. Therefore, the dual-metric Control Matrix serves as a robust and generalizable tool, providing reliable indicators to guide proactive control actions and significantly aid in the sustainable operation of full-scale MBR systems.

4.4 Discussion

4.4.1 The Unifying Concept of Actual Capacity

The comprehensive analysis across three distinct MBR plants validates the dual-metric framework (K value and Resistance indicators) as a robust, generalizable tool for diagnosing diverse fouling pathways. This synthesis culminates in a holistic operational philosophy centered on the concept of "Actual Capacity."

MBR operation is fundamentally a balance between permeate demand and the system's sustainable ability to meet it. Actual Capacity is defined as the maximum flux a system can handle at its current fouling state without triggering an imbalance between foulant deposition and removal (i.e., without exceeding the stability limit, K_{Target}). While a system has a theoretical

Design Capacity, the Actual Capacity is the true operational limit. It is not a fixed value but a dynamic property that degrades as fouling progresses.

The dynamic nature of Actual Capacity stems from the reality that the fouling threshold is not a single, fixed point but a high-dimensional 'spectrum' or 'transition zone' that constantly shifts. This complexity arises from the non-linear interactions of numerous variables. For instance, the system's state is continuously altered by biological changes, such as fluctuating MLSS concentrations, sludge rheology, and the characteristics of microbial products like EPS and SMP (Díaz et al. 2016; Le-Clech et al. 2006; Meng et al. 2007; Yang et al. 2009). Simultaneously, chemical conditions like pH and ionic strength modify the interfacial forces governing foulant adhesion (Bacchin et al. 2006; Ehsani et al. 2021; Xu et al. 2020; Ying et al. 2010), while physical parameters such as temperature variations impact fluid viscosity and overall hydrodynamics (Iorhemen et al. 2016; Liu et al. 2003; Pradhan et al. 2022; Wang and Gao 2021). It is the complex interplay of these interconnected factors that defines the system's ever-changing operational limit.

Because it remains impractical to monitor this entire multi-dimensional state in real-time, the operational state has historically been abstracted into the most critical parameter: flux. Flux directly represents productivity and is the primary driver of convective transport. This focus led to the concept of a fixed "critical flux." However, this model requires reframing. The critical flux must be understood not as an absolute constant, but as a dynamic, localized threshold evolving across time and space within the membrane bundle.

Figure 4.7 conceptually illustrates this dynamic. While Actual Capacity is a multi-dimensional concept, this illustration simplifies the dynamics by focusing on flux and the fouling condition. The blue dashed line represents the expected maximum capacity (Design Capacity),

which is a fixed value based on clean membrane conditions. However, as fouling progresses, the Actual Capacity (red line) degrades over time. When the operational flux demand (black line) exceeds this declining Actual Capacity (shaded areas), fouling accelerates. This dynamic has two critical consequences. First, peak fluxes cause more severe fouling than initially expected. Second, and more importantly, fouling accelerates even at fluxes that were previously sustainable. This clarifies the long-observed phenomenon where rapid fouling still occurs even when the operating flux is theoretically below the pre-defined critical flux level. This occurs because the true fouling threshold dynamically degrades, or because spatial heterogeneity causes localized fluxes to exceed the threshold even if the average flux does not (Cho and Fane 2002; Ognier et al. 2004). Therefore, the critical flux concept must be dynamically integrated with the Actual Capacity of the membrane system.

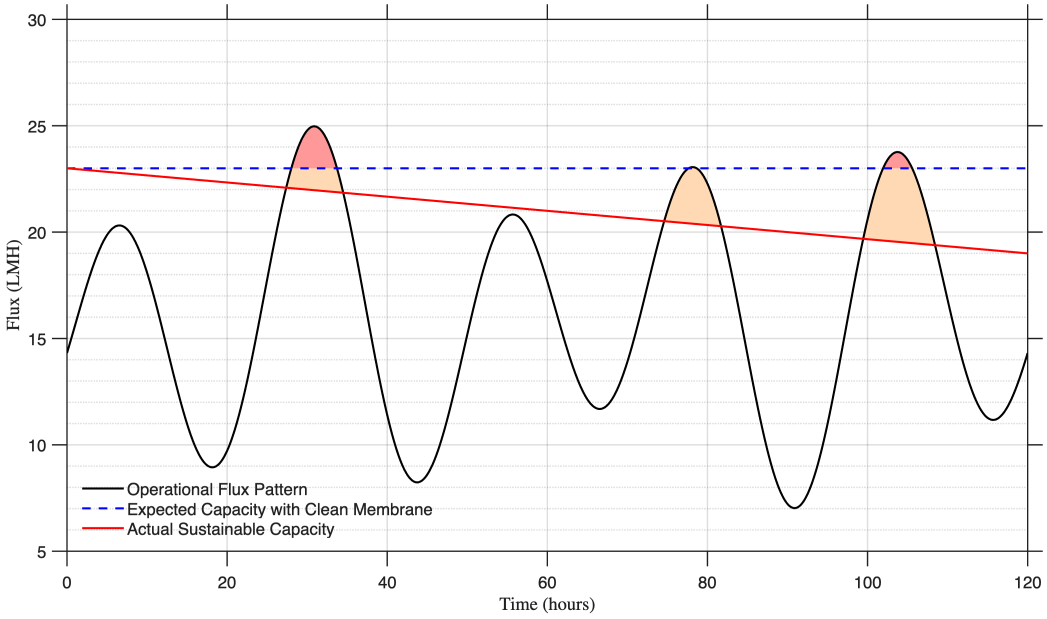


Figure 4.7: Conceptual illustration of a system's declining 'Actual Sustainable Capacity' (red line) in response to fouling progression, shown against a typical diurnal 'Operational Flux' pattern (black line) and the fixed maximum design capacity (blue dashed line). The shaded orange areas represent periods where the operational demand exceeds the system's sustainable capacity, leading to accelerated fouling.

This concept explains the diverse behaviors observed across the three plants. Plant A experienced a transition when an external stressor (high-flux event) surpassed its existing Actual

Capacity. Plant B operated at a low flux, but gradual fouling eroded its Actual Capacity until even that low flux became critical. Plant C demonstrated a highly stressed system where high flux and high solid loading continuously challenged a rapidly degrading capacity. This dynamic creates a vicious cycle: accelerated fouling further reduces Actual Capacity, increasing sensitivity to existing flux. Effective MBR management thus requires a shift from predicting a fixed threshold to a 'sensing and responding' paradigm. The dual-metric framework provides the tools to "sense" the dynamic Actual Capacity, allowing operators to adaptively adjust controls and maintain the operational flux below the real-time sustainable limit.

4.4.2 Visualizing the Actual Capacity with Operational Data

The theoretical concept of Actual Capacity is directly substantiated by operational data. Figure 4.8 provides this data-driven evidence by plotting the FR against the permeate flux for each plant, with R_T shown as color contours.

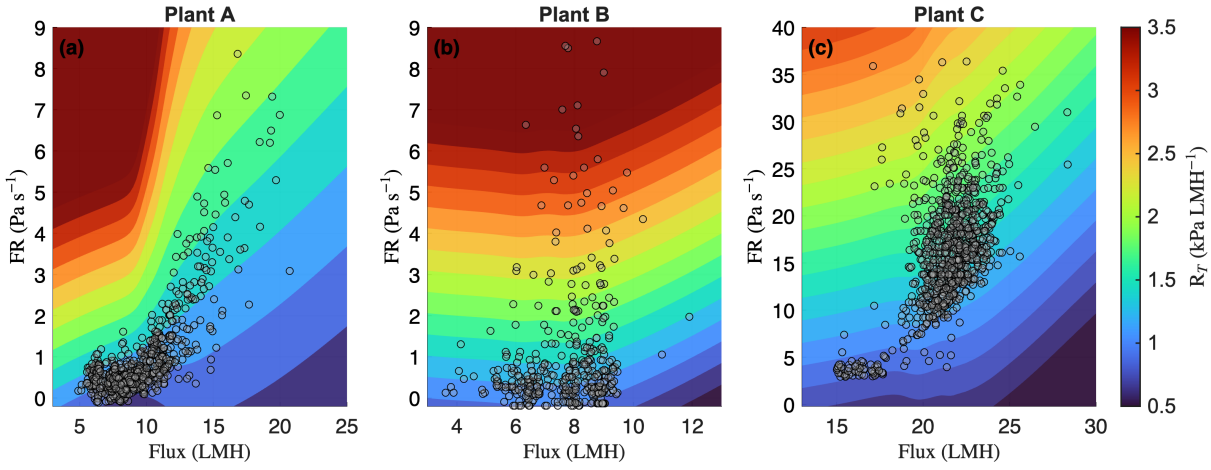


Figure 4.8: Fouling rate (FR) versus permeate flux, with total resistance (R_T) shown as color contours for Plants A, B, and C (panel (a), (b), and (c), respectively). The contours, smoothed using a LOWESS function to reveal the underlying trends, visualize the system's dynamic Actual Capacity by showing how the sustainable operational window shrinks as resistance increases.

The theoretical concept of Actual Capacity is directly substantiated by operational data. Figure 4.8 provides this data-driven evidence by plotting the FR against the permeate flux for

each plant, with R_T shown as color contours. These visualizations effectively map the system's sustainable operational window. Each contour line can be interpreted as an iso-capacity line, illustrating how the system's tolerance for a given flux diminishes as its fouling state (higher R_T) worsens. The distinct patterns confirm the unique operational characteristics of each plant. Plant A exhibits a clear flux-dependent capacity limit. The fouling rate markedly increases once the flux surpasses 10–13 LMH at R_T above 1.5 kPa/LMH. In contrast, in Plant B, operating at a low flux, FR is primarily governed by the rising resistance, with instability accelerating as R_T approaches 2.0 kPa/LMH. This visualizes the erosion of Actual Capacity by internal fouling progression rather than external stress. Plant C reveals a highly sensitive system; the tightly packed contours signify a narrow operational window where slight increases in resistance or flux trigger rapid acceleration. This empirical evidence for the Actual Capacity concept enables operators to identify and avoid operational danger zones.

4.4.3 A Holistic Framework for MBR Management

Understanding the dynamics of Actual Capacity is the first step; the ultimate goal is to manage it effectively. The insights from this research culminate in the holistic management framework shown in Figure 4.9. This framework translates the 'sensing and responding' paradigm into a proactive control strategy, positioning fouling as the central variable bridging system Capacity (CAPEX) and operational costs (OPEX).

The framework illustrates the lifecycle dynamic of an MBR system. CAPEX determines the initial Design Capacity. During operation, the system is subjected to Stressors (e.g., flux demand and solid loading). These stressors induce fouling, which degrades the Actual Capacity of the assets. To mitigate fouling and maintain performance, operational responses (Actions) are required, incurring ongoing costs (OPEX). If fouling is not managed effectively, severe

irreversible fouling or accelerated membrane wear can necessitate premature membrane replacement (Overhaul), imposing significant capital reinvestment costs. A smart Control System is therefore essential to balance these perspectives.

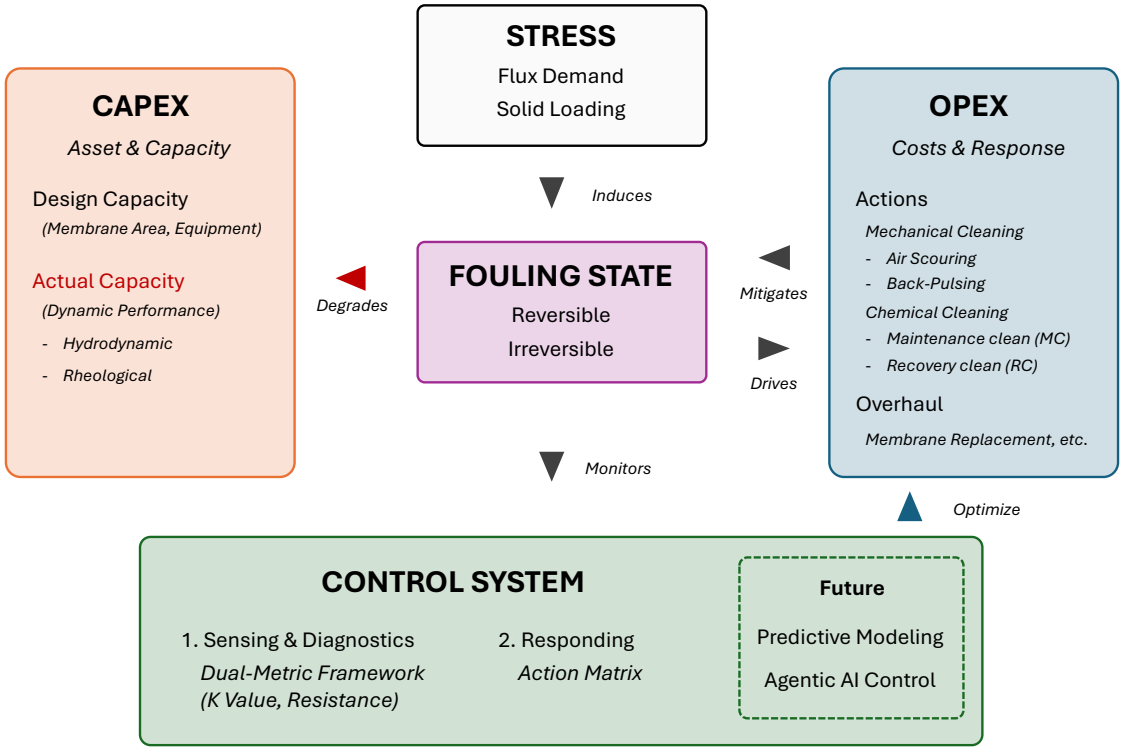


Figure 4.9: A holistic MBR management framework. Fouling acts as the central variable connecting system capacity (CAPEX) to operational control actions and long-term overhaul needs (OPEX). An intelligent control strategy based on real-time monitoring optimizes this entire lifecycle.

The core of this framework is a shift from rigid, pre-scheduled operations to a flexible, condition-based response enabled by the Control System:

1. Sensing and Diagnosis (Dual-Metric Framework): The K value and diagnostic resistance components provide the necessary real-time assessment of the fouling state and the current Actual Capacity.
2. Responding (Action Matrix): The diagnosis directly guides operational adjustments. The K value enables dynamic modulation of air scouring intensity for energy savings, while

the resistance analysis guides the optimal timing and intensity for BP and chemical cleanings (MC/RC), as prescribed by the Action Matrix (Figure 3.8).

The overarching goal of this proactive strategy is to maintain the highest possible membrane permeability by consistently operating within the system's sustainable Actual Capacity. This optimization minimizes OPEX while slowing the accumulation of irreversible fouling, thereby extending the time between major Overhauls. This approach preserves the long-term value of capital assets (CAPEX) while minimizing operational expenditures (OPEX), effectively bridging the gap between initial investment and sustainable, cost-effective operation. While the current framework focuses on diagnostic-driven control, it lays the essential foundation for the future integration of predictive models and agentic AI control (Chapter 5).

4.5 Conclusion

This chapter evaluated and generalized an integrated framework for membrane operation by applying it to three full-scale plants with distinct characteristics and fouling behaviors. The analysis confirmed that the dual-metric approach, combining the hydrodynamic K value with fouling-state indicators (R_T or detailed resistance components), is a robust and adaptable tool. It effectively diagnoses diverse fouling pathways driven by different stress types, including flux-driven cake formation (Plant A), resistance-driven instability (Plant B), and complex hybrid scenarios (Plant C).

Crucially, the findings provide strong empirical validation for the Actual Capacity concept as a unifying principle, explaining how membrane performance is dynamically governed by its current fouling state. The significance of this work lies in establishing a holistic, data-driven protocol that facilitates a paradigm shift in membrane management. This moves beyond a

reactive, fixed-threshold approach to a proactive strategy centered on managing the system's dynamic Actual Capacity.

This strategy allows operators to implement targeted actions to enhance stability, optimize air scour for energy savings, and reduce resource consumption. It not only improves daily operations (OPEX) but also preserves long-term membrane health by slowing irreversible fouling, thereby extending asset life and protecting capital investment (CAPEX). This framework paves the way for more intelligent and sustainable MBR operation. Future work should focus on integrating this diagnostic logic into automated control systems for real-time optimization. Further validation across a broader range of MBR configurations would strengthen its generalizability, and a detailed techno-economic analysis is recommended to quantify the long-term financial benefits of this proactive management approach.

Chapter 5 Discussion and Conclusion

5.1 Interpreting Fouling Dynamics through a Dual-Metric Framework

The operational challenges of membrane fouling are frequently understood through threshold phenomena, particularly the threshold flux (J^*). As formalized by Field and Pearce 2011, this concept provides a practical model by dividing the resistance rate into flux-independent (sub-critical) and flux-dependent (super-critical) components:

$$\frac{dR}{dt} \propto \begin{cases} a & \text{if } J \leq J^* \\ a + b \cdot (J - J^*) & \text{if } J > J^* \end{cases} \qquad \text{Equation (5.1)}$$

Here, 'a' represents a baseline, flux-independent rate of fouling. This is often attributed to slower mechanisms like the adsorption of SMP or gradual pore blocking, which typically manifest as persistent or irreversible fouling (related to R_{BP}) (Field and Pearce 2011; Ladewig and Al-Shaeli 2017; Miller et al. 2014; Sandoval-García et al. 2025). The term 'b' is a flux-dependent sensitivity factor that governs the rate of fouling when the operating flux (J) exceeds the threshold ($J > J^*$). This accelerated fouling is driven by the convective deposition of mixed liquor onto the membrane, typically leading to rapid cake accumulation (related to R_{cake}) (Drews 2010; Field and Pearce 2011; Wang and Wu 2009).

It is important to recognize the limitations of this model. Equation 5.1 is a piecewise linear model that effectively describes the transition observed around K_{Target}, where fouling begins to accelerate. However, it cannot capture the exponential increase in the fouling rate observed at K_{Lim}. Near this limit, the assumption of a constant sensitivity factor 'b' breaks down, initiating the Cake Compression Feedback loop (Chapter 3.5). While the distinction between

these 'a' and 'b' components is useful, the model's fundamental limitation is its assumption that J^* is a static value. In reality, J^* is a dynamic function of the system's hydrodynamic conditions, MLSS characteristics, and current fouling state. This dissertation reframes this variable threshold as the Actual Capacity. The K value operationalizes this concept by approximating the thresholds points with K_{Target} and K_{Lim}.

A dimensional analysis of the K value offers another insight into its physical meaning. Assuming MLSS concentration (g/L) is treated conceptually as a dimensionless mass fraction (implicitly normalized by fluid density during the empirical derivation), the derived units of K (m·s/kg) correspond precisely to the inverse of dynamic viscosity (1/μ), which represents fluidity. This interpretation suggests that the K value is not merely an empirical index but a physically interpretable measure of the hydrodynamic state near the membrane surface.

In this context, the K value can be understood as an indicator of the effective fluidity within the concentration polarization boundary layer. A high K value signifies high effective fluidity, implying that the boundary layer is relatively thin or less dense, allowing applied shear energy to be efficiently transmitted to the membrane surface for foulant removal. Conversely, a low K value indicates reduced fluidity (higher local effective viscosity), which dampens shear transmission (shear attenuation) and promotes deposition. K_{Target} can thus be interpreted as the minimum effective fluidity required to maintain a sustainable hydrodynamic balance.

The necessity for this dynamic, state-dependent perspective is illustrated by an anomaly observed in Plant C during a period of high solids loading. This case highlights a critical nuance regarding the nature of hydrodynamic stress. While the K value robustly quantifies the magnitude of stress (or the effective fluidity), the stress can originate from two distinct sources

kinetic stress (driven by high permeation drag due to high flux) and rheological stress (driven by high solids concentration/viscosity, leading to shear attenuation).

While K is a robust macroscopic indicator, the underlying force balance (Appendix A) at the membrane surface differs depending on which stress type is dominant, even at the same K value. In the high MLSS, low flux condition (initial Plant C), the system was dominated by rheological stress. The high viscosity compromised the hydrodynamics, which lowered the calculated K value below the empirical K_{Target}. However, the driving force for deposition (permeation drag) was relatively weak due to the low operating flux (low kinetic stress). Consequently, the actual rate of deposition did not exceed the rate of removal. This indicates that the operating flux was still below the system's actual threshold (J_*). The empirical K_{Target}, calibrated under more typical conditions, was limited to accurately reflect the J^* under these rheological conditions. Fouling remained governed by the baseline mechanism (the 'a' term) until the K value deteriorated significantly further, approaching K_{Lim}, at which point the threshold was finally crossed ($J > J^*$).

This analysis underscores an important insight that the J^* depends not just on the magnitude of hydrodynamic stress, but also on its nature, whether kinetic or rheological. Because the K value integrates both stress types, an ambiguity can arise where the same K value represents different underlying physical conditions and thus different proximity to J_*. This inherent limitation of using the K value alone reinforces the necessity of the dual-metric framework. Monitoring both the K value and the resistance components is essential for an accurate diagnosis.

By integrating the K value with resistance analysis, the dual-metric framework captures this nuance. It moves beyond the static assumptions of traditional models (Eq. 5.1), offering a

dynamic, state-dependent assessment of the system's Actual Capacity. This refined understanding of how different stressors interact with the evolving fouling state is essential for accurately predicting the MBR's true operational limits.

5.2 Contributions and Originality

This research makes a primary contribution by bridging the gap between theoretical fouling models and their practical application in full-scale submerged MBR operations. While previous work often focused on lab-scale mechanistic studies or isolated phenomenological observations in full-scale plants, this study systematically integrates these two domains by operationalizing theoretical concepts (e.g., force balance, threshold flux) using long-term, high-frequency industrial data.

The core originality lies in the development and validation of the dual-metric framework, which quantifies complex fouling dynamics using two operationally accessible indicators: the K value, representing hydrodynamic stress, and the diagnostic resistance components (R_{BP}, R_{cake}), reflecting the cumulative fouling state and its nature. This integrated system enables a proactive and mechanistic understanding of the MBR's internal state, moving beyond traditional monitoring based solely on TMP or permeability.

Furthermore, the concept of Actual Capacity, proposed and validated herein, offers a new theoretical lens for MBR performance. This paradigm reframes the MBR not as a device with fixed design limits, but as a dynamic or complex adaptive system whose operational boundaries are constantly shifting in response to internal states (fouling accumulation) and external stresses (flux demands). This perspective provides a fundamental explanation for why rapid fouling events can occur unpredictably, even under seemingly stable operating conditions, by illustrating how the sustainable capacity degrades over time.

5.3 Practical Implications

The findings provide a methodology to transition MBR operation from a reactive troubleshooting, experience-based approach to a proactive, data-driven science. This fundamentally shifts the operational paradigm toward proactive system health management. Analogous to human health monitoring, the K value serves as an indicator of acute hydrodynamic 'stress', signaling immediate risk. In contrast, the resistance components (e.g., R_{BP}) reflect the system's underlying 'health condition' or vulnerability. By continuously monitoring both stress and health, operators can make informed decisions to optimize performance and ensure long-term system resilience, rather than simply responding to failures.

This shift creates tangible value by addressing key barriers to the widespread adoption of MBR technology with operational stability and economic viability. Specific benefits include:

1. Dynamic control of air scour, guided by the K value thresholds, can offer reduction of aeration costs. The framework ensures that sufficient aeration is provided in response to hydrodynamic necessity, enhancing the economic competitiveness of MBR technology.
2. By sensing abrupt fouling events through the continuous monitoring of the Actual Capacity (the dynamic interplay of stress and health), the framework ensures stable and reliable production of high-quality treated water.
3. The primary goal of the control matrix is to minimize the necessity of harsh RC events, not to encourage premature cleanings. membrane longevity is inversely correlated with cumulative chemical exposure, which causes oxidative degradation. By guiding timely and appropriately scaled proactive interventions (e.g., optimized BP and MC based on resistance components), the framework reduces the frequency of RCs.

5.4 Limitations of the Study

While the findings are significant, several limitations should be acknowledged to contextualize the results and guide future work.

The framework is expected to be globally applicable, as its core metrics, the hydrodynamic K value and fouling resistance, are fundamental to submerged MBR operation. Its generalizability, however, requires further validation. The model was developed using data from three plants, all of which employed a specific corrugated flat-sheet membrane that hydrodynamically behaves as a flat sheet structure but has the advantage of having extra permeation surface due to its corrugation. Consequently, its applicability to other configurations, such as conventional hollow-fiber, dedicated flat-sheet systems, or ceramic type membrane, or to facilities treating substantially different wastewater types (e.g., highly industrial influents, high solid concentration), remains to be confirmed.

The K value model itself may warrant refinement. The current formulation assumes relationships with MLSS and TMP that may not be perfectly linear across all operational ranges. Specifically, the squared terms for MLSS and viscosity, derived from the initial theoretical framework, might overestimate their influence under certain conditions. Future iterations of the model could be improved by incorporating quantifiable sludge characteristics (e.g., filterability, particle size distribution, or refined viscosity correlations) to provide a more mechanistically robust index.

The framework's ability to diagnose specific fouling components (R_{BP} vs. R_{cake}) is contingent on the availability of BP data. In systems lacking this feature (such as Plant B), the overarching dual-metric approach using R_T still provides a robust foundation for control, though diagnosing the precise fouling trajectory and determining tailored actions are more challenging.

The model is inherently phenomenological. Rather than requiring challenging real-time characterization of feed MLSS properties (e.g., EPS/SMP concentrations), the framework implicitly accounts for their impact through their net effect on TMP and resistance. This is a strength in terms of practical implementation, allowing operators to rely on these calculated metrics to assess system status and initiate appropriate interventions, regardless of shifts in colloidal content or organic load. This utility reinforces that the most critical task for long-term application is the diligent recalibration of operational thresholds to account for long-term shifts in wastewater characteristics and membrane aging.

5.5 Future Research Directions

The diagnostic framework established in this dissertation provides the essential state representation for a new generation of intelligent MBR control systems. Future research should progress along a three-stage roadmap: From Diagnostics to Full Autonomy and Scalability, transforming the current condition-based system into a fully autonomous, predictive, and scalable management paradigm.

5.5.1 From Reactive to Proactive Control via Predictive Modeling

The immediate next step is to evolve the current diagnostic model into a proactive, feed-forward control system. This involves developing advanced time-series forecasting models, such as hybrid CNN-LSTM, Sequence-to-Sequence (Seq2Seq), or emerging Transformer-based architectures for time-series, trained on extensive historical data incorporating the dual metrics. Such a model could accurately forecast key variables like TMP, permeability or its rate changes, enabling the system to anticipate breaches of the fouling threshold and implement preemptive actions (e.g., adjustments in air scour). This shifts the operational paradigm from cleaning fouled membranes to preventing significant fouling in the first place.

5.5.2 From Predictive Control to Autonomous Optimization via Reinforcement Learning

Building upon predictive capabilities, a truly autonomous, self-optimizing system can be developed using Deep Reinforcement Learning (DRL). This requires formally defining the MBR as a Markov Decision Process (MDP), where a DRL agent learns to discover control strategies that surpass human-defined heuristics. The agent utilizes the dual-metric framework as its state input. The agent's goal is to optimize a multi-objective reward function balancing short-term operational costs (energy, chemicals) with long-term asset health (minimizing irreversible fouling). A practical and low-risk path to deployment involves a hybrid training strategy: initial policy learning using Offline (Batch) RL on historical data, pre-training the agent via behavioral cloning to mimic this dissertation's Action Matrix, and conducting final online fine-tuning with the Action Matrix serving as a permanent "safety net" (Safe RL) to prevent catastrophic actions.

5.5.3 From Single-Plant Autonomy to Fleet-Wide Intelligence via Hierarchical Models

The final challenge is to ensure model transferability and scalability across a fleet of diverse MBRs. This can be addressed by applying Bayesian hierarchical (or multi-level) models. This statistical approach enables "information borrowing," where a model for a plant with sparse data is robustly informed by trends from the entire fleet. This would not only allow for the rapid commissioning of new plants by providing robust initial model parameters (a solution to the "cold start" problem) but also create a powerful framework for fleet-wide anomaly detection and data-driven design for future systems, ultimately closing the loop between operations and engineering.

The synthesis of these approaches, a robust diagnostic framework, predictive modeling, and self-learning algorithms integrated within a hierarchical structure, presents a clear and achievable path toward the true optimization of MBRs as complex systems.

5.6 Conclusion

In summary, this dissertation identified the dynamic and interdependent nature of hydrodynamics and membrane fouling as a central challenge in MBR operation. It addressed this by developing a dual-metric diagnostic and control framework that integrates real-time indicators of hydrodynamic stress and fouling state. The introduction of Actual Capacity as a concept provides a unifying understanding of MBRs as dynamic systems with variable operational limits. By translating these theoretical insights into a practical control methodology, this work offers a clear pathway toward more reliable, energy-efficient, and economically sustainable MBR operation, strengthening their role in global water resource management.

Appendices

Appendix A: Theoretical Foundations of Threshold Phenomena in MBR Systems: A Spectral Perspective

A.1 Background and Purpose

Despite decades of research, membrane bioreactor (MBR) fouling remains a significant operational challenge, often culminating in abrupt 'TMP jumps' that conventional models fail to predict. This appendix establishes the theoretical foundation for the data-driven management strategy proposed in this dissertation. It frames this operational unpredictability not as a model deficiency to be corrected, but as an intrinsic feature of the MBR when understood as a Complex Adaptive System. It aims to establish the theoretical validity of the data-driven management strategy proposed in this dissertation, specifically supporting the use of the K_{Target} and K_{Lim} thresholds. This text deconstructs the limitations of traditional deterministic models by integrating fundamental Mass Balance (MB) and Force Balance (FB) principles with a complex systems perspective.

The purpose is to provide the foundational argument for a paradigm shift in MBR control. This shift is essential because the inherent complexity of MBRs makes precise prediction a futile pursuit, a reality that often forces operators into a cycle of reactive troubleshooting only after problems arise. The new paradigm, therefore, moves toward proactive management. Such an approach is critically dependent on the guidance of robust, high-dimensional indicators. These indicators are the essential tools that allow for effective, adaptive

control of the system's dynamic state, enabling operators to anticipate and mitigate fouling before it becomes a critical issue.

A.2 The Deterministic Paradigm: Concepts and Assumptions

The initial approach to managing membrane fouling, the primary constraint on MBR efficiency, was rooted in a deterministic paradigm, seeking singular flux thresholds to delineate safe operation.

A.2.1 The Critical Flux Concept and Taxonomy

The "Critical Flux" (J_S) concept (Field et al. 1995) proposed a threshold below which fouling is negligible. The premise is based conceptually on a hydrodynamic balance where back-transport mechanisms (e.g., shear-induced diffusion) equal or exceed convective transport. As MBR complexity became apparent, this concept evolved into a nuanced taxonomy (Appendix Table A.1).

The "Strong Form" (J_{cs}) represents an idealized zero-fouling scenario, defined by the initial deviation from the clean water flux-TMP linearity (Bacchin et al. 2006; Field et al. 1995). This is generally unattainable due to instantaneous adsorption (Bacchin et al. 2006; Miller et al. 2014). The "Weak Form" (J_{cw}) acknowledges flux-independent adsorption, marking the onset of significant flux-dependent fouling, such as cake formation (Field and Pearce 2011). The "Critical Flux for Irreversibility" (J_{ci}) identifies the flux above which irreversible fouling forms, linked to a phase transition from a dispersed to a condensed phase (Bacchin et al. 2006).

One operationally extended concept is the "Limiting Flux" (J_L), the maximum achievable flux where mass transport limits the system (Bacchin et al. 2006; Bowen and Jenner 1995). The "Threshold Flux" (J_{th}) is a pragmatic limit separating low and high fouling rate regions (Field and Pearce 2011). The "Sustainable Flux" (J_{sus}) represents a techno-economic optimization

balancing CAPEX and OPEX (Le-Clech et al. 2006). Additionally, the "Boundary Flux" (J_b) attempts to unify J_c and J_{th} into a single threshold distinguishing between constant and rapidly increasing permeability loss regimes (Stoller and Ochando-Pulido 2014), suggesting both concepts stem from the same fundamental physical phenomena. The shift towards operational concepts reflects the recognition that MBRs inherently foul, necessitating management rather than idealized prevention.

Appendix Table A.1: Taxonomy of Threshold Flux Concepts in MBR Operation

Term	Definition	Theoretical Basis
J_{cs} (Strong)	Flux below which no fouling occurs.	Idealized non-fouling condition ($R_T=R_m$).
J_{cw} (Weak)	Onset of significant flux-dependent fouling.	Transition from adsorption to cake formation ($R_T=R_m+R_{ads}$).
J_{ci}(Irreversibility)	Onset of irreversible fouling.	Phase transition from dispersed to condensed matter.
J_L (Limiting)	Maximum achievable flux.	Maximized resistance/Transport equilibrium.
J_{th}(Threshold)	Separates low/constant fouling rate from high/accelerating rate.	Transition point in fouling dynamics.
J_{sus}(Sustainable)	Economically optimal flux.	Techno-economic optimization (CAPEX vs. OPEX).
J_b (Boundary Flux)	Unified concept merging Jc and Jth.	Mathematical model defining constant vs. accelerating permeability loss.

A.3 Mechanistic Foundations: Mass Balance and Force Balance Perspectives

The traditional deterministic approaches discussed above can be built upon the integration of two fundamental principles: Mass Balance (MB), which describes the macroscopic transport of particles, and Force Balance (FB), which governs their microscopic stability and adhesion at the membrane interface.

A.3.1 The Integrated Framework

Fouling is a multi-scale phenomenon resulting from the interplay of macroscopic transport kinetics and microscopic interfacial stability thermodynamics. MB analyzes the macroscopic transport of foulants within the boundary layer adjacent to the membrane surface as

shown in Equation A.1 (Bowen and Jenner 1995). It governs the rate of accumulation, determining the concentration of material at the membrane surface (C_w). The fundamental principle is the conservation of mass, where the net flux of foulants ($N = J_{convective} - J_{back}$) is the difference between convective transport toward the membrane ($J_{convective} = J_v \cdot C$) and back-transport away from it ($J_{back} = D_{eff} \cdot dC/dx$) (Davis and Sherwood 1990; Romero and Davis 1991). Here, J_v is the permeate flux, C is the local foulant concentration, D_{eff} is the effective diffusion coefficient, and dC/dx is the concentration gradient normal (x) to the membrane surface. The mass balance is applied both in steady-state and dynamically. At steady-state (N=0), the fluxes are balanced, establishing Concentration Polarization (CP). Integrating the differential mass balance ($J_v \cdot C + D_{eff} \cdot dC/dx = 0$) across the boundary layer, often idealized using Film Theory, yields the equation quantifying CP (Bowen and Jenner 1995; Trettin and Doshi 1980):

$$J_v = k \cdot \ln\left(\frac{C_w}{C_b}\right) \qquad \text{Equation (A.1)}$$

where k is the mass transfer coefficient, which represents how effectively the operating hydrodynamics (shear and mixing) can remove accumulated material from the membrane surface (Van Den Berg et al. 1989), and C_b is the bulk concentration. Dynamically, when convective flux exceeds back-transport capacity (N>0), material accumulates. The rate of accumulation of cake mass (M) is modeled as:

$$\frac{dM}{dt} = J_v - J_{ss} \cdot C \qquad \text{Equation (A.2)}$$

where M is mass per unit area (e.g., kg/m^2) and J_{SS} represents the steady-state or critical flux threshold below which accumulation is mitigated (Bugge et al. 2012; Jørgensen et al. 2012; Liang et al. 2020).

FB analyzes the microscopic forces acting on individual particles near the membrane surface (Equation A.3). It governs the stability of the foulants, determining the conditions necessary for adhesion (particle-membrane) and cohesion (particle-particle) (Bacchin et al. 1995; Kang et al. 2004; Shen et al. 2015). The framework analyzes the equilibrium between deposition forces and removal/repulsion forces (Bacchin et al. 2002, 2005; Petseva et al. n.d.; Wang and Li 2012):

$$F_{Drag} + F_{Attraction} \approx F_{Shear/Lift} + F_{Repulsion} \qquad \text{Equation (A.3)}$$

FB dictates the ultimate fate of the accumulated material, whether it remains dispersed, adsorbs reversibly, or undergoes an irreversible phase transition, and governs the structural properties of the resulting fouling layer. The FB is typically quantified using the XDLVO (Extended Derjaguin-Landau-Verwey-Overbeek) theory, which calculates the total interaction energy (ΔG) as the sum of Van der Waals (LW), Electrostatic (EL), and Acid-Base/Hydrophobic (AB) interactions (Erkan et al. 2020; Hu et al. 2025; Kang et al. 2004; Qiao et al. 2022). The resulting energy profile determines the stability of the system.

The Integration of these frameworks is essential. MB determines the magnitude of C_w (the kinetics). FB determines the stability and adhesion potential of the material at that concentration (the thermodynamics of stability). FB defines both the propensity for spontaneous adsorption (related to the energy profile) and the critical aggregation concentration ($C_w \rightarrow C_c$) at which the accumulated mass undergoes a phase transition (Astudillo-Castro 2015; Bacchin et al. 2002). Furthermore, the FB directly informs the MB accumulation rate by defining the probability of attachment (E), which can be calculated from the ratio of deposition forces (e.g., F_{Drag}) to antagonistic forces (e.g., F_{Lift}) (Li and Wang 2006):

$$E \approx \frac{F_{Drag}}{F_{Drag} + F_{Lift}}$$ Equation (A.4)

It is the predicted breakdown of these two balances, the point where back-transport can no longer keep up (MB failure), or where adhesive forces overwhelm repulsive forces (FB collapse), that forms the theoretical basis for deterministic thresholds like the critical flux.

A.3.2 Defining Criticality

Criticality in MBRs is often associated with abrupt changes in fouling rates. However, fouling is a continuous process that begins prior to these critical events. The conceptual integration of MB and FB reveals a spectrum of fouling behaviors, ranging from initial adsorption to complete system saturation.

1. Sub-Critical Fouling (Adsorption and Reversible Deposition): Fouling can be initiated, even at low or zero flux conditions, independent of high permeation drag (F_{Drag}) (Bacchin et al. 2006; Miller et al. 2014). This occurs through spontaneous adsorption, where the membrane-foulant interaction is thermodynamically favorable. This contributes to an adsorption resistance (R_{ads}) recognized by J_{cw} (weak form). Within the XDLVO framework, this corresponds to conditions where the energy barrier is low or absent, allowing attachment at the Primary Energy Minimum (Bacchin et al. 1995). Alternatively, particles may be captured in the "Secondary Energy Minimum", resulting in weak, reversible attachment (Bacchin et al. 1995; Guo et al. 2012; Shen et al. 2015).
2. The stability limit (Force Balance Dominated): This defines the critical point where accumulated foulants lose their dispersed stability. While most clearly defined for colloidal systems (Bacchin et al. 1995, 2006; Wang and Li 2012), this principle extends broadly to the heterogeneous mixture in MBRs, including macromolecules (e.g., EPS/SMP) and flocs (Drews 2010; Mallah et al. 2024). It occurs when C_w (determined by

MB) reaches the Critical Concentration (C_c). This threshold represents the concentration required for aggregation (in colloidal systems) or gelation/solubility limit (in macromolecular systems). At this threshold, the FB collapses; attractive forces (or osmotic pressure limits for macromolecules) overwhelm repulsive/dispersive forces (Bacchin et al. 1995). This triggers a phase transition from a dispersed liquid phase (CP) to a condensed solid phase (gel or dense cake) (Wang and Li 2012). Operationally, this limit corresponds to the onset of irreversible fouling (J_{ci}), marking the transition from reversible accumulation to multi-layer deposition (Li and Wang 2006). During this transition, the rate of fouling deposition becomes highly sensitive to local operating conditions, a phenomenon that is itself central to the threshold flux concept (Field and Pearce 2011).

3. The transport limit (Mass Balance Dominated): This defines the absolute physical capacity of the system. It occurs when C_w reaches the Maximum Packing Concentration (C_{max}) (Davis and Sherwood 1990). At this point, the system's transport capacity is fully saturated (MB Saturation), leading to an exponential increase in hydraulic resistance (N. Petford 2009; Yang et al. 2009). Operationally, this corresponds to the Limiting Flux (J_L). The stability limit is generally reached before the transport limit ($C_c < C_{max}$).

While this framework provides clear, mechanistic definitions for thresholds, its practical application is profoundly complicated by the fact that these limits are not singular, uniform values in a real, heterogeneous MBR system.

A.3.3 Factors Influencing the Mechanistic Balances

The stability of the MB and FB is critically influenced by the operational environment, the rheological properties of the mixed liquor, and the characteristics of the biomass.

1. Hydrodynamics (air scouring, cross-flow velocity) generates wall shear stress (τ_w) (Carrère 2000; Drews 2010; Du et al. 2017b; Ratkovich et al. 2013). This shear enhances MB by increasing the effective diffusion coefficient (D_{eff}), which promotes back-transport (Belfort et al. 1994; Davis 1992). Simultaneously, it enhances FB by increasing hydrodynamic lift forces ($F_{Shear/Lift}$), directly counteracting deposition (Drews 2010; Kang et al. 2004).
2. Rheology, MLSS, and Temperature are intrinsically linked. MLSS concentration is the dominant factor determining sludge viscosity (Le-Clech et al. 2006; Meng et al. 2007; Pradhan et al. 2022). MBR sludge exhibits non-Newtonian (shear-thinning) behavior, and viscosity increases exponentially with MLSS, often dramatically above a critical threshold (e.g., 8-12 g/L) (Delgado et al. 2008; Meng et al. 2005; Ratkovich et al. 2013). Increased viscosity profoundly shifts the balance toward accelerated fouling by dampening the transmission of shear (reducing effective τ_w; shear attenuation) (Jeison and Van Lier 2006; Meng et al. 2007; Trussell et al. 2007; Yang et al. 2009), reducing back-transport coefficients (MB), and increasing permeation drag (FB). Temperature significantly impacts this dynamic; lower temperatures increase viscosity, exacerbating the negative rheological effects (Le-Clech et al. 2006).
3. Sludge Characteristics play a crucial role. The Particle Size Distribution (PSD) is the most critical factor, as the interplay between back-transport (MB) and adhesion (FB) creates distinct fouling behaviors at different scales (Appendix Table A.2). Large flocs (> 10 μm) and bacteria (1–10 μm) are effectively managed by hydrodynamic forces, forming relatively manageable, reversible cake layers (Belfort et al. 1994). However, a critical "Fouling Window" emerges between 0.1–1 μm. In this range, back-transport

mechanisms are at their weakest, allowing sticky colloidal particles (EPS) to accumulate on the membrane (Li and Wang 2006; Mcdonogh et al. 1989; Meng et al. 2017). Once there, FB determines their fate; they mediate strong adhesive forces through hydrophobic interactions and ion bridging, initiating dense, hard-to-remove irreversible fouling. Even smaller colloids (< 0.1 μm) contribute to it fouling by directly blocking membrane pores (Meng et al. 2017).

Appendix Table A.2: Dominant Back-Transport Mechanisms and the "Fouling Window"

Particle Size Range	Typical Foulant	Dominant Mechanism	Scaling Relationship	Relative Importance
< 0.1 μm	SMPs, fine colloids	Brownian Diffusion	$D_B \propto 1/a$	Irreversible; pore blocking & adsorption
0.1 – 1 μm	Colloidal EPS	Weakest transport	N/A	"Fouling Window": Primary initiators of irreversible fouling.
1 – 10 μm	Bacteria, micro-flocs	Shear-Induced Diffusion	$D_S \propto a^2$	Reversible; Dominant for cake layer control.
> 10 μm	Large sludge flocs	Inertial Lift	$F_{Lift} \propto a^3$	Highly Reversible; Strong back-transport prevents firm deposition.

* where 'a' represents the particle radius.

A.3.4 The Interplay of Mechanisms and Operational Challenges

The interaction between these factors creates complex operational challenges related to fouling layer stability and the limits of physical cleaning. Once the stability limit is crossed, a condensed fouling layer forms. The removal of this layer requires the applied hydrodynamic shear to exceed the layer's cohesive strength or yield stress (Du et al. 2017a; Yang et al. 2009). The mechanical properties of this layer, its compressibility and yield stress, are governed by the FB interactions, particularly the bridging effects of EPS (Choo and Lee 1998; Yang et al. 2009).

Furthermore, under increased TMP, the compressible cake layer undergoes compaction. This phenomenon increases the specific cake resistance (α) non-linearly with pressure (Bugge et al. 2012; Guo et al. 2012; Ho and Zydney 2000; Vera et al. 2015), often modeled as:

$$\alpha = \alpha_0(\Delta P)^s \qquad \text{Equation (A.5)}$$

where α_0 is the resistance at zero pressure and 's' is the compressibility coefficient, both of which must be empirically determined as they depend on complex, system-specific sludge properties (like particle structure and cohesion) that theoretical models alone cannot accurately predict. Compaction elevates the yield stress, making the layer significantly more difficult to remove via physical cleaning and often necessitating chemical intervention (Benkahla et al. 1995; Du et al. 2017b; Yang et al. 2009).

Efforts to mitigate fouling by increasing shear can be counterproductive. Excessively vigorous air intensity can cause floc breakup (Ding et al. 2016; Du et al. 2017b). This shifts the PSD toward the "fouling window" and releases bound EPS/SMPs (Wang and Li 2012; Zsirai et al. 2012). These fine materials can accelerate pore blocking or form denser, more irreversible gel layers with higher yield stress, potentially increasing the overall fouling propensity despite increased energy input (Chang et al. 2002; Desmond et al. 2022; Ying et al. 2010). This highlights the complex, non-linear interplay between hydrodynamics, rheology, biology, and transport mechanisms.

A.3.5 The Amplifying Dimensions of Operational Complexity

Beyond the inherent non-linearity of the fouling mechanisms, the challenge of modeling a full-scale MBR is profoundly amplified by operational complexities that introduce additional dimensions of space, time, and context. These dimensions transform the system from a predictable reactor into a dynamic entity where simple cause-and-effect relationships break down.

A membrane module is not a uniform system, as local operating conditions vary dramatically across its surface and depth, leading to spatial heterogeneity in fouling. For

instance, local flux and the intensity of air scouring are inconsistent across the membrane area (Cho and Fane 2002), while physical gradients, such as an increase in sludge concentration with height, create a spectrum of fouling potentials rather than a single state (Li and Wang 2006). This spatial complexity is compounded by the system's temporal dynamics; it is in constant flux, with sludge characteristics shifting with daily load variations and seasonal temperature changes. Furthermore, each MBR installation possesses a unique "context", its physical geometry and upstream biological processes, adding a final layer of site-specific variability that defies universal modeling.

Consequently, creating a deterministic model that can accurately predict and control a full-scale MBR becomes an exceptionally challenging, if not intractable, task. The operational reality is not a steady state but a dynamic, heterogeneous system prone to emergent behaviors. The very term "TMP jump" encapsulates this reality, signifying a sudden, unpredictable, and system-level failure that simple, linear prediction cannot foresee.

A.4 MBR as a Complex Adaptive System

The limitations of the deterministic paradigm necessitate a fundamental shift in perspective. MBRs need to be understood through the lens of a Complex Adaptive System proposed by (Holland 2006), a framework for dynamic networks where the collective behavior of the whole is unpredictable from its individual components alone. Given the highly heterogeneous environment of an MBR, with its constant interplay of biological, physical, and chemical interactions, it exhibits all the key characteristics of such a system.

The MBR exhibits all the key characteristics of a complex system, as summarized in Appendix Table A.3. At its core, the system is a dynamic network of heterogeneous agents that adapt to their environment (Holland 2006). Their interactions are highly non-linear, leading to

system-level self-organization through the formation of structures like the fouling layer, and the continuous reorganization of these structures in response to external forces (e.g., shear, compression, cleaning) and adaptive biological processes (Guo et al. 2012, 2020; Sandoval-García et al. 2025). This process is critically destabilized by powerful positive feedback loops, which are self-reinforcing cycles where an initial change triggers a series of events that amplify that original change, often leading to instability and rapid, non-linear effects (Holland 2006). Key examples in the MBR system include flux redistribution, a cascade failure driven by spatial heterogeneity, and cake compression feedback loop, a vicious cycle of rising pressure and resistance that often necessitates chemical intervention (Cho and Fane 2002; Hwang et al. 2008; Vera et al. 2015; Wang and Li 2012).

The collective result of these interacting characteristics is emergence, the appearance of novel, system-level behaviors unpredictable from the individual components. The "TMP jump" is the quintessential emergent property in MBRs; it is a sudden, system-level phase transition that occurs when the collective behavior, driven by the aforementioned feedback loops, crosses a critical tipping point. Crucially, recognizing the TMP Jump as an emergent phenomenon implies that perfect deterministic prediction is inherently impossible. This realization is the foundation for the paradigm shift advocated in this dissertation, moving away from prediction and toward adaptive management.

Appendix Table A.3: MBR Characteristics from a Complex Systems Perspective

CAS Characteristic	MBR System Example
Heterogeneous Agents	Bacteria, colloids, EPS, SMPs.
Non-linear Interactions	Exponential TMP increase near critical points.
Positive Feedback Loops	Flux Redistribution; Cake Compression Feedback Loop.
Self-organization	Formation of complex cake/biofilm structures.

Adaptation	Microbial communities shifting EPS production under stress.
Emergent Properties	The sudden phase transition (TMP Jump).

A.5 The Spectral Interpretation of Threshold Phenomena

The complex and emergent nature of the MBR invalidates the concept of a single, deterministic threshold. This reality guides the paradigm toward a statistical interpretation of the system's limits, formalized in the Distribution of Critical Flux (DCF) model (Bacchin et al. 2005). This approach characterizes fouling behavior not by a single value, but by the system's inherent heterogeneity, represented by a mean critical flux ($\bar{J}_c$) and a standard deviation (σ).

The DCF model provides a conceptual framework for understanding why the onset of critical fouling ($\bar{J}_{c,\,exp}$; experimentally measured) is observed well below the theoretical average capacity ($\bar{J}_c$). Statistically, $\bar{J}_{c,\,exp}$ aligns with the lower tail of the distribution (approximated as the 30th percentile in the idealized model). Physically, this signifies that fouling initiates in the most vulnerable fractions of the membrane. While real fouling involves complex phenomena like cake compaction and porosity changes rather than simple binary blockage, the fundamental consequence of this heterogeneity remains the same: as vulnerable areas experience reduced permeability, flux is inevitably redistributed to the remaining areas. This redistribution increases local flux, triggering a cascading failure that accelerates the overall fouling rate long before the average threshold is reached. This interpretation is supported by direct physical observations (Li 2000), which correlate the onset of significant deposition with a threshold level of initial surface coverage (≈30%).

This understanding of critical fouling as an emergent property of a heterogeneous system provides a compelling bridge to the widely observed $J_c \approx 2/3\ J_L$ relationship. This relationship, independently derived from mass transport models (Bacchin 2004), is robustly validated by the

DCF framework. The DCF model shows the ratio $\bar{J}_{c,\,exp} / J_L$ depends primarily on the Relative Standard Deviation (RSD = μ / $\bar{J}_c$), a measure of the system's relative heterogeneity:

$$\frac{\bar{J}_{c,exp}}{J_L} \approx 1 - \left(\frac{RSD}{2}\right) \qquad \text{Equation (A.6)}$$

Crucially, while absolute heterogeneity (σ) varies, the RSD often remains stable across different operating conditions. When the RSD is approximately 0.66 (as observed in Bacchin et al. 2005), the ratio is 0.67. The stability of the RSD explains why the "2/3 rule" persists as a robust macroscopic observation, despite the underlying microscopic complexities of fouling mechanisms. This robustness is further confirmed by independent analytical derivations (e.g., the exponential model yielding 0.632 (Astudillo-Castro 2015)) and experimental validations (e.g., the observed ratio of 0.69 in MBR systems (Jørgensen et al. 2014))

The convergence of these independent lines of evidence, statistical modeling of heterogeneity, physical observation of localized onset, and established mass transport theory, provides a strong justification for applying the "2/3 rule" to define practical operational limits, including the $K_{Target} \approx 2/3\ K_{Lim}$ relationship proposed in this dissertation.

A.6 The Paradigm Shift: From Prediction to Adaptive Management

The theoretical foundations established in this appendix (the mechanistic limits of Mass and Force Balance combined with the system's complexity, emergence, and spectral nature) mandate a paradigm shift: moving from the futile pursuit of 'Perfect Prediction' to the practice of 'Effective, Adaptive Management'. This new paradigm requires high-dimensional indicators capable of translating the complex system state into practical operational tools.

The Hydrodynamic Index (K value) proposed in this dissertation serves this function. By synthesizing key variables (shear, flux, viscosity, and resistance) into a single, integrated

parameter, the K value acts as a macroscopic indicator of the system's capacity spectrum, allowing for the identification of critical tipping points to guide robust operational strategies.

It is important, however, to recognize the relationship between this empirical indicator and the underlying microscopic theories (MB/FB). While these theories support the conceptual validity of the K value framework, the K value itself cannot be derived directly from first principles. A quantitative gap necessarily exists between idealized theory and the empirical model. Therefore, the K value should be understood as a macroscopic 'proxy' representing the complex system state. Recognizing this gap reinforces the dissertation's central argument: the limits of deterministic prediction must be acknowledged, necessitating a shift towards adaptive management guided by such robust proxies.

Crucially, the two data-driven K thresholds identified in Chapter 3, K_{Target} and K_{Lim}, are not mere empirical correlations; they are the macroscopic manifestations of the fundamental mechanistic limits: K_{Target} (stability limit) corresponds to the localized breakdown of the FB. It marks the operational point where stability collapses in the system's weakest zones (reaching C_c), initiating the phase transition (irreversible fouling) that seeds the flux redistribution feedback loop. K_{Lim} (The Transport Limit) corresponds to the saturation of the global MB. While theoretically linked to C_{max}, in compressible MBR systems, this limit is practically triggered by reaching a critical TMP, activating the cake compression feedback loop and leading to global system failure (TMP jump).

These thresholds define the three classic stages of fouling progression: stable operation (Phase 1: $K > K_{Target}$), accelerated propagation (Phase 2: $K_{Lim} < K < K_{Target}$), and system collapse (Phase 3: $K < K_{Lim}$). By directly linking an operational indicator (K) to the fundamental state of

the system (MB/FB), this framework validates the K value as a powerful, theoretically grounded tool for adaptive management.

A.7 Conclusion

This appendix has established a comprehensive theoretical foundation for MBR fouling. We have demonstrated that the system's inherent complexity (characterized by heterogeneity, non-linearity, and emergence) invalidates the traditional deterministic paradigm of a single fouling threshold. This reality necessitates a new framework, one that integrates the fundamental mechanistic limits of Mass and Force Balance with a complex systems perspective, leading to a spectral interpretation of system behavior.

The data-driven thresholds presented in this dissertation, K_{Target} and K_{Lim}, are shown to be the macroscopic manifestations of these fundamental limits: the stability limit (local Force Balance collapse) and the transport limit (global Mass Balance saturation and compression), respectively. The emergent nature of system failure, such as the TMP Jump, underscores the futility of perfect prediction. Therefore, the K value framework is validated not merely as an empirical tool, but as a theoretically sound and practically robust approach for the adaptive management of these inherently complex systems.

Appendix B: Data Processing Methodology

This appendix details the methodologies employed for processing raw operational data from the full-scale MBR facilities into structured, analysis-ready datasets. The focus is on the data pipeline architecture, the automated cycle classification algorithm, data normalization and cleaning procedures, and the resistance calculation protocol.

B.1 Overview of the Data Processing Pipeline

The analysis pipeline was developed within the MATLAB environment, utilizing the Statistics and Machine Learning Toolbox for analysis and the Parallel Computing Toolbox to accelerate the processing of large, high-frequency datasets. The pipeline is designed as a modular workflow that transforms raw sensor readings into a feature-rich dataset suitable for analysis and modeling.

The workflow follows a sequential process:

1. Data Acquisition and Pre-screening: Ingestion of raw time-series sensor data (e.g., TMP, flows, pressures) from the SCADA system and auxiliary operational logs (e.g., MLSS concentration, temperature, cleaning events, system status).
2. Resampling and Normalization: Standardization of data frequency and conversion to standard units.
3. Cycle Classification: Automated segmentation of the continuous time-series into discrete operational cycles (Permeation, Back-pulse, Cleaning).

4. Data Cleaning and Feature Engineering: Imputation of missing data, noise reduction, and calculation of derived operational metrics.
5. Resistance Calculation and Aggregation: Calculation of temperature-normalized resistance components and aggregation to lower frequencies for trend analysis.

This modular approach ensures reproducibility and allows for adaptation to different MBR facilities by adjusting plant-specific configuration parameters (e.g., membrane area).

B.2 Detailed Data Processing Steps

B.2.1 Resampling and Normalization

Raw data, often recorded at varying high frequencies, were first resampled to a consistent 15-second frequency. This standardization is crucial for aligning measurements from different sensors and reducing computational load while preserving the dynamics of operational cycles. Following resampling, the data underwent normalization and unit conversion:

1. Unit Conversion: All variables were converted to standard units (e.g., pressure to kPa).
2. Flow Normalization: Permeate and air scour flow rates were normalized based on the active membrane surface area, as recorded in the operational logs.
3. Flux Calculation: Permeate Flux (LMH) was calculated using the normalized permeate flow and the known active membrane surface area.

B.2.2 Automated Operational Cycle Classification

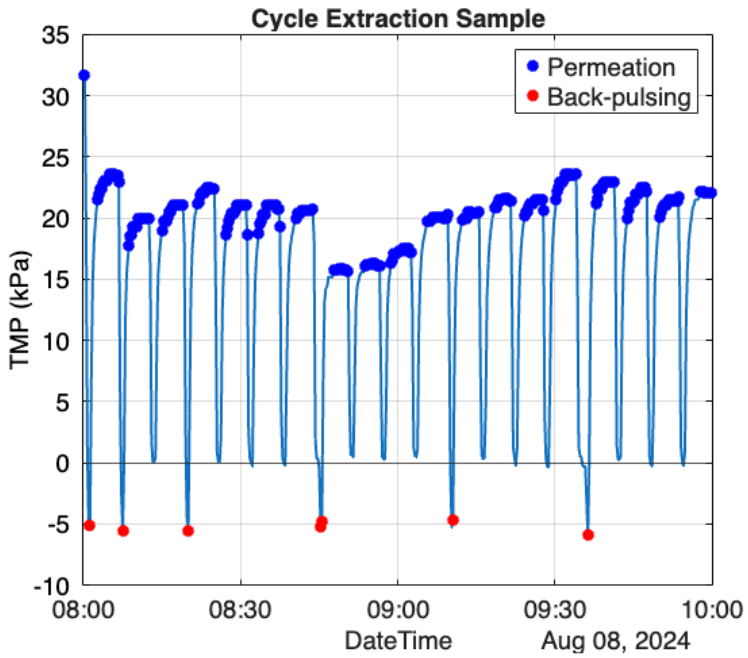
A critical step in the pipeline is the automated segmentation of the continuous time-series data into discrete operational states: Permeation (Production), Back-pulse Cleaning, and Chemical Cleaning (MC or RC). This segmentation is essential for the accurate calculation of resistance components specific to each operational phase.

The algorithm employs a multi-step approach combining signal thresholding and morphological analysis:

1. Signal Segmentation via Thresholding: The algorithm identifies potential operational states by applying thresholds to the TMP and Flux signals. Permeation cycles are characterized by positive TMP and Flux values consistently exceeding minimum operational thresholds. Conversely, non-permeation events are identified by significant deviations, such as near-zero TMP (Relaxation/Cleaning) or negative TMP/Flux (Back-pulsing).
2. Connected Components Analysis: To identify contiguous time intervals corresponding to a specific state, a Connected Components analysis (a technique utilized for grouping adjacent elements) is applied. This groups consecutive data points meeting the threshold criteria into distinct segments.
3. Cycle Refinement and Heuristics: The identified segments are refined based on expected duration constraints. For instance, segments must meet a minimum duration to be validated as a permeation cycle. Non-permeation segments are further classified into BP or Cleaning based on their duration. The algorithm includes logic to merge fragmented, temporally adjacent cleaning events into a single, contiguous cleaning event.

Figure B.1 illustrates an example output of the cycle classification algorithm applied to a TMP time series.

Appendix Figure B.1: Example output of the automated cycle classification algorithm. The algorithm successfully identifies and segments the time series into Permeation cycles (blue dots) and Back-pulsing events (red dots).



B.2.3 Data Cleaning and Feature Engineering

Real-world operational data often contain noise, gaps, and sensor errors that require robust processing. Wastewater temperature data, essential for viscosity correction, were processed to handle noise and sensor drift. A moving mean filter was applied to smooth the data. In cases where abrupt, non-physical step-changes were detected (indicative of sensor malfunction or recalibration), the data was segmented at the boundary of the shift. Smoothing was applied independently to the segments before and after the boundary to preserve the actual temperature trend while minimizing noise.

Accurate estimation of the MLSS concentration within the membrane tank is crucial, as it often differs from the concentration in the aeration basin due to solids thickening dynamics. Furthermore, MLSS sensors are prone to malfunctions and data gaps. A robust procedure was implemented to generate a continuous estimate of the average MLSS concentration in the membrane tank:

1. Mass Balance Framework: The procedure utilizes a mass balance around the membrane tank, incorporating the Feed MLSS, RAS MLSS, Permeate flow, and RAS flow.
2. Iterative Reconciliation: Due to potential gaps in both Feed and RAS sensor data, an iterative process is used. An initial estimate for RAS MLSS is derived from Feed MLSS sensor data using the mass balance equations, and vice versa. The algorithm iteratively uses one estimate to fill gaps in the other until the time series are complete and reconciled.
3. Final Estimation: The final reconciled Feed MLSS and RAS MLSS values are used to compute the average concentration within the membrane tank.

B.2.4 Resistance Calculation Protocol

The analysis relies on the decomposition of R_T into R_{BP} and R_{cake}. All resistance values were calculated based on Darcy's law and normalized to a reference temperature of 20°C to account for variations in water viscosity. The general form of the resistance calculation (using the operationally relevant unit kPa/LMH) is shown in Equation 3.9.

The decomposition utilizes the segmented data from the cycle classification algorithm. The specific timing protocols for measuring R_T and R_{BP} are critical for accurate decomposition (referencing Figure B.1):

1. R_T represents the resistance during the permeation cycle. It was calculated using TMP and Flux data measured during the permeation phase (e.g., the blue dots in Figure B.1). This measurement captures the resistance contribution of the fully developed dynamic cake layer in addition to persistent fouling and intrinsic membrane resistance.
2. R_{BP} represents the resistance measured during the BP cycle, serving as an operational metric for persistent or 'intact' fouling (irreversible fouling + intrinsic membrane resistance). It was calculated using the reverse TMP and BP flux data during the stable

phase of the BP cycle (e.g., the red dots in Figure B.1). Data from the very beginning and end of the pulse were typically excluded to avoid transitional hydrodynamic effects.

3. R_{cake} represents the dynamically accumulated cake layer removed by mechanical cleaning (e.g., BP or relaxation). It is calculated as the difference between R_T and R_{BP}.

B.2.5 Data Aggregation and Alignment

R_T and R_{BP} are inherently measured asynchronously during different operational phases. To calculate R_{cake} and analyze long-term trends, the high-frequency data must be aligned onto a common time basis. The processed high-frequency data (15-second intervals) were aggregated to lower frequencies, typically daily or 4-hourly intervals, using the median as the primary aggregation statistic. This aggregation step R_T and R_{BP}, enabling the calculation of R_{cake} at the aggregated frequency, and effectively smooths short-term fluctuations to reveal underlying operational trends.

Bibliography

Aslam, M., A. Charfi, G. Lesage, M. Heran, and J. Kim. 2017. “Membrane bioreactors for wastewater treatment: A review of mechanical cleaning by scouring agents to control membrane fouling.” *Chemical Engineering Journal*, 307: 897–913. https://doi.org/10.1016/j.cej.2016.08.144.

Astudillo-Castro, C. L. 2015. “Limiting Flux and Critical Transmembrane Pressure Determination Using an Exponential Model: The Effect of Concentration Factor, Temperature, and Cross-Flow Velocity during Casein Micelle Concentration by Microfiltration.” *Ind. Eng. Chem. Res.*, 54 (1): 414–425. https://doi.org/10.1021/ie5033292.

Bacchin, P. 2004. “A possible link between critical and limiting flux for colloidal systems: consideration of critical deposit formation along a membrane.” *Journal of Membrane Science*, 228 (2): 237–241. Elsevier. https://doi.org/10.1016/j.memsci.2003.10.012.

Bacchin, P., P. Aimar, and R. Field. 2006. “Critical and sustainable fluxes: Theory, experiments and applications.” *Journal of Membrane Science*, 281 (1–2): 42–69. https://doi.org/10.1016/j.memsci.2006.04.014.

Bacchin, P., P. Aimar, and V. Sanchez. 1995. “Model for colloidal fouling of membranes.” *AIChE Journal*, 41 (2): 368–376. https://doi.org/10.1002/aic.690410218.

Bacchin, P., B. Espinasse, and P. Aimar. 2005. “Distributions of critical flux: modelling, experimental analysis and consequences for cross-flow membrane filtration.” *Journal of Membrane Science*, 250 (1–2): 223–234. https://doi.org/10.1016/j.memsci.2004.10.033.

Bacchin, P., D. Si-Hassen, V. Starov, M. J. Clifton, and P. Aimar. 2002. “A unifying model for concentration polarization, gel-layer formation and particle deposition in cross-flow membrane filtration of colloidal suspensions.” *Chemical Engineering Science*, 57 (1): 77–91. https://doi.org/10.1016/S0009-2509(01)00316-5.

Barillon, B., S. M. Ruel, C. Langlais, and V. Lazarova. 2013. “Energy efficiency in membrane bioreactors.” *Water Science and Technology*, 67 (12): 2685–2691. https://doi.org/10.2166/wst.2013.163.

Belfort, G., R. H. Davis, and A. L. Zydney. 1994. “The behavior of suspensions and macromolecular solutions in crossflow microfiltration.” *Journal of Membrane Science*, 96 (1–2): 1–58. https://doi.org/10.1016/0376-7388(94)00119-7.

Benkahla, Y. K., A. Ould-Dris, M. Y. Jaffrin, and D. Si-Hassen. 1995. “Cake growth mechanism in cross-flow microfiltration of mineral suspensions.” *Journal of Membrane Science*, 98 (1–2): 107–117. https://doi.org/10.1016/0376-7388(94)00182-X.

Bhattacharjee, S., A. S. Kim, and M. Elimelech. 1999. “Concentration Polarization of Interacting Solute Particles in Cross-Flow Membrane Filtration.” *Journal of Colloid and Interface Science*, 212 (1): 81–99. https://doi.org/10.1006/jcis.1998.6045.

Bowen, W. R., and F. Jenner. 1995. “Theoretical descriptions of membrane filtration of colloids and fine particles: An assessment and review.” *Advances in Colloid and Interface Science*, 56: 141–200. https://doi.org/10.1016/0001-8686(94)00232-2.

Bugge, T. V., M. K. Jørgensen, M. L. Christensen, and K. Keiding. 2012. “Modeling cake buildup under TMP-step filtration in a membrane bioreactor: Cake compressibility is significant.” *Water Research*, 46 (14): 4330–4338. https://doi.org/10.1016/j.watres.2012.06.015.

Carrère, H. 2000. “Study of hydrodynamic parameters in the cross-flow filtration of guar gum pseudoplastic solutions.” *Journal of Membrane Science*, 174 (1): 135–145. https://doi.org/10.1016/S0376-7388(00)00378-1.

Chang, I.-S., P. Le Clech, B. Jefferson, and S. Judd. 2002. “Membrane Fouling in Membrane Bioreactors for Wastewater Treatment.” *J. Environ. Eng.*, 128 (11): 1018–1029. https://doi.org/10.1061/(ASCE)0733-9372(2002)128:11(1018).

Chen, J., H. Lin, L. Shen, Y. He, M. Zhang, and B.-Q. Liao. 2017. “Realization of quantifying interfacial interactions between a randomly rough membrane surface and a foulant particle.” *Bioresource Technology*, 226: 220–228. https://doi.org/10.1016/j.biortech.2016.12.025.

Cho, B. D., and A. G. Fane. 2002. “Fouling transients in nominally sub-critical flux operation of a membrane bioreactor.” *Journal of Membrane Science*, 209 (2): 391–403. https://doi.org/10.1016/S0376-7388(02)00321-6.

Choo, K.-H., and C.-H. Lee. 1998. “Hydrodynamic behavior of anaerobic biosolids during crossflow filtration in the membrane anaerobic bioreactor.” *Water Research*, 32 (11): 3387–3397. https://doi.org/10.1016/S0043-1354(98)00103-1.

Christensen, M. L., M. K. Jørgensen, G. Van De Staey, L. De Cock, and I. Smets. 2021. “Hydraulic resistance and osmotic pressure effects in fouling layers during MBR operations.” *Journal of Membrane Science*, 627: 119213. https://doi.org/10.1016/j.memsci.2021.119213.

Cui, Z. F., S. Chang, and A. G. Fane. 2003. “The use of gas bubbling to enhance membrane processes.” *Journal of Membrane Science*, 221 (1–2): 1–35. https://doi.org/10.1016/S0376-7388(03)00246-1.

Daigger, G. T., S. Sharvelle, M. Arabi, and N. G. Love. 2019. “Progress and Promise Transitioning to the One Water/Resource Recovery Integrated Urban Water Management Systems.” *J. Environ. Eng.*, 145 (10): 04019061. https://doi.org/10.1061/(ASCE)EE.1943-7870.0001552.

Davis, R. H. 1992. “Modeling of Fouling of Crossflow Microfiltration Membranes.” *Separation and Purification Methods*, 21 (2): 75–126. https://doi.org/10.1080/03602549208021420.

Davis, R. H., and J. D. Sherwood. 1990. “A similarity solution for steady-state crossflow microfiltration.” *Chemical Engineering Science*, 45 (11): 3203–3209. https://doi.org/10.1016/0009-2509(90)80212-W.

Delgado, S., R. Villarroel, and E. González. 2008. “Effect of the shear intensity on fouling in submerged membrane bioreactor for wastewater treatment.” *Journal of Membrane Science*, 311 (1–2): 173–181. https://doi.org/10.1016/j.memsci.2007.12.019.

Desmond, P., K. T. Huisman, H. Sanawar, N. M. Farhat, J. Traber, E. O. Fridjonsson, M. L. Johns, H.-C. Flemming, C. Picioreanu, and J. S. Vrouwenvelder. 2022. “Controlling the hydraulic resistance of membrane biofilms by engineering biofilm physical structure.” *Water Research*, 210: 118031. https://doi.org/10.1016/j.watres.2021.118031.

Díaz, O., E. González, and L. Vera. 2024. “Influence of Air Scouring and Residual Fouling on Cake Build-Up and Compression in Membrane Bioreactors.” *Ind. Eng. Chem. Res.*, 63 (31): 13740–13751. https://doi.org/10.1021/acs.iecr.4c00794.

Díaz, O., L. Vera, E. González, E. García, and J. Rodríguez-Sevilla. 2016. “Effect of sludge characteristics on membrane fouling during start-up of a tertiary submerged membrane bioreactor.” *Environ Sci Pollut Res*, 23 (9): 8951–8962. https://doi.org/10.1007/s11356-016-6138-y.

Diez, V., D. Ezquerra, J. L. Cabezas, A. García, and C. Ramos. 2014. “A modified method for evaluation of critical flux, fouling rate and in situ determination of resistance and compressibility in MBR under different fouling conditions.” *Journal of Membrane Science*, 453: 1–11. https://doi.org/10.1016/j.memsci.2013.10.055.

Ding, A., H. Liang, G. Li, N. Derlon, I. Szivak, E. Morgenroth, and W. Pronk. 2016. “Impact of aeration shear stress on permeate flux and fouling layer properties in a low pressure membrane bioreactor for the treatment of grey water.” *Journal of Membrane Science*, 510: 382–390. https://doi.org/10.1016/j.memsci.2016.03.025.

Drews, A. 2010. “Membrane fouling in membrane bioreactors—Characterisation, contradictions, cause and cures.” *Journal of Membrane Science*, 363 (1–2): 1–28. https://doi.org/10.1016/j.memsci.2010.06.046.

Du, X., X. Liu, Y. Wang, E. Radaei, B. Lian, G. Leslie, G. Li, and H. Liang. 2017a. “Particle deposition on flat sheet membranes under bubbly and slug flow aeration in coagulation-microfiltration process: Effects of particle characteristic and shear stress.” *Journal of Membrane Science*, 541: 668–676. https://doi.org/10.1016/j.memsci.2017.07.023.

Du, X., Y. Wang, G. Leslie, G. Li, and H. Liang. 2017b. “Shear stress in a pressure-driven membrane system and its impact on membrane fouling from a hydrodynamic condition perspective: a review: Shear stress in a pressure-driven membrane system.” *J. Chem. Technol. Biotechnol*, 92 (3): 463–478. https://doi.org/10.1002/jctb.5154.

Ehsani, M., H. Doan, and A. Lohi. 2021. “A comprehensive review of membrane fouling and cleaning methods with emphasis on ultrasound-assisted fouling control processes.” *Korean J. Chem. Eng.*, 38 (8): 1531–1555. https://doi.org/10.1007/s11814-021-0832-2.

Erkan, H. S., N. B. Turan, and G. O. Engin. 2020. “Fouling control in MBR in a sustainable perspective.” *Current Developments in Biotechnology and Bioengineering*, 21–57. Elsevier.

Field, R. W., and G. K. Pearce. 2011. “Critical, sustainable and threshold fluxes for membrane filtration with water industry applications.” *Advances in Colloid and Interface Science*, 164 (1–2): 38–44. https://doi.org/10.1016/j.cis.2010.12.008.

Field, R. W., D. Wu, J. A. Howell, and B. B. Gupta. 1995. “Critical flux concept for microfiltration fouling.” *Journal of Membrane Science*, 100 (3): 259–272. https://doi.org/10.1016/0376-7388(94)00265-Z.

FOOD & WATER WATCH. 2025. *A No Brainer: How AI’s Energy and Water Footprints Threaten Climate Progress*. FOOD & WATER WATCH.

Francy, D. S., E. A. Stelzer, R. N. Bushon, A. M. G. Brady, A. G. Williston, K. R. Riddell, M. A. Borchardt, S. K. Spencer, and T. M. Gellner. 2012. “Comparative effectiveness of membrane bioreactors, conventional secondary treatment, and chlorine and UV disinfection to remove microorganisms from municipal wastewaters.” *Water Research*, 46 (13): 4164–4178. https://doi.org/10.1016/j.watres.2012.04.044.

Guo, J., S. Xia, R. Wang, and J. Zhao. 2008. “Study on membrane fouling of submerged membrane bioreactor in treating bathing wastewater.” *Journal of Environmental Sciences*, 20 (10): 1158–1167. https://doi.org/10.1016/S1001-0742(08)62204-4.

Guo, W., H.-H. Ngo, and J. Li. 2012. “A mini-review on membrane fouling.” *Bioresource Technology*, 122: 27–34. https://doi.org/10.1016/j.biortech.2012.04.089.

Guo, X., P. Hong, and T.-M. Laleg-Kirati. 2020. “Nonlinear Model Predictive Control Design for BSM-MBR: Benchmark of Membrane Bioreactor.” *IFAC-PapersOnLine*, 53 (2): 16524–16530. https://doi.org/10.1016/j.ifacol.2020.12.764.

He, C., Z. Liu, J. Wu, X. Pan, Z. Fang, J. Li, and B. A. Bryan. 2021. “Future global urban water scarcity and potential solutions.” *Nat Commun*, 12 (1): 4667. https://doi.org/10.1038/s41467-021-25026-3.

He, Z., D. J. Miller, S. Kasemset, L. Wang, D. R. Paul, and B. D. Freeman. 2016. “Fouling propensity of a poly(vinylidene fluoride) microfiltration membrane to several model oil/water emulsions.” *Journal of Membrane Science*, 514: 659–670. https://doi.org/10.1016/j.memsci.2016.04.018.

Hermia, J. 1985. “Blocking Filtration. Application to Non-Newtonian Fluids.” *Mathematical Models and Design Methods in Solid-Liquid Separation*, A. Rushton, ed., 83–89. Dordrecht: Springer Netherlands.

Ho, C.-C., and A. L. Zydney. 2000. “A Combined Pore Blockage and Cake Filtration Model for Protein Fouling during Microfiltration.” *Journal of Colloid and Interface Science*, 232 (2): 389–399. https://doi.org/10.1006/jcis.2000.7231.

Hoek, E. M. V., and M. Elimelech. 2003. “Cake-Enhanced Concentration Polarization: A New Fouling Mechanism for Salt-Rejecting Membranes.” *Environ. Sci. Technol.*, 37 (24): 5581–5588. https://doi.org/10.1021/es0262636.

Holland, J. H. 2006. “Studying Complex Adaptive Systems.” *Jrl Syst Sci & Complex*, 19 (1): 1–8. https://doi.org/10.1007/s11424-006-0001-z.

Hu, X., H. Lin, G. Yu, L. Shen, J. Teng, M. Zhang, B. Li, L. Zhao, D. L. Zhao, and C. Chen. 2025. “Deciphering the nexus of soluble microbial products (SMPs) and membrane fouling: Roles, mechanisms, and control strategies.” *Chemical Engineering Journal*, 520: 165910. https://doi.org/10.1016/j.cej.2025.165910.

Hwang, B.-K., W.-N. Lee, K.-M. Yeon, P.-K. Park, C.-H. Lee, in-S. Chang, A. Drews, and M. Kraume. 2008. “Correlating TMP Increases with Microbial Characteristics in the Bio-Cake on the Membrane Surface in a Membrane Bioreactor.” *Environ. Sci. Technol.*, 42 (11): 3963–3968. https://doi.org/10.1021/es7029784.

Iorhemen, O., R. Hamza, and J. Tay. 2016. “Membrane Bioreactor (MBR) Technology for Wastewater Treatment and Reclamation: Membrane Fouling.” *Membranes*, 6 (2): 33. https://doi.org/10.3390/membranes6020033.

Jeison, D., and J. B. Van Lier. 2006. “Cake layer formation in anaerobic submerged membrane bioreactors (AnSMBR) for wastewater treatment.” *Journal of Membrane Science*, 284 (1–2): 227–236. https://doi.org/10.1016/j.memsci.2006.07.035.

Jørgensen, M. K., T. V. Bugge, M. L. Christensen, and K. Keiding. 2012. “Modeling approach to determine cake buildup and compression in a high-shear membrane bioreactor.” *Journal of Membrane Science*, 409–410: 335–345. https://doi.org/10.1016/j.memsci.2012.04.002.

Jørgensen, M. K., K. Keiding, and M. L. Christensen. 2014. “On the reversibility of cake buildup and compression in a membrane bioreactor.” *Journal of Membrane Science*, 455: 152–161. https://doi.org/10.1016/j.memsci.2013.12.052.

Judd, S. 2008. “The status of membrane bioreactor technology.” *Trends in Biotechnology*, 26 (2): 109–116. https://doi.org/10.1016/j.tibtech.2007.11.005.

Jun, C., K. Aghasadeghi, and G. T. Daigger. 2024. “Optimizing Air Scouring Energy for Sustainable Membrane Bioreactor Operation by Characterizing the Combination of Factors Leading to Threshold Limiting Conditions.” *Membranes*, 14 (3): 58. https://doi.org/10.3390/membranes14030058.

Kang, S., A. Subramani, E. Hoek, M. Deshusses, and M. Matsumoto. 2004. “Direct observation of biofouling in cross-flow microfiltration: mechanisms of deposition and release.” *Journal of Membrane Science*, 244 (1–2): 151–165. https://doi.org/10.1016/j.memsci.2004.07.011.

Ladewig, B., and M. N. Z. Al-Shaeli. 2017. *Fundamentals of Membrane Bioreactors*. Springer Transactions in Civil and Environmental Engineering. Singapore: Springer Singapore.

Le-Clech, P., V. Chen, and T. A. G. Fane. 2006. “Fouling in membrane bioreactors used in wastewater treatment.” *Journal of Membrane Science*, 284 (1–2): 17–53. https://doi.org/10.1016/j.memsci.2006.08.019.

Li, H. 2000. “An assessment of depolarisation models of crossflow microfiltration by direct observation through the membrane.” *Journal of Membrane Science*, 172 (1–2): 135–147. https://doi.org/10.1016/S0376-7388(00)00334-3.

Li, X., and X. Wang. 2006. “Modelling of membrane fouling in a submerged membrane bioreactor.” *Journal of Membrane Science*, 278 (1–2): 151–161. https://doi.org/10.1016/j.memsci.2005.10.051.

Liang, J., L. Yu, and J. Wu. 2020. “The dynamic change of specific cake resistance in membrane bioreactor due to periodical cake relaxation.” *Journal of Environmental Chemical Engineering*, 8 (4): 103837. https://doi.org/10.1016/j.jece.2020.103837.

Liu, R., X. Huang, Y. F. Sun, and Y. Qian. 2003. “Hydrodynamic effect on sludge accumulation over membrane surfaces in a submerged membrane bioreactor.” *Process Biochemistry*, 39 (2): 157–163. https://doi.org/10.1016/S0032-9592(03)00022-0.

Lykkegaard Christensen, M. 2006. *The effect of filter cake viscoelasticity on filtration: a study of activated sludge dewatering : Ph. D. dissertation*. Aalborg: Section of Chemistry, Aalborg University.

Mallah, N. B., A. A. Shah, A. M. Pirzada, I. Ali, M. I. Khan, A. S. Jatoi, J. L. Ullman, and R. B. Mahar. 2024. “Advanced Control Strategies of Membrane Fouling in Wastewater Treatment: A Review.” *Processes*, 12 (12): 2681. https://doi.org/10.3390/pr12122681.

Mannina, G., and G. Di Bella. 2012. “Comparing two start-up strategies for MBRs: Experimental study and mathematical modelling.” *Biochemical Engineering Journal*, 68: 91–103. https://doi.org/10.1016/j.bej.2012.07.011.

Mcdonogh, R. M., A. G. Fane, and C. J. D. Fell. 1989. “Charge effects in the cross-flow filtration of colloids and particulates.” *Journal of Membrane Science*, 43 (1): 69–85. https://doi.org/10.1016/S0376-7388(00)82354-6.

Meng, F., S.-R. Chae, A. Drews, M. Kraume, H.-S. Shin, and F. Yang. 2009. “Recent advances in membrane bioreactors (MBRs): Membrane fouling and membrane material.” *Water Research*, 43 (6): 1489–1512. https://doi.org/10.1016/j.watres.2008.12.044.

Meng, F., B. Shi, F. Yang, and H. Zhang. 2007. “New insights into membrane fouling in submerged membrane bioreactor based on rheology and hydrodynamics concepts.” *Journal of Membrane Science*, 302 (1–2): 87–94. https://doi.org/10.1016/j.memsci.2007.06.030.

Meng, F., H. Zhang, Y. Li, X. Zhang, and F. Yang. 2005. “Application of fractal permeation model to investigate membrane fouling in membrane bioreactor.” *Journal of Membrane Science*, 262 (1–2): 107–116. https://doi.org/10.1016/j.memsci.2005.04.013.

Meng, F., S. Zhang, Y. Oh, Z. Zhou, H.-S. Shin, and S.-R. Chae. 2017. “Fouling in membrane bioreactors: An updated review.” *Water Research*, 114: 151–180. https://doi.org/10.1016/j.watres.2017.02.006.

Miller, D. J., S. Kasemset, D. R. Paul, and B. D. Freeman. 2014. “Comparison of membrane fouling at constant flux and constant transmembrane pressure conditions.” *Journal of Membrane Science*, 454: 505–515. https://doi.org/10.1016/j.memsci.2013.12.027.

Monclús, H., M. Dalmau, S. Gabarrón, G. Ferrero, I. Rodríguez-Roda, and J. Comas. 2015. “Full-scale validation of an air scour control system for energy savings in membrane bioreactors.” *Water Research*, 79: 1–9. https://doi.org/10.1016/j.watres.2015.03.032.

N. Petford. 2009. “Which effective viscosity?” *Mineral. mag.*, 73 (2): 167–191. https://doi.org/10.1180/minmag.2009.073.2.167.

Ognier, S., C. Wisniewski, and A. Grasmick. 2004. “Membrane bioreactor fouling in sub-critical filtration conditions: a local critical flux concept.” *Journal of Membrane Science*, 229 (1–2): 171–177. https://doi.org/10.1016/j.memsci.2003.10.026.

Petseva, D. N., V. M. Starovb, and I. B. Ivanova. n.d. “Concentrated dispersions of charged colloidal particles: sedimentation, ultrafiltration and diffusiow.”

Poorasgari, E., T. Vistisen Bugge, M. Lykkegaard Christensen, and M. Koustrup Jørgensen. 2015. “Compressibility of fouling layers in membrane bioreactors.” *Journal of Membrane Science*, 475: 65–70. https://doi.org/10.1016/j.memsci.2014.09.056.

Pradhan, M., M. A. H. Johir, J. Kandasamy, H. Ratnaweera, and S. Vigneswaran. 2022. “Effects of Viscosity on Submerged Membrane Microfiltration Systems.” *Membranes*, 12 (8): 780. https://doi.org/10.3390/membranes12080780.

Pritchard, M., J. A. Howell, and R. W. Field. 1995. “The ultrafiltration of viscous fluids.” *Journal of Membrane Science*, 102: 223–235. https://doi.org/10.1016/0376-7388(94)00309-M.

Psoch, C., and S. Schiewer. 2005. “Critical flux aspect of air sparging and backflushing on membrane bioreactors.” *Desalination*, 175 (1): 61–71. https://doi.org/10.1016/j.desal.2004.09.023.

Qiao, Z., Y. Guo, and Z. Wang. 2022. “A multi-functional rinsing model based on cake properties for predicting rinsing efficiency and calculating energy consumption in MBR.” *Journal of Membrane Science*, 660: 120849. https://doi.org/10.1016/j.memsci.2022.120849.

Ratkovich, N., W. Horn, F. P. Helmus, S. Rosenberger, W. Naessens, I. Nopens, and T. R. Bentzen. 2013. “Activated sludge rheology: A critical review on data collection and modelling.” *Water Research*, 47 (2): 463–482. https://doi.org/10.1016/j.watres.2012.11.021.

Romero, C. A., and R. H. Davis. 1988. “Global model of crossflow microfiltration based on hydrodynamic particle diffusion.” *Journal of Membrane Science*, 39 (2): 157–185. https://doi.org/10.1016/S0376-7388(00)80987-4.

Romero, C. A., and R. H. Davis. 1990. “Transient model of crossflow microfiltration.” *Chemical Engineering Science*, 45 (1): 13–25. https://doi.org/10.1016/0009-2509(90)87076-5.

Romero, C. A., and R. H. Davis. 1991. “Experimental verification of the shear-induced hydrodynamic diffusion model of crossflow microfiltration.” *Journal of Membrane Science*, 62 (3): 249–273. https://doi.org/10.1016/0376-7388(91)80042-5.

Sandoval-García, V., M. V. Ruano, M. Alliet, C. Brepols, J. Comas, J. Harmand, M. Heran, G. Mannina, I. Rodriguez-Roda, I. Smets, and A. Robles. 2025. “Modeling MBR fouling: A critical review analysis towards establishing a framework for good modeling practices.” *Water Research*, 268: 122611. https://doi.org/10.1016/j.watres.2024.122611.

Schwarz, A. O., B. E. Rittmann, G. V. Crawford, A. M. Klein, and G. T. Daigger. 2006. “Critical Review on the Effects of Mixed Liquor Suspended Solids on Membrane Bioreactor Operation.” *Separation Science and Technology*, 41 (7): 1489–1511. https://doi.org/10.1080/01496390600634699.

Shen, L., Q. Lei, J.-R. Chen, H.-C. Hong, Y.-M. He, and H.-J. Lin. 2015. “Membrane fouling in a submerged membrane bioreactor: Impacts of floc size.” *Chemical Engineering Journal*, 269: 328–334. https://doi.org/10.1016/j.cej.2015.02.002.

Song, L., and M. Elimelech. 1995. “Particle Deposition onto a Permeable Surface in Laminar Flow.” *Journal of Colloid and Interface Science*, 173 (1): 165–180. https://doi.org/10.1006/jcis.1995.1310.

Stoller, M., and J. M. Ochando-Pulido. 2014. “About Merging Threshold and Critical Flux Concepts into a Single One: The Boundary Flux.” *The Scientific World Journal*, 2014: 1–8. https://doi.org/10.1155/2014/656101.

Tarleton, E. S. 1994. “UNDERSTANDING FLUX DECLINE IN CROSSFLOW MICROFILTRATION – PART II: EFFECTS OF PROCESS PARAMETERS.”

Trettin, D. R., and M. R. Doshi. 1980. “LIMITING FLUX IN ULTRAFILTRATION OF MACROMOLECULAR SOLUTIONS.” *Chemical Engineering Communications*, 4 (4–5): 507–522. https://doi.org/10.1080/00986448008935925.

Trussell, R. S., R. P. Merlo, S. W. Hermanowicz, and D. Jenkins. 2007. “Influence of mixed liquor properties and aeration intensity on membrane fouling in a submerged membrane bioreactor at high mixed liquor suspended solids concentrations.” *Water Research*, 41 (5): 947–958. https://doi.org/10.1016/j.watres.2006.11.012.

UN Water (Ed.). 2024. *Water for prosperity and peace*. The United Nations World Water Development Report. Paris: UNESCO.

Van Den Berg, G. B., I. G. Rácz, and C. A. Smolders. 1989. “Mass transfer coefficients in cross-flow ultrafiltration.” *Journal of Membrane Science*, 47 (1–2): 25–51. https://doi.org/10.1016/S0376-7388(00)80858-3.

Van Der Marel, P., A. Zwijnenburg, A. Kemperman, M. Wessling, H. Temmink, and W. Van Der Meer. 2009. “An improved flux-step method to determine the critical flux and the critical flux for irreversibility in a membrane bioreactor.” *Journal of Membrane Science*, 332 (1–2): 24–29. https://doi.org/10.1016/j.memsci.2009.01.046.

Vera, L., E. González, O. Díaz, R. Sánchez, R. Bohorque, and J. Rodríguez-Sevilla. 2015. “Fouling analysis of a tertiary submerged membrane bioreactor operated in dead-end mode at high-fluxes.” *Journal of Membrane Science*, 493: 8–18. https://doi.org/10.1016/j.memsci.2015.06.014.

Wang, B., Y. Zhang, G. Zhang, K. Zhang, and R. W. Field. 2021. “Innovation and optimization of aeration in free bubbling flat sheet MBRs.” *Journal of Membrane Science*, 635: 119522. https://doi.org/10.1016/j.memsci.2021.119522.

Wang, X.-M., and X.-Y. Li. 2012. “A unified model for quantification of concentration polarization (CP) of particles during cross-flow membrane filtration.” *Colloids and Surfaces A: Physicochemical and Engineering Aspects*, 407: 99–107. https://doi.org/10.1016/j.colsurfa.2012.05.014.

Wang, Z., and Z. Gao. 2021. “A new flux prediction model for laminar and turbulent flow regimes in constant pressure cross-flow microfiltration.” *Journal of Environmental Chemical Engineering*, 9 (5): 106156. https://doi.org/10.1016/j.jece.2021.106156.

Wang, Z., and Z. Wu. 2009. “A Review of Membrane Fouling in MBRs: Characteristics and Role of Sludge Cake Formed on Membrane Surfaces.” *Separation Science and Technology*, 44 (15): 3571–3596. https://doi.org/10.1080/01496390903182578.

Wintgens, T. 2003. “Modelling of a membrane bioreactor system for municipal wastewater treatment.” *Journal of Membrane Science*, 216 (1–2): 55–65. https://doi.org/10.1016/S0376-7388(03)00046-2.

Xu, H., K. Xiao, X. Wang, S. Liang, C. Wei, X. Wen, and X. Huang. 2020. “Outlining the Roles of Membrane-Foulant and Foulant-Foulant Interactions in Organic Fouling During Microfiltration and Ultrafiltration: A Mini-Review.” *Front. Chem.*, 8: 417. https://doi.org/10.3389/fchem.2020.00417.

Yamamoto, K., M. Hiasa, T. Mahmood, and T. Matsuo. 1988. “DIRECT SOLID-LIQUID SEPARATION USING HOLLOW FIBER MEMBRANE IN AN ACTIVATED SLUDGE AERATION TANK.” *Water Pollution Research and Control Brighton*, 43–54. Elsevier.

Yang, F., A. Bick, S. Shandalov, A. Brenner, and G. Oron. 2009. “Yield stress and rheological characteristics of activated sludge in an airlift membrane bioreactor.” *Journal of Membrane Science*, 334 (1–2): 83–90. https://doi.org/10.1016/j.memsci.2009.02.022.

Yeo, A., and A. G. Fane. 2005. “Performance of individual fibers in a submerged hollow fiber bundle.” *Water Science and Technology*, 51 (6–7): 165–172. https://doi.org/10.2166/wst.2005.0635.

Ying, W., F. Yang, A. Bick, G. Oron, and M. Herzberg. 2010. “Extracellular Polymeric Substances (EPS) in a Hybrid Growth Membrane Bioreactor (HG-MBR): Viscoelastic and Adherence Characteristics.” *Environ. Sci. Technol.*, 44 (22): 8636–8643. https://doi.org/10.1021/es102309y.

Zsirai, T., P. Buzatu, P. Aerts, and S. Judd. 2012. “Efficacy of relaxation, backflushing, chemical cleaning and clogging removal for an immersed hollow fibre membrane bioreactor.” *Water Research*, 46 (14): 4499–4507. https://doi.org/10.1016/j.watres.2012.05.004.